

1 SEARCH FOR PRODUCTION OF A HIGGS BOSON AND A SINGLE TOP
2 QUARK IN MULTILEPTON FINAL STATES IN pp COLLISIONS AT $\sqrt{s} = 13$
3 TeV.

4 by

5 Jose Andres Monroy Montañez

6 A DISSERTATION

7 Presented to the Faculty of

8 The Graduate College at the University of Nebraska

In Partial Fulfilment of Requirements

10 For the Degree of Doctor of Philosophy

11 Major: Physics and Astronomy

12 Under the Supervision of Kenneth Bloom and Aaron Dominguez

13 Lincoln, Nebraska

14 July, 2018

15 SEARCH FOR PRODUCTION OF A HIGGS BOSON AND A SINGLE TOP
16 QUARK IN MULTILEPTON FINAL STATES IN pp COLLISIONS AT $\sqrt{s} = 13$
17 TeV.

18 Jose Andres Monroy Montañez, Ph.D.

19 University of Nebraska, 2018

20 Adviser: Kenneth Bloom and Aaron Dominguez

²¹ Table of Contents

²² Table of Contents	iii
²³ List of Figures	vii
²⁴ List of Tables	x
²⁵ 1 INTRODUCTION	1
²⁶ 2 Theoretical approach	2
27 2.1 Introduction	2
28 2.2 Standard model of particle physics	3
29 2.2.1 Fermions	5
30 2.2.1.1 Leptons	6
31 2.2.1.2 Quarks	8
32 2.2.2 Fundamental interactions	13
33 2.2.3 Gauge bosons	18
34 2.3 Electroweak unification and the Higgs mechanism	20
35 2.3.1 Spontaneous symmetry breaking (SSB)	28
36 2.3.2 Higgs mechanism	32
37 2.3.3 Masses of the gauge bosons	35

38	2.3.4	Masses of the fermions	36
39	2.3.5	The Higgs field	37
40	2.3.6	Production of Higgs bosons at LHC	38
41	2.3.7	Higgs boson decay channels	42
42	2.4	Associated production of a Higgs boson and a single Top quark.	43
43	2.5	The CP-mixing in tH processes	47
44	2.6	Experimantal status of the anomalous Higg-fermion coupling.	52
45	3	The CMS experiment at the LHC	54
46	3.1	Introduction	54
47	3.2	The LHC	55
48	3.3	The CMS experiment	65
49	3.3.1	Coordinate system	67
50	3.3.2	Pixels detector	68
51	3.3.3	Silicon strip tracker	70
52	3.3.4	Electromagnetic calorimeter	72
53	3.3.5	Hadronic calorimeter	73
54	3.3.6	Superconducting solenoid magnet	75
55	3.3.7	Muon system	76
56	3.3.8	CMS trigger system	77
57	3.3.9	CMS computing	79
58	4	Event generation, simulation and reconstruction	83
59	4.1	Event generation	84
60	4.2	Monte Carlo Event Generators.	88
61	4.3	CMS detector simulation.	89
62	4.4	Event reconstruction.	91

63	4.4.1	Particle-Flow Algorithm.	92
64	4.4.2	Event reconstruction examples	104
65	5	Statistical methods	107
66	5.1	Multivariate analysis	107
67	5.1.1	Decision trees	110
68	5.1.2	Boosted decision trees (BDT)	112
69	5.2	MVA methods, NN, BDT, boosting, overtraining, variable ranking	115
70	5.3	statistical inference, likelihood parametrization	115
71	5.4	nuisance parameters	115
72	5.5	exclusion limits	115
73	5.6	asymptotic limits	115
74	6	Search for production of a Higgs boson and a single top quark in multilepton final states in pp collisions at $\sqrt{s} = 13$ TeV	116
76	6.1	Introduction	116
77	6.2	Data and MC Samples	118
78	6.2.1	Full 2016 dataset and MC samples	118
79	6.2.2	Triggers	121
80	6.2.2.1	Trigger efficiency scale factors	121
81	6.3	Object Identification and event selection	122
82	6.3.1	Jets and b tagging	122
83	6.3.2	Lepton selection	123
84	6.3.3	Lepton selection efficiency	124
85	6.4	Background predictions	125
86	6.5	Signal discrimination	126
87	6.5.1	Classifiers response	130

88	6.6 Additional discriminating variables	133
89	Bibliography	134
90	References	136

⁹¹ List of Figures

92	2.1	Standard model of particle physics.	4
93	2.2	Transformations between quarks	12
94	2.3	Fundamental interactions in nature.	13
95	2.4	SM interactions diagrams	14
96	2.5	Neutral current processes	21
97	2.6	Spontaneous symmetry breaking mechanism	29
98	2.7	SSB Potential form	30
99	2.8	Potential for complex scalar field	31
100	2.9	SSB mechanism for complex scalar field	32
101	2.10	Proton-Proton collision	39
102	2.11	Higgs boson production mechanism Feynman diagrams	40
103	2.12	Higgs boson production cross section and decay branching ratios	41
104	2.13	Associated Higgs boson production mechanism Feynman diagrams	43
105	2.14	Cross section for tHq process as a function of κ_t	46
106	2.15	Cross section for tHW process as a function of κ_{Htt}	47
107	2.16	NLO cross section for tX_0 and $t\bar{t}X_0$.	50
108	2.17	NLO cross section for tWX_0 , $t\bar{t}X_0$.	51

109	2.18 Two dimentional κ_t - κ_V plot of the coupling modifiers. ATLAS and CMS combination.	52
110		
111	3.1 CERN accelerator complex	55
112	3.2 LHC protons source. First acceleration stage.	56
113	3.3 The LINAC2 accelerating system at CERN.	57
114	3.4 LHC layout and RF cavities module.	58
115	3.5 LHC dipole magnet.	60
116	3.6 Integrated luminosity delivered by LHC and recorded by CMS during 2016	62
117	3.7 LHC interaction points	63
118	3.8 Multiple pp collision bunch crossing at CMS.	65
119	3.9 Layout of the CMS detector	66
120	3.10 CMS detector coordinate system	67
121	3.11 CMS pixel detector schematic view.	70
122	3.12 SST Schematic view.	71
123	3.13 CMS ECAL schematic view	72
124	3.14 CMS HCAL schematic view	74
125	3.15 CMS solenoid magnet	75
126	3.16 CMS Muon system schematic view	76
127	3.17 CMS Level-1 trigger architecture	78
128	3.18 WLCG structure	80
129	3.19 Data flow from CMS detector through hardware Tiers	82
130		
131	4.1 Event generation process.	84
132	4.2 Particle flow algorithm.	92
133	4.3 Jet reconstruction.	100
134	4.4 Jet energy corrections.	101

134	4.5	Secondary vertex in a b-hadron decay.	103
135	4.6	HIG-13-004 Event 1 reconstruction.	104
136	4.7	$e\mu$ event reconstruction.	105
137	4.8	Recorded event reconstruction.	106
138	5.1	Scatter plots-MVA event classification.	109
139	5.2	Scalar test statistical.	109
140	5.3	Decision tree.	110
141	5.4	Decision tree output example.	113
142	6.1	The two leading-order diagrams of tHq production.	117
143	6.2	Input variables to the BDT for signal discrimination normalized.	127
144	6.3	Input variables to the BDT for signal discrimination not normalized.	129
145	6.4	BDT inputs as seen by TMVA against $t\bar{t}$.	130
146	6.5	BDT inputs as seen by TMVA against $t\bar{t}V$.	131
147	6.6	Correlation matrices for the input variables in the TMVA.	132
148	6.7	MVA classifiers performance.	132
149	6.8	Additional discriminating variables distributions.	134

¹⁵⁰ List of Tables

151	2.1	Fermions of the SM.	5
152	2.2	Fermion masses.	6
153	2.3	Leptons properties.	9
154	2.4	Quarks properties.	9
155	2.5	Fermion weak isospin and weak hypercharge multiplets.	11
156	2.6	Fundamental interactions features.	15
157	2.7	SM gauge bosons.	20
158	2.8	Higgs boson properties.	38
159	2.9	Predicted branching ratios for a SM Higgs boson with $m_H = 125 \text{ GeV}/c^2$	42
160	2.10	Predicted SM cross sections for tH production at $\sqrt{s} = 13 \text{ TeV}$	44
161	2.11	Predicted enhancement of the tHq and tHW cross sections at LHC	48
162	6.1	Signal samples and their cross section and branching fraction.	118
163	6.2	κ_V and κ_t combinations.	119
164	6.3	List of background samples used in this analysis (CMSSW 80X).	120
165	6.4	Leading-order $t\bar{t}W$ and $t\bar{t}Z$ samples used in the signal BDT training.	120
166	6.5	Table of high-level triggers that we consider in the analysis.	121
167	6.6	Trigger efficiency scale factors and associated uncertainties.	122
168	6.7	Requirements on each of the three muon selections.	123

169	6.8 Criteria for each of the three electron selections.	124
170	6.9 MVA input discriminating variables	128
171	6.10 TMVA input variables ranking for BDTA_GRAD method	133
172	6.11 TMVA configuration used in the BDT training.	133
173	6.12 ROC-integral for all the testing cases.	135

¹⁷⁴ Chapter 1

¹⁷⁵ INTRODUCTION

¹⁷⁶ **Chapter 2**

¹⁷⁷ **Theoretical approach**

¹⁷⁸ **2.1 Introduction**

¹⁷⁹ The physical description of the universe is a challenge that physicists have faced by
¹⁸⁰ making theories that refine existing principles and proposing new ones in an attempt
¹⁸¹ to embrace emerging facts and phenomena.

¹⁸²

¹⁸³ At the end of 1940s Julian Schwinger [1] and Richard P. Feynman [2], based in the
¹⁸⁴ work of Sin-Itiro Tomonaga [3], developed an electromagnetic theory consistent with
¹⁸⁵ special relativity and quantum mechanics that describes how matter and light inter-
¹⁸⁶ act; the so-called “quantum eletrodynamics” (QED) had born.

¹⁸⁷

¹⁸⁸ QED has become the guide in the development of theories that describe the universe.
¹⁸⁹ It was the first example of a quantum field theory (QFT), which is the theoretical
¹⁹⁰ framework for building quantum mechanical models that describes particles and their
¹⁹¹ interactions. QFT is composed of a set of mathematical tools that combines classical
¹⁹² fields, special relativity and quantum mechanics, while keeping the quantum point

193 particles and locality ideas.

194 This chapter gives an overview of the standard model of particle physics, starting
 195 with a description of the particles and interactions that compose it, followed by a
 196 description of the electroweak interaction, the Higgs boson and the associated pro-
 197 duction of Higgs boson and a single top quark (tH). The description contained in
 198 this chapter is based on references [4–6].

199 **2.2 Standard model of particle physics**

200 Particle physics at the fundamental level is modeled in terms of a collection of in-
 201 teracting particles and fields in a theory known as the “standard model of particle
 202 physics (SM)”¹.

203

204 The full picture of the SM is composed of three fields², whose excitations are inter-
 205 preted as particles called mediators or force-carriers; a set of fields, whose excitations
 206 are interpreted as elementary particles, interacting through the exchange of those
 207 mediators and a field that gives the mass to elementary particles. Figure 2.1 shows
 208 an scheme of the SM particles organization. In addition to the particles in the scheme
 209 (but not listed in it), their corresponding anti-particles, with opposite quantum num-
 210 bers, are also part of the picture; some particles are their own anti-particles, like
 211 photon or Higgs, or anti-particle is already listed like in the W^+ and W^- case.

212

213 The mathematical formulation of the SM is based on group theory and the use of
 214 Noether’s theorem [8] which states that for a physical system modeled by a Lagrangian

¹ The formal and complete treatment of the SM is out of the scope of this document, however a plenty of textbooks describing it at several levels are available in the literature. The treatment in references [?] is quite comprehensive and detailed.

² Note that gravitational field is not included in the standard model formulation

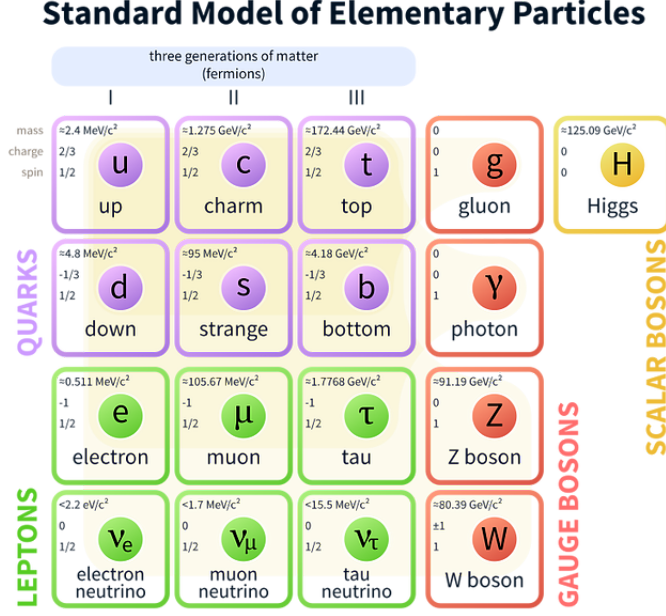


Figure 2.1: Schematic representation of the Standard model of particle physics. SM is a theoretical model intended to describe three of the four fundamental forces of the universe in terms of a set of particles and their interactions. [7].

that is invariant under a group of transformations a conservation law is expected. For instance, a system described by a time-independent Lagrangian is invariant (symmetric) under time changes (transformations) with the total energy conservation law as the expected conservation law. In QED, the charge operator (Q) is the generator of the $U(1)$ symmetry which according to the Noether's theorem means that there is a conserved quantity; this conserved quantity is the electric charge and thus the law of conservation of electric charge is established.

222

In the SM, the symmetry group $SU(3)_C \otimes SU(2)_L \otimes U(1)_Y$ describes three of the four fundamental interactions in nature(see section 2.2.2): strong interaction(SI), weak interaction(WI) and electromagnetic interactions (EI) in terms of symmetries associated to physical quantities:

- 227 • Strong: $SU(3)_C$ associated to color charge
- 228 • Weak: $SU(2)_L$ associated to weak isospin and chirality
- 229 • Electromagnetic: $U(1)_Y$ associated to weak hypercharge and electric charge
- 230 It will be shown that the electromagnetic and weak interactions are combined in
 231 the so-called electroweak interaction where chirality, hypercharge, weak isospin and
 232 electric charge are the central concepts.

233 **2.2.1 Fermions**

234 The basic constituents of the ordinary matter at the lowest level, which form the set
 235 of elementary particles in the SM formulation, are quarks and leptons. All of them
 236 have spin 1/2, therefore they are classified as fermions since they obey Fermi-Dirac
 237 statistics. There are six “flavors” of quarks and three of leptons organized in three
 238 generations, or families, as shown in table 2.1.

239

		Generation		
		1st	2nd	3rd
Leptons	Charged	Electron (e)	Moun(μ)	Tau (τ)
	Neutral	Electron neutrino (ν_e)	Muon neutrino (ν_μ)	Tau neutrino (ν_τ)
Quarks	Up-type	Up (u)	Charm (c)	Top (t)
	Down-type	Down (d)	Strange (s)	Bottom (b)

Table 2.1: Fermions of the SM. There are six flavors of quarks and three of leptons, organized in three generations, or families, composed of two pairs of closely related particles. The close relationship is motivated by the fact that WI between leptons is limited to the members of the same generation; WI between quarks is not limited but greatly favoured, to same generation members.

240

241 There is a mass hierarchy between generations (see table 2.2), where the higher gener-
 242 ation particles decays to the lower one, which can explain why the ordinary matter is

made of particles in the first generation. In the SM, neutrinos are modeled as massless particles so they are not subject to this mass hierarchy; however, today it is known that neutrinos are massive so the hierarchy could be restated. The reason behind this mass hierarchy is one of the most important open questions in particle physics, and it becomes more puzzling when noticing that the mass difference between first and second generation fermions is small compared to the mass difference with respect to the third generation.

Lepton	Mass (MeV/c ²)	Quark	Mass (MeV/c ²)
e	0.51	u	2.2
μ	105.65	c	1.28×10^3
τ	1776.86	t	173.1×10^3
ν_e	Unknown	d	4.7
ν_μ	Unknown	s	96
τ_μ	Unknown	b	4.18×10^3

Table 2.2: Fermion masses [9]. Generations differ by mass in a way that have been interpreted as a masss hierarchy. Approximate values with no uncertainties are used, for comparison purpose.

Usually, the second and third generation fermions are produced in high energy processes, like the ones recreated in particle accelerators.

2.2.1.1 Leptons

A lepton is an elementary particle that is not subject to the SI. As seen in table 2.1, there are two types of leptons, the charged ones (electron, muon and tau) and the neutral ones (the three neutrinos). The electric charge (Q) is the property that gives leptons the ability to participate in the EI. From the classical point of view, Q plays a central role determining, among others, the strength of the electric field through which the electromagnetic force is exerted. It is clear that neutrinos are not affected

260 by EI because they don't carry electric charge.

261

262 Another feature of the leptons that is fundamental in the mathematical description
263 of the SM is the chirality, which is closely related to spin and helicity. Helicity defines
264 the handedness of a particle by relating its spin and momentum such that if they
265 are parallel then the particle is right-handed; if spin and momentum are antiparallel
266 the particle is said to be left-handed. The study of parity conservation (or viola-
267 tion) in β -decay has shown that only left-handed electrons/neutrinos or right-handed
268 positrons/anti-neutrinos are created [10]; the inclusion of that feature in the theory
269 was achieved by using projection operators for helicity, however, helicity is frame de-
270 pendent for massive particles which makes it not Lorentz invariant and then another
271 related attribute has to be used: *chirality*.

272

273 Chirality is a purely quantum attribute which makes it not so easy to describe in
274 graphical terms but it defines how the wave function of a particle transforms under
275 certain rotations. As with helicity, there are two chiral states, left-handed chiral (L)
276 and right-handed chiral (R). In the highly relativistic limit where $E \approx p \gg m$ helicity
277 and chirality converge, becoming exactly the same for massless particles.

278

279 In the following, when referring to left-handed (right-handed) it will mean left-handed
280 chiral (right-handed chiral). The fundamental fact about chirality is that while EI
281 and SI are not sensitive to chirality, in WI left-handed and right-handed fermions are
282 treated asymmetrically, such that only left handed fermions and right-handed anti-
283 fermions are allowed to couple to WI mediators, which is a violation of parity. The
284 way to translate this statement in a formal mathematical formulation is based on the
285 isospin symmetry group $SU(2)_L$.

286

287 Each generation of leptons is seen as a weak isospin doublet.³ The left-handed charged
 288 lepton and its associated left-handed neutrino are arranged in doublets of weak isospin
 289 T=1/2 while their right-handed partners are singlets:

$$\begin{pmatrix} \nu_l \\ l \end{pmatrix}_L, l_R := \begin{pmatrix} \nu_e \\ e \end{pmatrix}_L, \begin{pmatrix} \nu_\mu \\ \mu \end{pmatrix}_L, \begin{pmatrix} \nu_\tau \\ \tau \end{pmatrix}_L, e_R, \mu_R, \tau_R, \nu_{eR}, \nu_{\mu R}, \nu_{\tau R} \quad (2.1)$$

290 The isospin third component refers to the eigenvalues of the weak isospin operator
 291 which for doublets is $T_3 = \pm 1/2$, while for singlets it is $T_3 = 0$. The physical meaning
 292 of this doublet-singlet arrangement falls in that the WI couples the two particles in
 293 the doublet by exchanging the interaction mediator while the singlet member is not
 294 involved in WI. The main properties of the leptons are summarized in table 2.3.

295

296 Altough all three flavor neutrinos have been observed, their masses remain unknown
 297 and only some estimations have been made [11]. The main reason is that the fla-
 298 vor eigenstates are not the same as the mass eigenstates which implies that when
 299 a neutrino is created its mass state is a linear combination of the three mass eigen-
 300 states and experiments can only probe the squared difference of the masses. The
 301 Pontecorvo-Maki-Nakagawa-Sakata (PMNS) mixing matrix encode the relationship
 302 between flavor and mass eigenstates.

303

304 2.2.1.2 Quarks

305 Quarks are the basic constituents of protons and neutrons. The way quarks join to
 306 form bound states, called “hadrons”, is through the SI. Quarks are affected by all the

³ The weak isospin is an analogy of the isospin symmetry in strong interaction where neutron and proton are affected equally by strong force but differ in their charge.

Lepton	Q(e)	T_3	L_e	L_μ	L_τ	Lifetime (s)
Electron (e)	-1	-1/2	1	0	0	Stable
Electron neutrino(ν_e)	0	1/2	1	0	0	Unknown
Muon (μ)	-1	-1/2	0	1	0	2.19×10^{-6}
Muon neutrino (ν_μ)	0	1/2	0	1	0	Unknown
Tau (τ)	-1	-1/2	0	0	1	290.3×10^{-15}
Tau neutrino (τ_μ)	0	1/2	0	0	1	Unknown

Table 2.3: Leptons properties [9]. Q: electric charge, T_3 : weak isospin. Only left-handed leptons and right-handed anti-leptons participate in the WI. Anti-particles with inverted T_3 , Q and lepton number complete the leptons set but are not listed. Right-handed leptons and left-handed anti-leptons, neither listed, form weak isospin singlets with $T_3 = 0$ and do not take part in the weak interaction.

307 fundamental interactions which means that they carry all the four types of charges:
 308 color, electric charge, weak isospin and mass.

Flavor	Q(e)	I_3	T_3	B	C	S	T	B'	Y	Color
Up (u)	2/3	1/2	1/2	1/3	0	0	0	0	1/3	r,b,g
Charm (c)	2/3	0	1/2	1/3	1	0	0	0	4/3	r,b,g
Top(t)	2/3	0	1/2	1/3	0	0	1	0	4/3	r,b,g
Down(d)	-1/3	-1/2	-1/2	1/3	0	0	0	0	1/3	r,b,g
Strange(s)	-1/3	0	-1/2	1/3	0	-1	0	0	-2/3	r,b,g
Bottom(b)	-1/3	0	-1/2	1/3	0	0	0	-1	-2/3	r,b,g

Table 2.4: Quarks properties [9]. Q: electric charge, I_3 : isospin, T_3 : weak isospin, B: baryon number, C: charmness, S: strangeness, T: topness, B' : bottomness, Y: hypercharge. Anti-quarks posses the same mass and spin as quarks but all charges (color, flavor numbers) have opposite sign.

309
 310 Table 2.4 summarizes the features of quarks, among which the most particular is
 311 their fractional electric charge. Note that fractional charge is not a problem, given
 312 that quarks are not found isolated, but serves to explain how composed particles are
 313 formed out of two or more valence quarks⁴.

314

⁴ Hadrons can contain an indefinite number of virtual quarks and gluons, known as the quark and gluon sea, but only the valence quarks determine hadrons' quantum numbers.

315 Color charge is the responsible for the SI between quarks and is the symmetry
 316 ($SU(3)_C$) that defines the formalism to describe SI. There are three colors: red (r),
 317 blue(b) and green(g) and their corresponding three anti-colors; thus each quark carries
 318 one color unit while anti-quarks carries one anti-color unit. As said above, quarks are
 319 not allowed to be isolated due to the color confinement effect, therefore their features
 320 have been studied indirectly by observing their bound states created when:

- 321 • one quark with a color charge is attracted by an anti-quark with the correspond-
 322 ing anti-color charge forming a colorless particle called a “meson.”
- 323 • three quarks (anti-quarks) with different color (anti-color) charges are attracted
 324 among them forming a colorless particle called a “baryon(anti-baryon).”

325 In practice, when a quark is left alone isolated a process called “hadronization” occurs
 326 where the quark emits gluons (see section 2.2.3) which eventually will generate new
 327 quark-antiquark pairs and so on; those quarks will recombine to form hadrons that
 328 will decay into leptons. This proliferation of particles looks like a “jet” coming from
 329 the isolated quark. More details about the hadronization process and jet structure
 330 will be given in chapter4.

331 In the first version of the quark model (1964), M. Gell-Mann [12] and G. Zweig
 332 [13, 14] developed a consistent way to classify hadrons according to their properties.
 333 Only three quarks (u, d, s) were involved in a scheme in which all baryons have
 334 baryon number $B=1$ and therefore quarks have $B=1/3$; non-baryons have $B=0$. The
 335 scheme organizes baryons in a two-dimensional space ($I_3 - Y$); Y (hypercharge) and I_3
 336 (isospin) are quantum numbers related by the Gell-Mann-Nishijima formula [15, 16]:

$$Q = I_3 + \frac{Y}{2} \quad (2.2)$$

337 where $Y = B + S + C + T + B'$ are the quantum numbers listed in table 2.4. Baryon
 338 number is conserved in SI and EI which means that single quarks cannot be created
 339 but in pairs $q - \bar{q}$.

340

341 There are six quark flavors organized in three generations (see table 2.1) following a
 342 mass hierarchy which, again, implies that higher generations decay to first generation
 343 quarks.

	Quarks			T_3	Y_W	Leptons			T_3	Y_W
Doublets	$(\begin{smallmatrix} u \\ d' \end{smallmatrix})_L$	$(\begin{smallmatrix} c \\ s' \end{smallmatrix})_L$	$(\begin{smallmatrix} t \\ b' \end{smallmatrix})_L$	$(\begin{smallmatrix} 1/2 \\ -1/2 \end{smallmatrix})$	1/3	$(\begin{smallmatrix} \nu_e \\ e \end{smallmatrix})_L$	$(\begin{smallmatrix} \nu_\mu \\ \mu \end{smallmatrix})_L$	$(\begin{smallmatrix} \nu_\tau \\ \tau \end{smallmatrix})_L$	$(\begin{smallmatrix} 1/2 \\ -1/2 \end{smallmatrix})$	-1
Singlets	u_R	c_R	t_R	0	4/3	ν_{eR}	$\nu_{\mu R}$	$\nu_{\tau R}$	0	-2

Table 2.5: Fermion weak isospin and weak hypercharge multiplets. Weak hypercharge is calculated through the Gell-Mann-Nishijima formula 2.2 but using the weak isospin and charge for quarks.

344

345 Isospin doublets of quarks are also defined (see table 2.5) and as for neutrinos, the
 346 mass eigenstates are not the same as the WI eigenstates which means that members of
 347 different quark generations are connected by the WI mediator; thus, up-type quarks
 348 are coupled not to down-type quarks directly but to a superposition of down-type
 349 quarks (q'_d) via WI according to:

$$q'_d = V_{CKM} q_d$$

350

$$\begin{pmatrix} d' \\ s' \\ b' \end{pmatrix} = \begin{pmatrix} V_{ud} & V_{us} & V_{ub} \\ V_{cd} & V_{cs} & V_{cb} \\ V_{td} & V_{ts} & V_{tb} \end{pmatrix} \begin{pmatrix} d \\ s \\ b \end{pmatrix} \quad (2.3)$$

351 where V_{CKM} is known as Cabibbo-Kobayashi-Maskawa (CKM) mixing matrix [17,18].

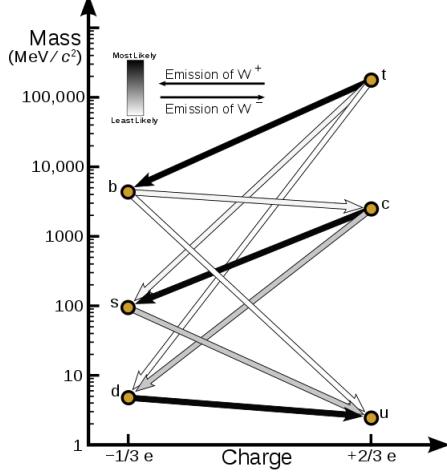


Figure 2.2: Transformations between quarks through the exchange of a WI. Higher generations quarks decay to first generation quarks by emitting a W boson. The arrow color indicates the likelihood of the transition according to the grey scale in the top left side which represent the CKM matrix parameters [19].

352 The weak decays of quarks are represented in the diagram of figure 2.2; again the
 353 CKM matrix plays a central role since it contains the probabilities for the different
 354 quark decay channels, in particular, note that quark decays are greatly favored be-
 355 tween generation members.

356

357 CKM matrix is a 3×3 unitary matrix parametrized by three mixing angles and
 358 the *CP-mixing phase*; the latter is the parameter responsible for the Charge-Parity
 359 symmetry violation (CP-violation) in the SM. The fact that the b quark decays almost
 360 all the times to a top quark is exploited in this thesis when making the selection of
 361 the signal events by requiring the presence of a jet tagged as a jet coming from a
 362 b quark in the final state. The effect of the *CP-mixing phase* on the cross section of
 363 associated production of Higgs boson and a single top process is also explored in this
 364 thesis.

365 2.2.2 Fundamental interactions

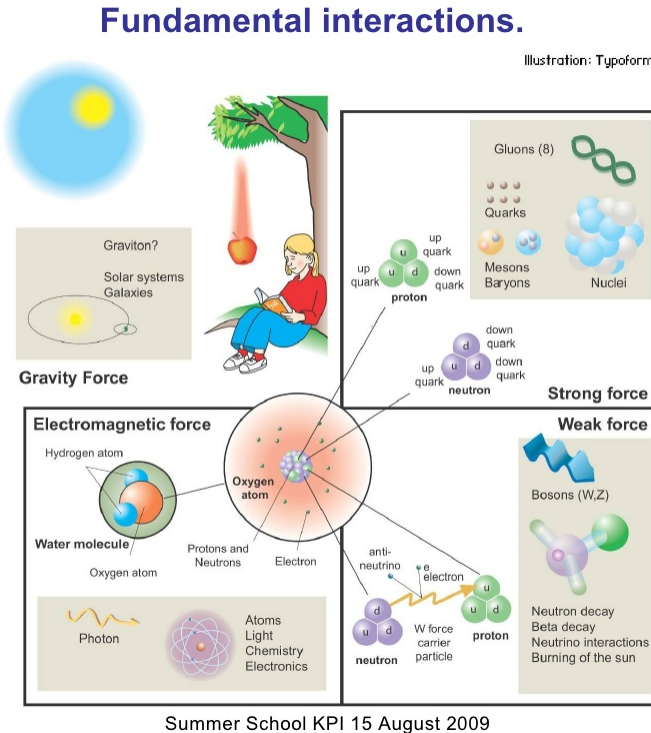


Figure 2.3: Fundamental interactions in nature. Despite the many manifestations of forces in nature, we can track all of them back to one of the fundamental interactions. The most common forces are gravity and electromagnetic given that all of us are subject and experience them in everyday life.

366 Even though there are many manifestations of force in nature, like the ones repre-

367 sented in figure 2.3, we can classify all of them into one of four fundamental interac-

368 tions:

- 369 • *Electromagnetic interaction (EI)* affects particles that are “electrically charged,”
 370 like electrons and protons. It is described by QED combining quantum mechan-
 371 ics, special relativity and electromagnetism in order to explain how particles
 372 with electric charge interact through the exchange of photons, therefore, one
 373 says that “Electromagnetic Force” is mediated by “photons”. Figure 2.4a. shows

374 a graphical representation, known as “feynman diagram”, of electron-electron
 375 scattering.

- 376 • *Strong interaction (SI)* described by Quantum Chromodynamics (QCD). Hadrons
 377 like proton and neutron have internal structure given that they are composed
 378 of two or more valence quarks⁵. Quarks have fractional electric charge which
 379 means that they are subject to electromagnetic interaction and in the case of the
 380 proton they should break apart due to electrostatic repulsion; however, quarks
 381 are held together inside the hadrons against their electrostatic repulsion by the
 382 “Strong Force” through the exchange of “gluons.” The analog to the electric
 383 charge is the “color charge”. Electrons and photons are elementary particles
 384 as quarks but they don’t carry color charge, therefore they are not subject to
 385 SI. The feynman diagram for gluon exchange between quarks is shown in figure
 386 2.4b.

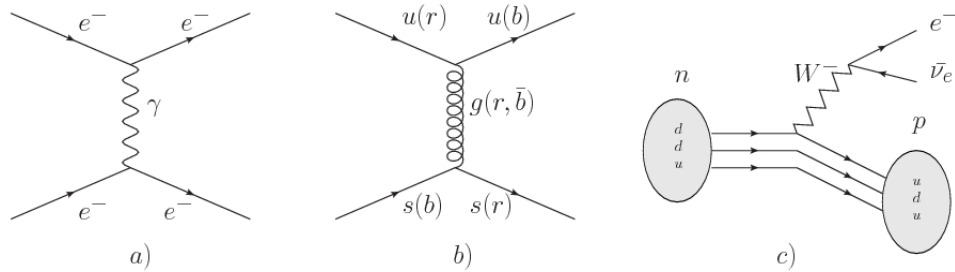


Figure 2.4: Feynman diagrams representing the interactions in SM; a) EI: e-e scattering; b) SI: gluon exchange between quarks ; c) WI: β -decay

- 387 • *Weak interaction (WI)* described by the weak theory (WT), is responsible, for
 388 instance, for the radioactive decay in atoms and proton-proton (pp) fusion
 389 within the sun. Quarks and leptons are the particles affected by the weak
 390 interaction; they possess a property called “flavor charge” (see 2.2.1) which can
 391 be changed by emitting or absorbing one weak force mediator. There are three

⁵ particles made of four and five quarks are exotic states not so common.

392 mediators of the “weak force” known as “Z” boson in the case of electrically
 393 neutral changes and “ W^\pm ” bosons in the case of electrically charged changes.
 394 The “weak isospin” is the WI analog to electric charge in EI, and color charge
 395 in SI, and defines how quarks and leptons are affected by the weak force. Figure
 396 2.4c. shows the feynman diagram of β -decay where a newtron (n) is transformed
 397 in a proton (p) by emmiting a W^- particle. Since this thesis is in the frame
 398 of the electroweak interaction, a more detailed description of it will be given in
 399 section 2.3

400 • *Gravitational interaction (GI)* described by General Theory of Relativity (GR).
 401 It is responsible for the structure of galaxies and black holes as well as the
 402 expansion of the universe. As a classical theory, in the sense that it can be for-
 403 mulated without even appeal to the concept of quantization, it implies that the
 404 spacetime is a continuum and predictions can be made without limitation to the
 405 precision of the measurement tools. The latter represent a direct contradiction
 406 of the quantum mechanics principles. Gravity is deterministic while quantum
 407 mechanics is probabilistic; despite that, efforts to develop a quantum theory of
 408 gravity have predicted the “graviton” as mediator of the Gravitational force⁶.

Interaction	Acts on	Relative strength	Range (m)	Mediators
Electromagnetic (QED)	Electrically charged particles	10^{-2}	Infinite	Photon
Strong (QCD)	Quarks and gluons	1	10^{-15}	Gluon
Weak (WI)	Leptons and quarks	10^{-6}	10^{-18}	W^\pm , Z
Gravitational (GI)	Massive particles	10^{-39}	Infinite	Graviton

Table 2.6: Fundamental interactions features [20].

409

⁶ Actually a wide variety of theories have been developed in an attempt to describe gravity; some famous examples are string theory and supergravity.

410 Table 2.6 summarizes the main features of the fundamental interactions. The rela-
 411 tive strength of the fundamental forces reveals the meaning of strong and weak; in
 412 a context where the relative strength of the SI is 1, the EI is about hundred times
 413 weaker and WI is about million times weaker than the SI. A good description on
 414 how the relative strength and range of the fundamental interactions are calculated
 415 can be found in references [20, 21]. In the everyday life, only EI and GI are explicitly
 416 experienced due to the range of these interactions; i.e., at the human scale distances
 417 only EI and GI have appreciable effects, in contrast to SI which at distances greater
 418 than 10^{-15} m become negligible.

419

420 QED was built successfully on the basis of the classical electrodynamics theory (CED)
 421 of Maxwell and Lorentz, following theoretical and experimental requirements imposed
 422 by

- 423 • lorentz invariance: independence on the reference frame.
- 424 • locality: interacting fields are evaluated at the same space-time point to avoid
 425 action at a distance.
- 426 • renormalizability: physical predictions are finite and well defined
- 427 • particle spectrum, symmetries and conservation laws already known must emerge
 428 from the theory.
- 429 • gauge invariance.

430 The gauge invariance requirement reflects the fact that the fundamental fields cannot
 431 be directly measured but associated fields which are the observables. Electric (“E”)
 432 and magnetic (“B”) fields in CED are associated with the electric scalar potential

433 “V” and the vector potential “A”. In particular, \mathbf{E} can be obtained by measuring
 434 the change in the space of the scalar potential (ΔV); however, two scalar potentials
 435 differing by a constant “f” correspond to the same electric field. The same happens in
 436 the case of the vector potential “A”; thus, different configurations of the associated
 437 fields result in the same set of values of the observables. The freedom in choosing
 438 one particular configuration is known as “gauge freedom”; the transformation law con-
 439 necting two configurations is known as “gauge transformation” and the fact that the
 440 observables are not affected by a gauge transformation is called “gauge invariance”.

441

442 When the gauge transformation:

$$\begin{aligned} \mathbf{A} &\rightarrow \mathbf{A} - \Delta f \\ V &\rightarrow V - \frac{\partial f}{\partial t} \end{aligned} \tag{2.4}$$

443 is applied to Maxwell equations, they are still satisfied and the fields remain invariant.
 444 Thus, CED is invariant under gauge transformations and is called a “gauge theory”.
 445 The set of all gauge transformations form the “symmetry group” of the theory, which
 446 according to the group theory, has a set of “group generators”. The number of group
 447 generators determine the number of “gauge fields” of the theory.

448

449 As mentioned in the first lines of section 2.2, QED has one symmetry group ($U(1)$)
 450 with one group generator (the Q operator) and one gauge field (the electromagnetic
 451 field A^μ). In CED there is not a clear definition, beyond the historical convention, of
 452 which fields are the fundamental and which are the associated, but in QED it is clear
 453 that the fundamental field is A^μ . When a gauge theory is quantized, the gauge field

454 is quantized and its quanta is called “gauge boson”. The word boson characterizes
 455 particles with integer spin which obvey Bose-einstein statistics.

456

457 As will be detailed in section 2.3, interactions between partcles in a system can be
 458 obtained by considering first the Lagrangian density of free particles in the system,
 459 which of course is incomplete because the interaction terms have been left out, and
 460 demanding global phase transformation invariance. Global phase transformation in-
 461 variance means that a gauge transformation is performed identically to every point
 462 in the space⁷ and the Lagrangian remains invariant. Then, the global transformation
 463 is promoted to a local phase transformation (this time the gauge transformation de-
 464 pends on the position in space) and again invariance is required.

465

466 Due to the space dependence of the local tranformation, the Lagrangian density is
 467 not invariant anymore. In order to restate the gauge invariance, the gauge covariant
 468 derivative is introduced in the Lagrangian and with it the gauge field responsible for
 469 the interaction between particles in the system. The new Lagrangian density is gauge
 470 invariant, includes the interaction terms needed to account for the interactions and
 471 provides a way to explain the interaction between particles through the exchange of
 472 the gauge boson.

473 This recipe was used to build QED and the theories that aim to explain the funda-
 474 mental interactions.

475 **2.2.3 Gauge bosons**

476 The importance of the gauge bosons comes from the fact that they are the force
 477 mediators or force carriers. The features of the gauge bosons reflect those of the

⁷ Here space corresponds to the 4-dimensional space i.e. space-time.

478 fields they represent and they are extracted from the Lagrangian density used to
 479 describe the interactions. In section 2.3, it will be shown how the gauge bosons of the
 480 EI and WI emerge from the electroweak Lagrangian. The SI gauge bosons features
 481 are also extracted from the SI Lagrangian but it is not detailed in this document. The
 482 main features of the SM gauge bosons will be briefly presented below and summarized
 483 in table 2.7.

- 484 • **Photon.** EI occurs when the photon couples to (is exchanged between) particles
 485 carrying electric charge; however, the photon itself does not carry electric charge,
 486 therefore, there is no coupling between photons. Given that the photon is
 487 massless the EI is of infinite range, i.e., electrically charged particles interact
 488 even if they are located far away one from each other; this also implies that
 489 photons always move with the speed of light.
- 490 • **Gluon.** SI is mediated by gluons which, same as photons, are massless. They
 491 carry one unit of color charge and one unit of anticolor charge which means that
 492 gluons couple to other gluons. As a result, the range of the SI is not infinite
 493 but very short due to the attraction between gluons, giving rise to the “color
 494 confinement” which explains why color charged particles cannot be isolated but
 495 live within composited particles, like quarks inside protons.
- 496 • **W, Z.** The WI mediators, W^\pm and Z, are massive which explains their short-
 497 range. Given that the WI is the only interaction that can change the flavor
 498 of the interacting particles, the W boson is the responsible for the nuclear
 499 transmutation where a neutron is converted in a proton or vice versa with the
 500 involvement of an electron and a neutrino (see figure 2.4c). The Z boson is the
 501 responsible of the neutral weak processes like neutrino elastic scattering where

502 no electric charge but momentum transference is involved. WI gauge bosons
 503 carry isospin charge which makes possible the interaction between them.

Interaction	Mediator	Electric charge (e)	Color charge	Weak Isospin	mass (GeV/c ²)
Electromagnetic	Photon (γ)	0	No	0	0
Strong	Gluon (g)	0	Yes -octet	No	0
Weak	W^\pm Z	± 1 0	No No	± 1 0	80.385 ± 0.015 91.188 ± 0.002

Table 2.7: SM gauge bosons main features [9].

504

505 **2.3 Electroweak unification and the Higgs
 506 mechanism**

507 Physicists dream of building a theory that contains all the interactions in one single
 508 interaction, i.e., showing that at some scale in energy all the four fundamental in-
 509 teractions are unified and only one interaction emerges in a “Theory of everything”.
 510 The first sign of the feasibility of such unification comes from success in the con-
 511 struction of the CED. Einstein spent years trying to reach that dream, which by
 512 1920 only involved electromagnetism and gravity, with no success; however, a new
 513 partial unification was achieved in the 1960’s, when S.Glashow [22], A.Salam [23] and
 514 S.Weinberg [24] independently proposed that electromagnetic and weak interactions
 515 are two manifestations of a more general interaction called “electroweak interaction
 516 (EWT)”. Both, QCD and EWT, were developed in parallel and following the useful
 517 prescription provided by QED and the gauge invariance principles.

518

519 The theory of weak interactions was capable of explaining the β -decay and in general
 520 the processes mediated by W^\pm bosons. However, there were some processes like the

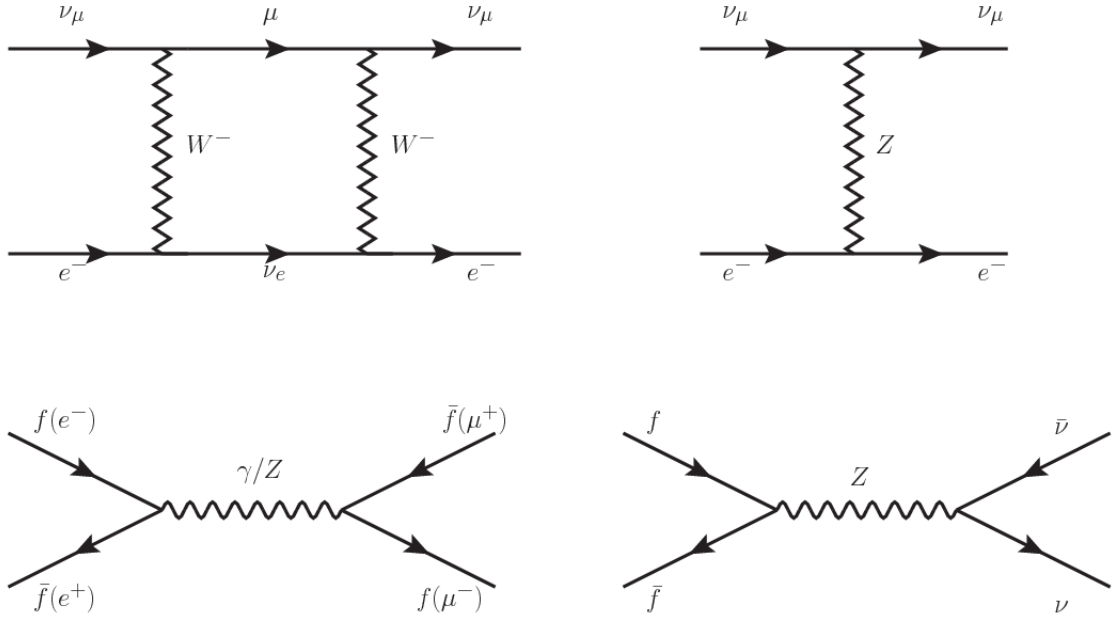


Figure 2.5: Top: $\nu_\mu - e^-$ scattering going through charged currents (left) and neutral currents (right). Bottom: neutral current processes for charged fermions (left) and involving neutrinos (right). While neutral current processes involving only charged fermions can proceed through EI or WI, those involving neutrinos can only proceed via WI.

521 “ $\nu_\mu - e$ scattering” which would require the exchange of two W bosons (see figure 2.5
 522 top diagrams) giving rise to divergent loop integrals and then non finite predictions.
 523 By including neutral currents involving fermions via the exchange of neutral bosons
 524 Z, those divergences are compensated and the predictions become realistic.

525

526 Neutral weak interaction vertices conserve flavor in the same way as the electromag-
 527 netic vertices do, but additionally, the Z boson can couple to neutrinos which implies
 528 that processes involving charged fermions can proceed through EI or WI but processes
 529 involving neutrinos can proceed only through WI.

530

531 The prescription to build a gauge theory of the WI consists of proposing a free field
 532 Lagrangian density that includes the particles involved; next, by requesting invari-

533 ance under global phase transformations first and generalizing to local phase trans-
 534 formations invariance later, the conserved currents are identified and interactions are
 535 generated by introducing gauge fields. Given that the goal is to include the EI and
 536 WI in a single theory, the group symmetry considered should be a combination of
 537 $SU(2)_L$ and $U(1)_{em}$, however the latter cannot be used directly because the EI treats
 538 left and right-handed particles indistinctly in contrast to the former. Fortunately, the
 539 weak hypercharge, which is a combination of the weak isospin and the electric charge
 540 (eqn 2.2) is suitable to be used since it is conserved by the EI and WI. Thus, the
 541 symmetry group to be considered is

$$G \equiv SU(2)_L \otimes U(1)_Y \quad (2.5)$$

542 The following treatment applies to any of the fermion generations, but for simplicity
 543 the first generation of leptons will be considered [5, 6, 25, 26].

544

545 Given the first generation of leptons

$$\psi_1 = \begin{pmatrix} \nu_e \\ e^- \end{pmatrix}_L, \quad \psi_2 = \nu_{eR}, \quad \psi_3 = e_R^- \quad (2.6)$$

546 the charged fermionic currents are given by

$$J_\mu \equiv J_\mu^+ = \bar{\nu}_{eL} \gamma_\mu e_L, \quad J_\mu^\dagger \equiv J_\mu^- = \bar{e}_L \gamma_\mu \nu_{eL} \quad (2.7)$$

547 and the free Lagrangian is given by

$$\mathcal{L}_0 = \sum_{j=1}^3 i\bar{\psi}_j(x) \gamma^\mu \partial_\mu \psi_j(x). \quad (2.8)$$

548 Mass terms are included directly in the QED and QCD free Lagrangians since they

549 preserve the invariance under the symmetry transformations involved which treat
 550 left-handed and right-handed similarly, however mass terms of the form

$$m_W^2 W_\mu^\dagger(x) W^\mu(x) + \frac{1}{2} m_Z^2 Z_\mu(x) Z^\mu(x) - m_e \bar{\psi}_e(x) \psi_e(x) \quad (2.9)$$

551 which represent the mass of W^\pm , Z and electrons, are not invariant under G trans-
 552 formations, therefore the gauge fields described by the EWI are in principle massless.

553

554 Experiments have shown that the gauge fields are not massless; however, they have
 555 to acquire mass through a mechanism compatible with the gauge invariance; that
 556 mechanism is known as the “Higgs mechanism” and will be considered later in this
 557 section. The global transformations in the combined symmetry group G can be
 558 written as

$$\begin{aligned} \psi_1(x) &\xrightarrow{G} \psi'_1(x) \equiv U_Y U_L \psi_1(x), \\ \psi_2(x) &\xrightarrow{G} \psi'_2(x) \equiv U_Y \psi_2(x), \\ \psi_3(x) &\xrightarrow{G} \psi'_3(x) \equiv U_Y \psi_3(x) \end{aligned} \quad (2.10)$$

559 where U_L represent the $SU(2)_L$ transformation acting only on the weak isospin dou-
 560 blet and U_Y represent the $U(1)_Y$ transformation acting on all the weak isospin mul-
 561 tiplets. Explicitly

$$U_L \equiv \exp\left(i \frac{\sigma_i}{2} \alpha^i\right), \quad U_Y \equiv \exp(i y_i \beta) \quad (i = 1, 2, 3) \quad (2.11)$$

562 with σ_i the Pauli matrices and y_i the weak hypercharges. In order to promote the
 563 transformations from global to local while keeping the invariance, it is required that

564 $\alpha^i = \alpha^i(x)$, $\beta = \beta(x)$ and the replacement of the ordinary derivatives by the covariant
 565 derivatives

$$\begin{aligned} D_\mu \psi_1(x) &\equiv \left[\partial_\mu + ig\sigma_i W_\mu^i(x)/2 + ig'y_1 B_\mu(x) \right] \psi_1(x) \\ D_\mu \psi_2(x) &\equiv \left[\partial_\mu + ig'y_2 B_\mu(x) \right] \psi_2(x) \\ D_\mu \psi_3(x) &\equiv \left[\partial_\mu + ig'y_3 B_\mu(x) \right] \psi_3(x) \end{aligned} \quad (2.12)$$

566 introducing in this way four gauge fields, $W_\mu^i(x)$ and $B_\mu(x)$, in the process. The
 567 covariant derivatives (eqn 2.12) are required to transform in the same way as fermion
 568 fields $\psi_i(x)$ themselves, therefore, the gauge fields transform as:

$$\begin{aligned} B_\mu(x) &\xrightarrow{G} B'_\mu(x) \equiv B_\mu(x) - \frac{1}{g'} \partial_\mu \beta(x) \\ W_\mu^i(x) &\xrightarrow{G} W_\mu^{i\prime}(x) \equiv W_\mu^i(x) - \frac{i}{g} \partial_\mu \alpha_i(x) - \varepsilon_{ijk} \alpha_i(x) W_\mu^j(x). \end{aligned} \quad (2.13)$$

569 The G invariant version of the Lagrangian density 2.8 can be written as

$$\mathcal{L}_0 = \sum_{j=1}^3 i\bar{\psi}_j(x) \gamma^\mu D_\mu \psi_j(x) \quad (2.14)$$

570 where free massless fermion and gauge fields and fermion-gauge boson interactions
 571 are included. The EWI Lagrangian density must additionally include kinetic terms
 572 for the gauge fields (\mathcal{L}_G) which are built from the field strengths, according to

$$B_{\mu\nu}(x) \equiv \partial_\mu B_\nu - \partial_\nu B_\mu \quad (2.15)$$

$$W_{\mu\nu}^i(x) \equiv \partial_\mu W_\nu^i(x) - \partial_\nu W_\mu^i(x) - g\varepsilon^{ijk}W_\mu^j W_\nu^k \quad (2.16)$$

573 the last term in eqn. 2.16 is added in order to hold the gauge invariance; therefore,

$$\mathcal{L}_G = -\frac{1}{4}B_{\mu\nu}(x)B^{\mu\nu}(x) - \frac{1}{4}W_{\mu\nu}^i(x)W_i^{\mu\nu}(x) \quad (2.17)$$

574 which contains not only the free gauge fields contributions, but also the gauge fields
575 self-interactions and interactions among them.

576

577 The three weak isospin conserved currents resulting from the $SU(2)_L$ symmetry are
578 given by

$$J_\mu^i(x) = \frac{1}{2}\bar{\psi}_1(x)\gamma_\mu\sigma^i\psi_1(x) \quad (2.18)$$

579 while the weak hypercharge conserved current resulting from the $U(1)_Y$ symmetry is
580 given by

$$J_\mu^Y = \sum_{j=1}^3 \bar{\psi}_j(x)\gamma_\mu y_j\psi_j(x) \quad (2.19)$$

581 In order to evaluate the electroweak interactions modeled by an isos triplet field W_μ^i
582 which couples to isospin currents J_μ^i with strength g and additionally the singlet
583 field B_μ which couples to the weak hypercharge current J_μ^Y with strength $g'/2$. The
584 interaction Lagrangian density to be considered is

$$\mathcal{L}_I = -g J^{i\mu}(x) W_\mu^i(x) - \frac{g'}{2} J^{Y\mu}(x) B_\mu(x) \quad (2.20)$$

585 Note that the weak isospin currents are not the same as the charged fermionic currents
 586 that were used to describe the WI (eqn 2.7), since the weak isospin eigenstates are
 587 not the same as the mass eigenstates, but they are closely related

$$J_\mu = \frac{1}{2}(J_\mu^1 + iJ_\mu^2), \quad J_\mu^\dagger = \frac{1}{2}(J_\mu^1 - iJ_\mu^2). \quad (2.21)$$

588 The same happens with the gauge fields W_μ^i which are related to the mass eigenstates
 589 W^\pm by

$$W_\mu^+ = \frac{1}{\sqrt{2}}(W_\mu^1 - iW_\mu^2), \quad W_\mu^- = \frac{1}{\sqrt{2}}(W_\mu^1 + iW_\mu^2). \quad (2.22)$$

590 The fact that there are three weak isospin conserved currents is an indication that in
 591 addition to the charged fermionic currents, which couple charged to neutral leptons,
 592 there should be a neutral fermionic current that does not involve electric charge
 593 exchange; therefore, it couples neutral fermions or fermions of the same electric charge.
 594 The third weak isospin current contains a term that is similar to the electromagnetic
 595 current (j_μ^{em}), indicating that there is a relation between them and resembling the
 596 Gell-Mann-Nishijima formula 2.2 adapted to electroweak interactions

$$Q = T_3 + \frac{Y_W}{2}. \quad (2.23)$$

597 Just as Q generates the $U(1)_{em}$ symmetry, the weak hypercharge generates the $U(1)_Y$
 598 symmetry as said before. It is possible to write the relationship in terms of the currents
 599 as

$$j_\mu^{em} = J_\mu^3 + \frac{1}{2} J_\mu^Y. \quad (2.24)$$

600 The neutral gauge fields W_μ^3 and B_μ cannot be directly identified with the Z and the
 601 photon fields since the photon interacts similarly with left and right-handed fermions;
 602 however, they are related through a linear combination given by

$$\begin{aligned} A_\mu &= B_\mu \cos \theta_W + W_\mu^3 \sin \theta_W \\ Z_\mu &= -B_\mu \sin \theta_W + W_\mu^3 \cos \theta_W \end{aligned} \quad (2.25)$$

603 where θ_W is known as the “Weinberg angle.” The interaction Lagrangian is now given
 604 by

$$\mathcal{L}_I = -\frac{g}{\sqrt{2}}(J^\mu W_\mu^+ + J^{\mu\dagger} W_\mu^-) - \left(g \sin \theta_W J_\mu^3 + g' \cos \theta_W \frac{J_\mu^Y}{2}\right) A^\mu - \left(g \cos \theta_W J_\mu^3 - g' \sin \theta_W \frac{J_\mu^Y}{2}\right) Z^\mu \quad (2.26)$$

605 the first term is the weak charged current interaction, while the second term is the
 606 electromagnetic interaction under the condition

$$g \sin \theta_W = g' \cos \theta_W = e, \quad \frac{g'}{g} = \tan \theta_W \quad (2.27)$$

607 contained in the eqn.2.24; the third term is the neutral weak current.

608

609 Note that the neutral fields transformation given by the eqn. 2.25 can be written in
 610 terms of the coupling constants g and g' as:

$$A_\mu = \frac{g' W_\mu^3 + g B_\mu}{\sqrt{g^2 + g'^2}}, \quad Z_\mu = \frac{g W_\mu^3 - g' B_\mu}{\sqrt{g^2 + g'^2}} \quad (2.28)$$

611 So far, the Lagrangian density describing the non-massive EWI is:

$$\mathcal{L}_{nmEWI} = \mathcal{L}_0 + \mathcal{L}_G \quad (2.29)$$

612 where fermion and gauge fields have been considered massless because their regular
 613 mass terms are manifestly non invariant under G transformations; therefore, masses
 614 have to be generated in a gauge invariant way. The mechanism by which this goal is
 615 achieved is known as the “Higgs mechanism” and is closely connected to the concept
 616 of “spontaneous symmetry breaking.”

617 2.3.1 Spontaneous symmetry breaking (SSB)

618 Figure 2.6 left shows a steel nail (top) which is subject to an external force; the form
 619 of the potential energy is also shown (bottom).

620

621 Before reaching the critical force value, the system has rotational symmetry with re-
 622 spect to the nail axis; however, after the critical force value is reached the nail buckles
 623 (top right). The form of the potential energy (bottom right) changes, preserving its
 624 rotational symmetry although its minima does not exhibit that rotational symmetry
 625 any longer. Right before the nail buckles there is no indication of the direction the
 626 nail will bend because any of the directions are equivalent, but once the nail bends,
 627 choosing a direction, an arbitrary minimal energy state (ground state) is selected and
 628 it does not share the system’s rotational symmetry. This mechanism for reaching an
 629 asymmetric ground state is known as “*spontaneous symmetry breaking*”.

630 The lesson from this analysis is that the way to introduce the SSB mechanism into a
 631 system is by adding the appropriate potential to it.

632

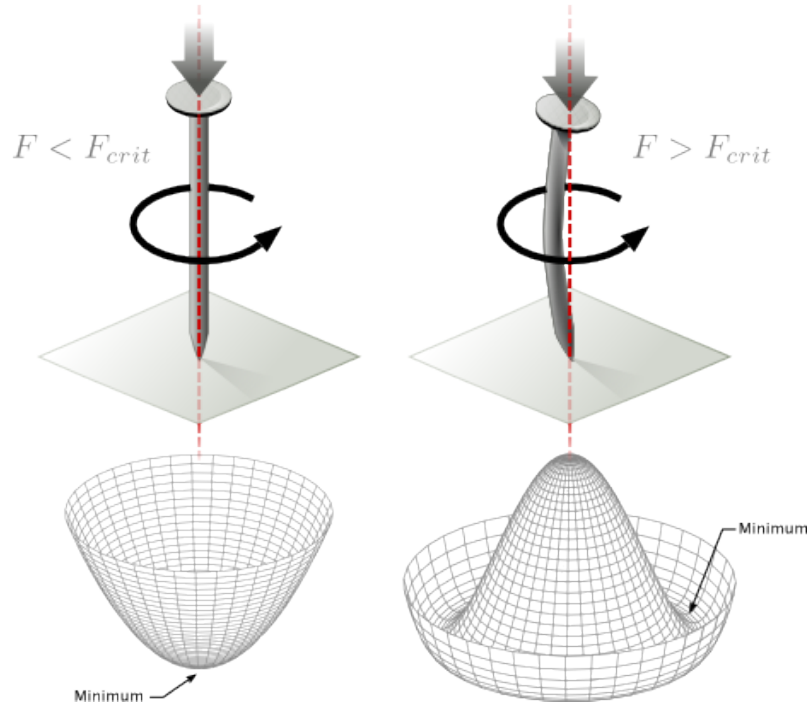


Figure 2.6: Spontaneous symmetry breaking mechanism. The steel nail, subject to an external force (top left), has rotational symmetry with respect to its axis. When the external force overcomes a critical value the nail buckles (top right) choosing a minimal energy state (ground state) and thus “*breaking spontaneously the rotational symmetry*”. The potential energy (bottom) changes but holds the rotational symmetry; however, an infinite number of asymmetric ground states are generated and circularly distributed in the bottom of the potential [27].

633 Figure 2.7 shows a plot of the potential $V(\phi)$ in the case of a scalar field ϕ

$$V(\phi) = \mu^2 \phi^\dagger \phi + \lambda (\phi^\dagger \phi)^2 \quad (2.30)$$

634 If $\mu^2 > 0$ the potential has only one minimum at $\phi = 0$ and describes a scalar field
 635 with mass μ . If $\mu^2 < 0$ the potential has a local maximum at $\phi = 0$ and two minima
 636 at $\phi = \pm\sqrt{-\mu^2/\lambda}$ which enables the SSB mechanism to work.

637

638 In the case of a complex scalar field $\phi(x)$

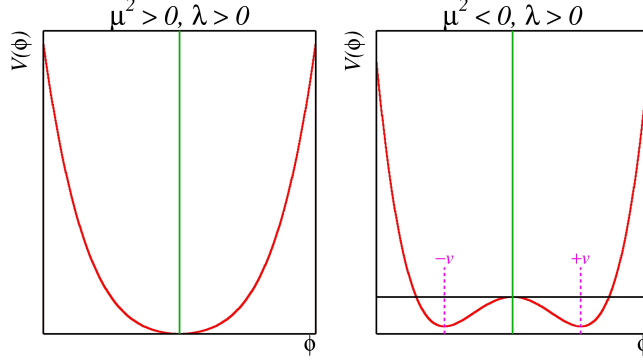


Figure 2.7: Shape of the potential $V(\phi)$ for $\lambda > 0$ and: $\mu^2 > 0$ (left) and $\mu^2 < 0$ (right). The case $\mu^2 < 0$ corresponds to the potential suitable for introducing the SSB mechanism by choosing one of the two ground states which are connected via reflection symmetry. [27].

$$\phi(x) = \frac{1}{\sqrt{2}}(\phi_1 + i\phi_2) \quad (2.31)$$

639 the Lagrangian (invariant under global $U(1)$ transformations) is given by

$$\mathcal{L} = (\partial_\mu \phi)^\dagger (\partial^\mu \phi) - V(\phi), \quad V(\phi) = \mu^2 \phi^\dagger \phi + \lambda (\phi^\dagger \phi)^2 \quad (2.32)$$

640 where an appropriate potential has been added in order to introduce the SSB.

641

642 As seen in figure 2.8, the potential has now an infinite number of minima circularly
 643 distributed along the ξ -direction which makes possible the occurrence of the SSB by
 644 choosing an arbitrary ground state; for instance, $\xi = 0$, i.e. $\phi_1 = v, \phi_2 = 0$

$$\phi_0 = \frac{v}{\sqrt{2}} \exp(i\xi) \xrightarrow{\text{SSB}} \phi_0 = \frac{v}{\sqrt{2}} \quad (2.33)$$

645 As usual, excitations over the ground state are studied by making an expansion about

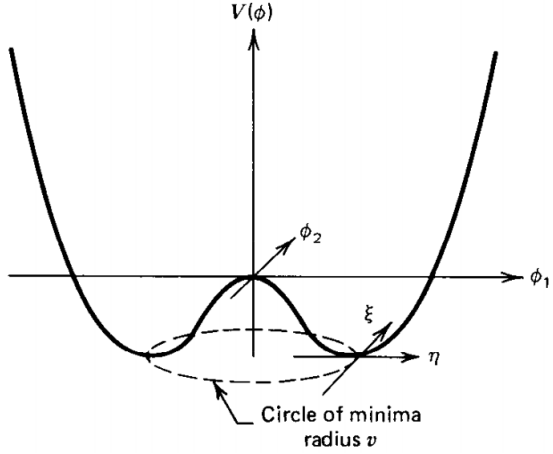


Figure 2.8: Potential for complex scalar field. There is a circle of minima of radius v along the ξ -direction [6].

646 it; thus, the excitation can be parametrized as:

$$\phi(x) = \frac{1}{\sqrt{2}}(v + \eta(x) + i\xi(x)) \quad (2.34)$$

647 which when substituted into eqn. 2.32 produces a Lagrangian in terms of the new
648 fields η and ξ

$$\mathcal{L}' = \frac{1}{2}(\partial_\mu \xi)^2 + \frac{1}{2}(\partial_\mu \eta)^2 + \mu^2 \eta^2 - V(\phi_0) - \lambda v \eta (\eta^2 + \xi^2) - \frac{\lambda}{4}(\eta^2 + \xi^2)^2 \quad (2.35)$$

649 where the last two terms represent the interactions and self-interaction between the
650 two fields η and ξ . The particular feature of the SSB mechanism is revealed when
651 looking to the first three terms of \mathcal{L}' . Before the SSB, only the massless ϕ field is
652 present in the system; after the SSB there are two fields of which the η -field has
653 acquired mass $m_\eta = \sqrt{-2\mu^2}$ while the ξ -field is still massless (see figure 2.9).

654

655 Thus, the SSB mechanism serves as a method to generate mass but as a side effect a

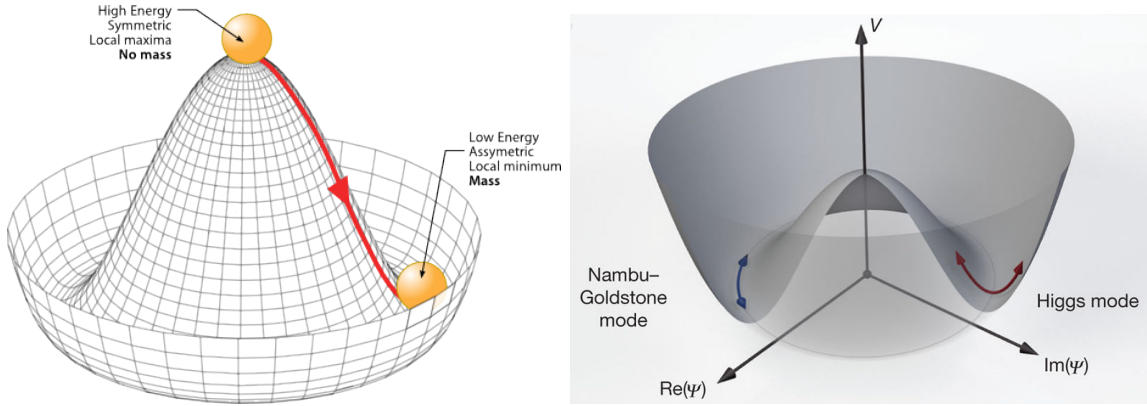


Figure 2.9: SSB mechanism for a complex scalar field [27, 28].

656 *massless field is introduced in the system.* This fact is known as the Goldstone theorem
 657 and states that a massless scalar field appears in the system for each continuous
 658 symmetry spontaneously broken. Another version of the Goldstone theorem states
 659 that “*if a Lagrangian is invariant under a continuous symmetry group G , but the*
 660 *vacuum is only invariant under a subgroup $H \subset G$, then there must exist as many*
 661 *massless spin-0 particles (Nambu-Goldstone bosons) as broken generators.*” [26] The
 662 Nambu-Goldstone boson can be understood considering that the potential in the ξ -
 663 direction is flat so excitations in that direction are not energy consuming and thus
 664 represent a massless state.

665 2.3.2 Higgs mechanism

666 When the SSB mechanism is introduced in the formulation of the EWI in an attempt
 667 to generate the mass of the so far massless gauge bosons and fermions, an interesting
 668 effect is revealed. In order to keep the G symmetry group invariance and generate
 669 the mass of the EW gauge bosons, a G invariant Lagrangian density (\mathcal{L}_S) has to be
 670 added to the non massive EWI Lagrangian (eqn. 2.29)

$$\mathcal{L}_S = (D_\mu \phi)^\dagger (D^\mu \phi) - \mu^2 \phi^\dagger \phi - \lambda (\phi^\dagger \phi)^2, \quad \lambda > 0, \mu^2 < 0 \quad (2.36)$$

$$D_\mu \phi = \left(i\partial_\mu - g \frac{\sigma_i}{2} W_\mu^i - g' \frac{Y}{2} B_\mu \right) \phi \quad (2.37)$$

671 ϕ has to be an isospin doublet of complex scalar fields so it preserves the G invariance;
 672 thus ϕ can be defined as:

$$\phi = \begin{pmatrix} \phi^+ \\ \phi^0 \end{pmatrix} \equiv \frac{1}{\sqrt{2}} \begin{pmatrix} \phi_1 + i\phi_2 \\ \phi_3 + i\phi_4 \end{pmatrix}. \quad (2.38)$$

673 The minima of the potential are defined by

$$\phi^\dagger \phi = \frac{1}{2} (\phi_1^2 + \phi_2^2 + \phi_3^2 + \phi_4^2) = -\frac{\mu^2}{2\lambda}. \quad (2.39)$$

674 The choice of the ground state is critical. By choosing a ground state, invariant under
 675 $U(1)_{em}$ gauge symmetry, the photon will remain massless and the W^\pm and Z bosons
 676 masses will be generated which is exactly what is needed. In that sense, the best
 677 choice corresponds to a weak isospin doublet with $T_3 = -1/2$, $Y_W = 1$ and $Q = 0$
 678 which defines a ground state with $\phi_1 = \phi_2 = \phi_4$ and $\phi_3 = v$:

$$\phi_0 \equiv \frac{1}{\sqrt{2}} \begin{pmatrix} 0 \\ v \end{pmatrix}, \quad v^2 \equiv -\frac{\mu^2}{\lambda}. \quad (2.40)$$

679 where the vacuum expectation value v is fixed by the Fermi coupling G_F according
 680 to $v = (\sqrt{2}G_F)^{1/2} \approx 246$ GeV.

681

682 The G symmetry has been broken and three Nambu-Goldstone bosons will appear.

683 The next step is to expand ϕ about the chosen ground state as:

$$\phi(x) = \frac{1}{\sqrt{2}} \exp\left(\frac{i}{v} \sigma_i \theta^i(x)\right) \begin{pmatrix} 0 \\ v + H(x) \end{pmatrix} \approx \frac{1}{\sqrt{2}} \begin{pmatrix} \theta_1(x) + i\theta_2(x) \\ v + H(x) - i\theta_3(x) \end{pmatrix} \quad (2.41)$$

684 to describe fluctuations from the ground state ϕ_0 . The fields $\theta_i(x)$ represent the
 685 Nambu-Goldstone bosons while $H(x)$ is known as “higgs field.” The fundamental
 686 feature of the parametrization used is that the dependence on the $\theta_i(x)$ fields is
 687 factored out in a global phase that can be eliminated by taking the physical “unitary
 688 gauge” $\theta_i(x) = 0$. Therefore the expansion about the ground state is given by:

$$\phi(x) \frac{1}{\sqrt{2}} \begin{pmatrix} 0 \\ v + H(x) \end{pmatrix} \quad (2.42)$$

689 which when substituted into \mathcal{L}_S (eqn. 2.36) results in a Lagrangian containing the now
 690 massive three gauge bosons W^\pm, Z , one massless gauge boson (photon) and the new
 691 Higgs field (H). The three degrees of freedom corresponding to the Nambu-Goldstone
 692 bosons are now integrated into the massive gauge bosons as their longitudinal po-
 693 larizations which were not available when they were massless particles. The effect
 694 by which vector boson fields acquire mass after an spontaneous symmetry breaking,
 695 but without an explicit gauge invariance breaking is known as the “*Higgs mechanism*”.

696

697 The mechanism was proposed by three independent groups: F.Englert and R.Brout
 698 in August 1964 [29], P.Higgs in October 1964 [30] and G.Guralnik, C.Hagen and
 699 T.Kibble in November 1964 [31]; however, its importance was not realized until
 700 S.Glashow [22], A.Salam [23] and S.Weinberg [24], independently, proposed that elec-
 701 tromagnetic and weak interactions are two manifestations of a more general interac-
 702 tion called “electroweak interaction” in 1967.

703 **2.3.3 Masses of the gauge bosons**

704 The mass of the gauge bosons is extracted by evaluating the kinetic part of Lagrangian
 705 \mathcal{L}_S in the ground state (known also as the vacuum expectation value), i.e.,

$$\left| \left(\partial_\mu - ig \frac{\sigma_i}{2} W_\mu^i - i \frac{g'}{2} B_\mu \right) \phi_0 \right|^2 = \left(\frac{1}{2} v g \right)^2 W_\mu^+ W^{-\mu} + \frac{1}{8} v^2 (W_\mu^3, B_\mu) \begin{pmatrix} g^2 & -gg' \\ -gg' & g'^2 \end{pmatrix} \begin{pmatrix} W^{3\mu} \\ B^\mu \end{pmatrix} \quad (2.43)$$

706 comparing with the typical mass term for a charged boson $M_W^2 W^+ W^-$

$$M_W = \frac{1}{2} v g. \quad (2.44)$$

The second term in the right side of the eqn.2.43 comprises the masses of the neutral bosons, but it needs to be written in terms of the gauge fields Z_μ and A_μ in order to be compared to the typical mass terms for neutral bosons, therefore using eqn. 2.28

$$\begin{aligned} \frac{1}{8} v^2 [g^2 (W_\mu^3)^2 - 2gg' W_\mu^3 B^\mu + g'^2 B_\mu^2] &= \frac{1}{8} v^2 [g W_\mu^3 - g' B_\mu]^2 + 0[g' W_\mu^3 + g B_\mu]^2 \quad (2.45) \\ &= \frac{1}{8} v^2 [\sqrt{g^2 + g'^2} Z_\mu]^2 + 0[\sqrt{g^2 + g'^2} A_\mu]^2 \end{aligned}$$

707 and then

$$M_Z = \frac{1}{2} v \sqrt{g^2 + g'^2}, \quad M_A = 0 \quad (2.46)$$

708 **2.3.4 Masses of the fermions**

709 The lepton mass terms can be generated by introducing a gauge invariant Lagrangian
 710 term describing the Yukawa coupling between the lepton field and the Higgs field

$$\mathcal{L}_{Yl} = -G_l \left[(\bar{\nu}_l, \bar{l})_L \begin{pmatrix} \phi^+ \\ \phi^0 \end{pmatrix} l_R + \bar{l}_R (\phi^-, \bar{\phi}^0) \begin{pmatrix} \nu_l \\ l \end{pmatrix}_L \right], \quad l = e, \mu, \tau. \quad (2.47)$$

711 After the SSB and replacing the usual field expansion about the ground state (eqn.2.40)
 712 into \mathcal{L}_{Yl} , the mass term arises

$$\mathcal{L}_{Yl} = -m_l (\bar{l}_L l_R + \bar{l}_R l_L) - \frac{m_l}{v} (\bar{l}_L l_R + \bar{l}_R l_L) H = -m_l \bar{l} l \left(1 + \frac{H}{v} \right) \quad (2.48)$$

713

$$m_l = \frac{G_l}{\sqrt{2}} v \quad (2.49)$$

714 where the additional term represents the lepton-Higgs interaction. The quark masses
 715 are generated in a similar way as lepton masses but for the upper member of the
 716 quark doublet a different Higgs doublet is needed:

$$\phi_c = -i\sigma_2 \phi^* = \begin{pmatrix} -\bar{\phi}^0 \\ \phi^- \end{pmatrix}. \quad (2.50)$$

717 Additionally, given that the quark isospin doublets are not constructed in terms of
 718 the mass eigenstates but in terms of the flavor eigenstates, as shown in table2.5, the
 719 coupling parameters will be related to the CKM matrix elements; thus the quark
 720 Lagrangian is given by:

$$\mathcal{L}_{Yq} = -G_d^{i,j} (\bar{u}_i, \bar{d}'_i)_L \begin{pmatrix} \phi^+ \\ \phi^0 \end{pmatrix} d_{jR} - G_u^{i,j} (\bar{u}_i, \bar{d}'_i)_L \begin{pmatrix} -\bar{\phi}^0 \\ \phi^- \end{pmatrix} u_{jR} + h.c. \quad (2.51)$$

721 with $i,j=1,2,3$. After SSB and expansion about the ground state, the diagonal form

722 of \mathcal{L}_{Yq} is:

$$\mathcal{L}_{Yq} = -m_d^i \bar{d}_i d_i \left(1 + \frac{H}{v}\right) - m_u^i \bar{u}_i u_i \left(1 + \frac{H}{v}\right) \quad (2.52)$$

723 Fermion masses depend on arbitrary couplings G_l and $G_{u,d}$ and are not predicted by
724 the theory.

725 2.3.5 The Higgs field

726 After the characterization of the fermions and gauge bosons as well as their interac-
727 tions, it is necessary to characterize the Higgs field itself. The Lagrangian \mathcal{L}_S in eqn.
728 2.36 written in terms of the gauge bosons is given by

$$\mathcal{L}_S = \frac{1}{4} \lambda v^4 + \mathcal{L}_H + \mathcal{L}_{HV} \quad (2.53)$$

729

$$\mathcal{L}_H = \frac{1}{2} \partial_\mu H \partial^\mu H - \frac{1}{2} m_H^2 H^2 - \frac{1}{2v} m_H^2 H^3 - \frac{1}{8v^2} m_H^2 H^4 \quad (2.54)$$

730

$$\mathcal{L}_{HV} = m_H^2 W_\mu^+ W^{\mu-} \left(1 + \frac{2}{v} H + \frac{2}{v^2} H^2\right) + \frac{1}{2} m_Z^2 Z_\mu Z^\mu \left(1 + \frac{2}{v} H + \frac{2}{v^2} H^2\right) \quad (2.55)$$

731 The mass of the Higgs boson is deduced as usual from the mass term in the Lagrangian
732 resulting in:

$$m_H = \sqrt{-2\mu^2} = \sqrt{2\lambda}v \quad (2.56)$$

733 however, it is not predicted by the theory either. The experimental efforts to find
734 the Higgs boson, carried out by the “Compact Muon Solenoid (CMS)” experiment
735 and the “A Toroidal LHC AppartuS (ATLAS)” experiments at the “Large Hadron
736 Collider(LHC)”, gave great results by July of 2012 when the discovery of a new
737 particle compatible with the Higgs boson predicted by the electroweak theory [32, 33]
738 was announced. Although at the announcement time there were some reservations
739 about calling the new particle the “Higgs boson”, today this name is widely accepted.

740 The Higgs mass measurement, reported by both experiments [34], is in table 2.8.

Property	Value
Electric charge	0
Colour charge	0
Spin	0
Weak isospin	-1/2
Weak hypercharge	1
Parity	1
Mass (GeV/c^2)	$125.09 \pm 0.21 \text{ (stat.)} \pm 0.11 \text{ (syst.)}$

Table 2.8: Higgs boson properties. Higgs mass is not predicted by the theory and the value here corresponds to the experimental measurement.

741

742 2.3.6 Production of Higgs bosons at LHC

743 At LHC, Higgs boson is produced as a result of the collision of two counter-rotating
 744 protons beams. A detailed description of the LHC machine will be presented in
 745 chapter 3. “The total cross section” is a parameter that quantifies the number of pp
 746 collisions that happen when a number of protons are fired at each other. Different
 747 results can be obtained after a pp collision and for each one the “cross section” is
 748 defined as the number of pp collisions that conclude in that particular result with
 749 respect to the number of protons fired at each other.

750 Protons are composed of quarks and these quarks are bound by gluons; however,
 751 what is commonly called the quark content of the proton makes reference to the
 752 valence quarks. A sea of quarks and gluons is also present inside the proton as repre-
 753 sented in figure 2.10. In a proton-proton (pp) collision, the constituents (quarks and
 754 gluons) are those who collide. The pp cross section depends on the momentum of
 755 the colliding particles, reason for which it is needed to know how the momentum is
 756 distributed inside the proton. Quarks and gluons are known as partons and the func-
 757 tions that describe how the proton momentum is distributed among partons inside it

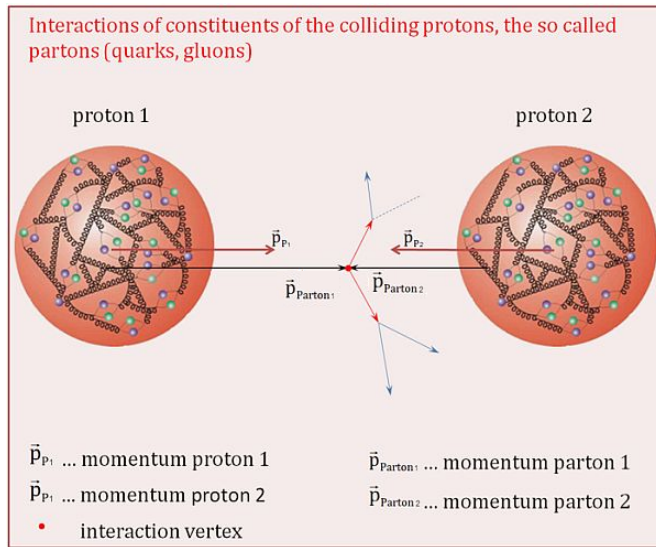


Figure 2.10: Proton-proton collision. Protons are composed of 3 valence quarks, a sea of quarks and gluons; therefore in a proton-proton collision, quarks and gluons are those who collide. [35].

758 are called “parton distribution functions (PDFs)”; PDFs are determined from experi-

759 mental data obtained in experiments where the internal structure of hadrons is tested.

760

In addition, in physics, a common approach to study complex systems consists in starting with a simpler version of them, for which a well known description is available, and add an additional “perturbation” which represents a small deviation from the known behavior. If the perturbation is small enough, the physical quantities associated with the perturbed system are expressed as a series of corrections to those of the simpler system; therefore, the more terms are considered in the series (the higher order in the perturbation series), the more precise is the the description of the complex system.

769

770 This thesis explores the Higgs production at LHC; therefore the overview presented
771 here will be oriented specifically to the production mechanisms after pp collisions at

772 LHC.

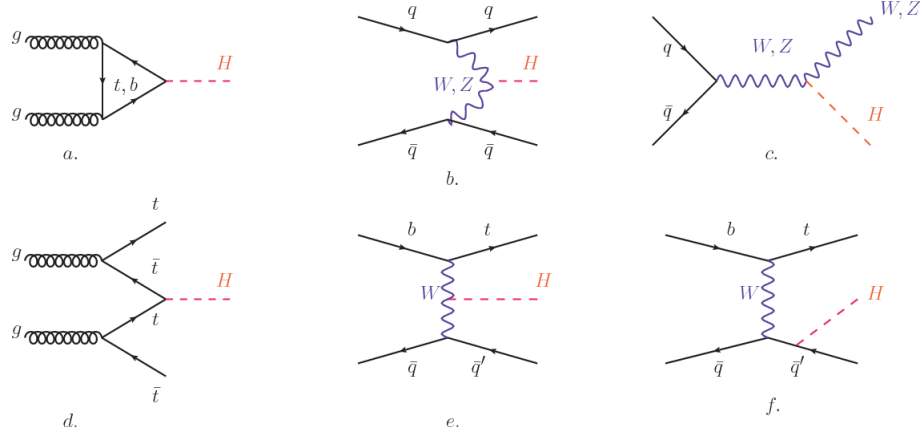


Figure 2.11: Main Higgs boson production mechanism Feynman diagrams. a. gluon-gluon fusion, b. vector boson fusion (VBF), c. Higgs-strahlung, d. Associated production with a top or bottom quark pair, e-f. associated production with a single top quark.

773 Figure 2.11 shows the Feynman diagrams for the leading order (first order) Higgs
 774 production processes at LHC, while the cross section for Higgs production as a func-
 775 tion of the center of mass-energy (\sqrt{s}) for pp collisions is showed in figure 2.12 left.
 776 The tags NLO (next to leading order), NNLO (next to next to leading order) and
 777 N3LO (next to next to next to leading order) make reference to the order at which
 778 the perturbation series have been considered.

779 As shown in eqns 2.47, 2.51 and 2.55, the strength of the Higgs-fermion interaction
 780 is proportional to the fermion mass while the strength of the Higgs-gauge boson
 781 interaction is proportional to the square of the gauge boson mass, which implies
 782 that the Higgs production and decay mechanisms are dominated by couplings $H -$
 783 (W, Z, t, b, τ) .

784 The main production mechanism is the gluon fusion (figure 2.11a and $pp \rightarrow H$ in figure
 785 2.12) given that gluons carry the highest fraction of momentum of the protons in pp
 786 colliders. Since the Higgs boson does not couple to gluons, the mechanism proceeds
 787 through the exchange of a virtual top-quark loop given that for it the coupling is

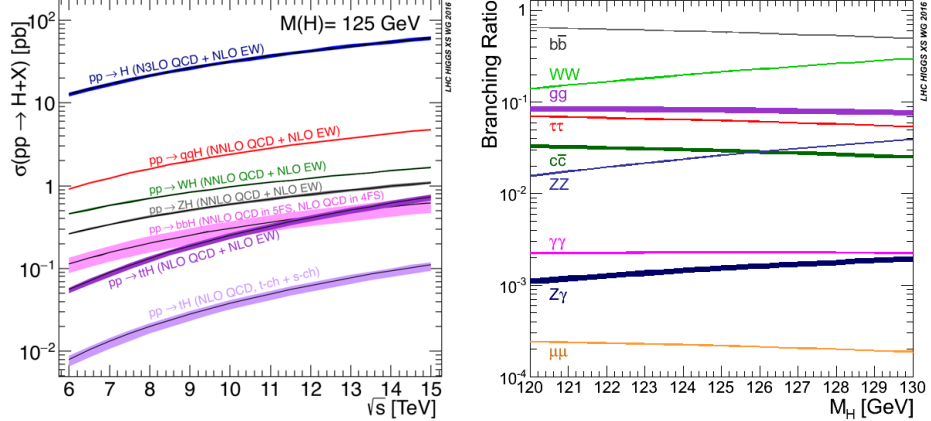


Figure 2.12: Higgs boson production cross sections (left) and decay branching ratios (right) for the main mechanisms. The VBF is indicated as qqH [36].

the biggest. Note that in this process, the Higgs boson is produced alone, which makes this mechanism experimentally clean when combined with the two-photon or the four-lepton decay channels (see section 2.3.7).

Vector boson fusion (figure 2.11b and $pp \rightarrow qqH$ in figure 2.12) has the second largest production cross section. The scattering of two fermions is mediated by a weak gauge boson which later emits a Higgs boson. In the final state, the two fermions tend to be located in a particular region of the detector which is used as a signature when analyzing the datasets provided by the experiments. More details about how to identify events of interest in an analysis will be given in chapter 6.

The next production mechanism is Higgs-strahlung (figure 2.11c and $pp \rightarrow WH, pp \rightarrow ZH$ in figure 2.12) where two fermions annihilate to form a weak gauge boson. If the initial fermions have enough energy, the emergent boson eventually will emit a Higgs boson.

The associated production with a top or bottom quark pair and the associated production with a single top quark (figure 2.11d-f and $pp \rightarrow bbH, pp \rightarrow t\bar{t}H, pp \rightarrow tH$ in figure 2.12) have a smaller cross section than the main three mechanisms above,

804 but they provide a good opportunity to test the Higgs-top coupling. The analysis
 805 reported in this thesis is developed using these production mechanisms. A detailed
 806 description of the tH mechanism will be given in section 2.4.

807 2.3.7 Higgs boson decay channels

808 When a particle can decay through several modes, also known as channels, the
 809 probability of decaying through a given channel is quantified by the “branching ratio
 810 (BR)” of the decay channel; thus, the BR is defined as the ratio of number of decays
 811 going through that given channel to the total number of decays. In regard to the
 812 Higgs boson decay, the BR can be predicted with accuracy once the Higgs mass is
 813 known [37, 38]. In figure 2.12 right, a plot of the BR as a function of the Higgs mass
 814 is presented. The largest predicted BR corresponds to the $b\bar{b}$ pair decay channel (see
 815 table 2.9).

Decay channel	Branching ratio	Rel. uncertainty
$H \rightarrow b\bar{b}$	5.84×10^{-1}	$+3.2\% - 3.3\%$
$H \rightarrow W^+W^-$	2.14×10^{-1}	$+4.3\% - 4.2\%$
$H \rightarrow \tau^+\tau^-$	6.27×10^{-2}	$+5.7\% - 5.7\%$
$H \rightarrow ZZ$	2.62×10^{-2}	$+4.3\% - 4.1\%$
$H \rightarrow \gamma\gamma$	2.27×10^{-3}	$+5.0\% - 4.9\%$
$H \rightarrow Z\gamma$	1.53×10^{-3}	$+9.0\% - 8.9\%$
$H \rightarrow \mu^+\mu^-$	2.18×10^{-4}	$+6.0\% - 5.9\%$

Table 2.9: Predicted branching ratios and the relative uncertainty for a SM Higgs boson with $m_H = 125 GeV/c^2$. [9]

817 **2.4 Associated production of a Higgs boson and a
818 single Top quark.**

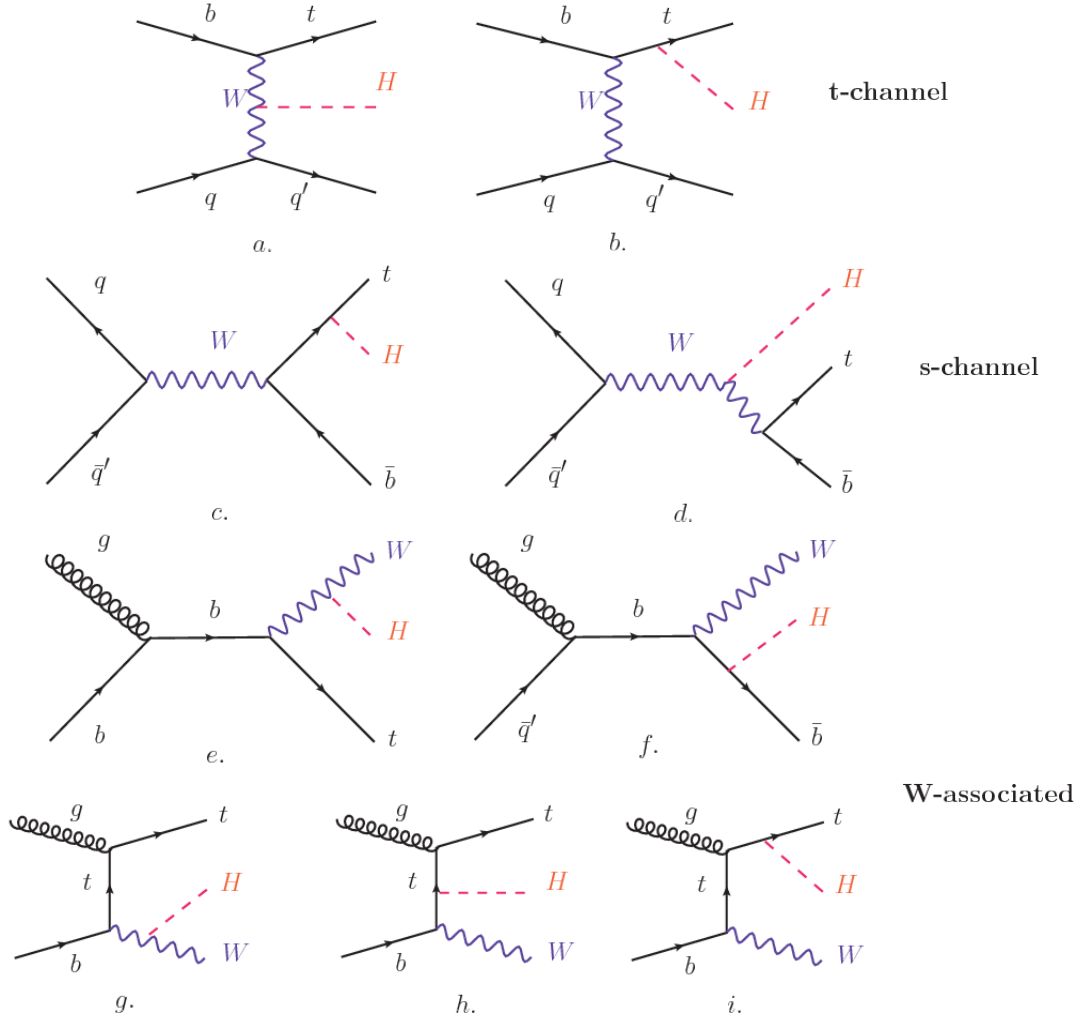


Figure 2.13: Associated Higgs boson production mechanism Feynman diagrams. a.,b. t-channel (tHq), c.,d. s-channel (tHb), e-i. W-associated.

819 Associated production of Higgs boson has been extensively studied [39–43]. While
820 measurements of the main Higgs production mechanisms rates are sensitive to the
821 strength of the Higgs coupling to W boson or top quark, they are not sensitive to the
822 relative sign between the two couplings. In this thesis, the Higgs boson production

mechanism explored is the associated production with a single top quark (*th*) which offers sensitiveness to the relative sign of the Higgs couplings to W boson and to top quark. The description given here is based on the reference [41]

826

827 A process where two incoming particles interact and produce a final state with two
 828 particles can proceed in three ways also called channels (see, for instance, figure 2.13
 829 ommiting the red line). The t-channel represents processes where an intermediate
 830 particle is emitted by one of the incoming particles and absorbed by the other. The
 831 s-channel represents processes where the two incoming particles merge into an inter-
 832 mediate particle which eventually will split into the particles in the final state. The
 833 third channel, u-channel, is similar to the t-channel but the two outgoing particles
 834 interchange their roles.

835

836 The *th* production, where Higgs boson can be radiated either from the top quark or
 837 from the W boson, is represented by the leading order Feynman diagrams in figure
 838 2.13. The cross section for the *th* process is calculated, as usual, summing over
 839 the contributions from the different feynman diagrams; therefore it depends on the
 840 interference between the contributions. In the SM, the interference for t-channel (tHq
 841 process) and W-associated (tHW process) production is destructive [39] resulting in
 842 the small cross sections presented in table 2.10.

tH production channel	Cross section (fb)
t-channel ($pp \rightarrow tHq$)	$70.79^{+2.99}_{-4.80}$
W-associated ($pp \rightarrow tHW$)	$15.61^{+0.83}_{-1.04}$
s-channel($pp \rightarrow tHb$)	$2.87^{+0.09}_{-0.08}$

Table 2.10: Predicted SM cross sections for *tH* production at $\sqrt{s} = 13$ TeV [44, 45].

843

844 While the s-channel contribution can be neglected, it will be shown that a deviation
 845 from the SM destructive interference would result in an enhancement of the th cross
 846 section compared to that in SM, which could be used to get information about the
 847 sign of the Higgs-top coupling [41, 42]. In order to describe th production processes,
 848 Feynman diagram 2.13b will be considered; there, the W boson is radiated by a
 849 quark in the proton and eventually it will interact with the b quark. In the high
 850 energy regime, the effective W approximation [46] allows to describe the process as
 851 the emmision of an approximately on-shell W and its hard scattering with the b
 852 quark; i.e. $Wb \rightarrow th$. The scattering amplitude for the process is given by

$$\mathcal{A} = \frac{g}{\sqrt{2}} \left[(\kappa_t - \kappa_V) \frac{m_t \sqrt{s}}{m_W v} A \left(\frac{t}{s}, \varphi; \xi_t, \xi_b \right) + \left(\kappa_V \frac{2m_W s}{v} \frac{1}{t} + (2\kappa_t - \kappa_V) \frac{m_t^2}{m_W v} \right) B \left(\frac{t}{s}, \varphi; \xi_t, \xi_b \right) \right], \quad (2.57)$$

853 where $\kappa_V \equiv g_{HVV}/g_{HVV}^{SM}$ and $\kappa_t \equiv g_{Ht}/g_{Ht}^{SM} = y_t/y_t^{SM}$ are scaling factors that quan-
 854 tify possible deviations of the couplings, Higgs-Vector boson (H-W) and Higgs-top
 855 (H-t) respectively, from the SM couplings; $s = (p_W + p_b)^2$, $t = (p_W - p_H)^2$, φ is the
 856 Higgs azimuthal angle around the z axis taken parallel to the direction of motion of
 857 the incoming W; A and B are funtions describing the weak interaction in terms of
 858 the chiral states of the quarks b and t . Terms that vanish in the high energy limit
 859 have been neglected as well as the Higgs and b quark masses⁸.

860

861 The scattering amplitude grows with energy like \sqrt{s} for $\kappa_V \neq \kappa_t$, in contrast to
 862 the SM ($\kappa_t = \kappa_V = 1$), where the first term in 2.57 cancels out and the amplitude
 863 is constant for large s ; therefore, a deviation from the SM predictions represents an
 864 enhancement in the tHq cross section. In particular, for a SM H-W coupling and a H-t

⁸ A detailed explanation of the structure and approximations used to derive \mathcal{A} can be found in reference [41]

865 coupling of inverted sign with respect to the SM ($\kappa_V = -\kappa_t = 1$) the tHq cross section
 866 is enhanced by a factor greater 10 as seen in the figure 2.14 taken from reference [41];
 867 reference [47] has reported similar enhancement results.

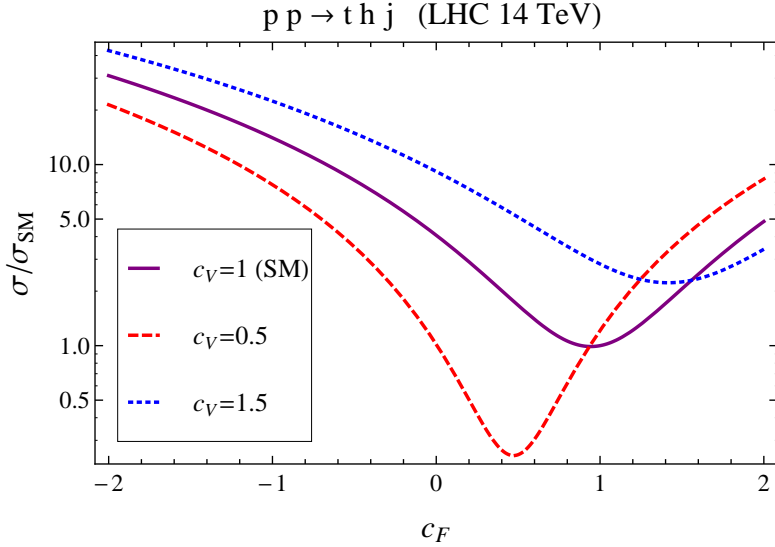


Figure 2.14: Cross section for tHq process as a function of κ_t , normalized to the SM, for three values of κ_V . In the plot c_f refers to the Higgs-fermion coupling which is dominated by the H-t coupling and represented here by κ_t . Solid, dashed and dotted lines correspond to $c_V \rightarrow \kappa_V = 1, 0.5, 1.5$ respectively. Note that for the SM ($\kappa_V = \kappa_t = 1$), the destructive effect of the interference is maximal.

868 A similar analysis is valid for the W-associated channel but, in that case, the inter-
 869 ference is more complicated since there are more than two contributions and an ad-
 870 ditional interference with the production of Higgs boson and a top pair process($t\bar{t}H$).
 871 The calculations are made using the so-called Diagram Removal (DR) technique where
 872 interfering diagrams are removed (or added) from the calculations in order to evaluate
 873 the impact of the removed contributions. DR1 was defined to neglect $t\bar{t}H$ interference
 874 while DR2 was defined to take $t\bar{t}H$ interference into account [48]. As shown in figure
 875 2.15, the tHW cross section is enhanced from about 15 fb (SM: $\kappa_{Htt} = 1$) to about
 876 150 fb ($\kappa_{Htt} = -1$). Differences between curves for DR1 and DR2 help to gauge the
 877 impact of the interference with $t\bar{t}H$.

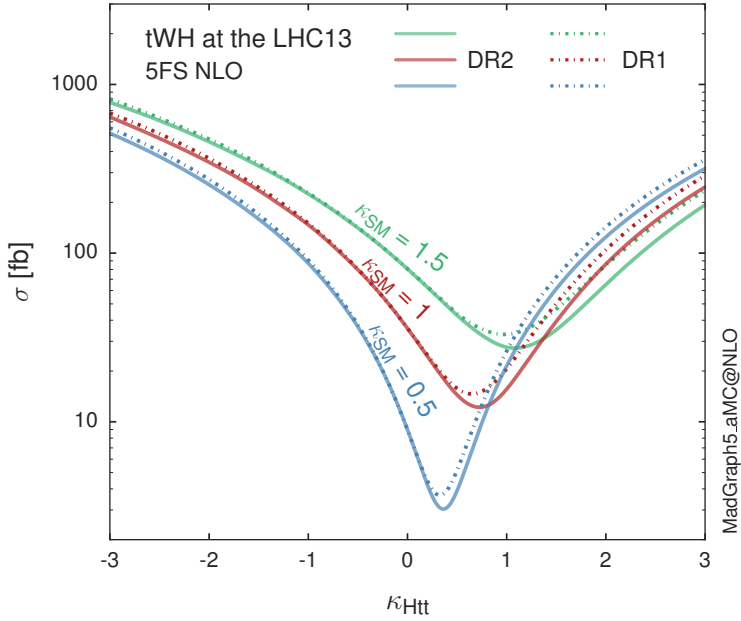


Figure 2.15: Cross section for tHW process as a function of κ_{Htt} , for three values of κ_{SM} at $\sqrt{s} = 13$ TeV. $\kappa_{Htt}^2 = \sigma_{Htt}/\sigma_{Htt}^{SM}$ is a simple rescaling of the SM Higgs interactions.

878 Results of the calculations of the tHq and tHW cross sections at $\sqrt{s} = 13$ TeV can be
 879 found in reference [49] and a summary of the results is presented in table 2.11.

880

881 2.5 The CP-mixing in tH processes

882 In addition to the sensitivity to sign of the H-t coupling, tHq and tHW processes have
 883 been proposed as a tool to investigate the possibility of a H-t coupling that does not
 884 conserve CP [43, 48, 50]. Current experimental results are consistent with SM H-V
 885 and H-t couplings; however, negative H-t coupling is not excluded completely [53].

886

887 In this thesis, the sensitivity of th processes to CP-mixing is also studied in the
 888 effective field theory framework and based in references [43, 48]; a generic particle

	\sqrt{s} TeV	$\kappa_t = 1$	$\kappa_t = -1$
$\sigma^{LO}(tHq)(\text{fb})$ [41]	8	≈ 17.4	≈ 252.7
	14	≈ 80.4	≈ 1042
$\sigma^{NLO}(tHq)(\text{fb})$ [41]	8	$18.28^{+0.42}_{-0.38}$	$233.8^{+4.6}_{-0.0}$
	14	$88.2^{+1.7}_{-0.0}$	$982.8^{+28}_{-0.0}$
$\sigma^{LO}(tHq)(\text{fb})$ [47]	14	≈ 71.8	≈ 893
$\sigma^{LO}(tHW)(\text{fb})$ [47]	14	≈ 16.0	≈ 139
$\sigma^{NLO}(tHq)(\text{fb})$ [49]	8	$18.69^{+8.62\%}_{-17.13\%}$	-
	13	$74.25^{+7.48\%}_{-15.35\%}$	$848^{+7.37\%}_{-13.70\%}$
	14	$90.10^{+7.34\%}_{-15.13\%}$	$1011^{+7.24\%}_{-13.39\%}$
$\sigma^{LO}(tHW)(\text{fb})$ [48]	13	$15.77^{+15.91\%}_{-15.76\%}$	-
$\sigma^{NLO}DR1(tHW)(\text{fb})$ [48]	13	$21.72^{+6.52\%}_{-5.24\%}$	≈ 150
$\sigma^{NLO}DR2(tHW)(\text{fb})$ [48]	13	$16.28^{+7.34\%}_{-15.13\%}$	≈ 150

Table 2.11: Predicted enhancement of the tHq and tHW cross sections at LHC for $\kappa_V = 1$ and $\kappa_t = \pm 1$ at LO and NLO; the cross section enhancement of more than a factor of 10 is due to the flippling in the sign of the H-t coupling with respect to the SM one.

889 (X_0) of spin-0 and a general CP violating interaction with the top quark, can couple
 890 to scalar and pseudoscalar fermionic densities. The H-W interaction is assumed to
 891 be SM-like. The Lagrangian modeling the H-t interaction is given by

$$\mathcal{L}_0^t = -\bar{\psi}_t (c_\alpha \kappa_{Htt} g_{Htt} + i s_\alpha \kappa_{Att} g_{Att} \gamma_5) \psi_t X_0, \quad (2.58)$$

892 where α is the CP-mixing phase, $c_\alpha \equiv \cos \alpha$ and $s_\alpha \equiv \sin \alpha$, κ_{Htt} and κ_{Att} are real
 893 dimensionless rescaling parameters⁹, $g_{Htt} = g_{Att} = m_t/v = y_t/\sqrt{2}$ and $v \sim 246$ GeV is
 894 the Higgs vacuum expectation value. In this parametrization, it is easy to recover
 895 three special cases

896 • CP-even coupling $\rightarrow \alpha = 0^\circ$

897 • CP-odd coupling $\rightarrow \alpha = 90^\circ$

898 • SM coupling $\rightarrow \alpha = 0^\circ$ and $\kappa_{Htt} = 1$

⁹ analog to κ_t and κ_V

899 The loop induced X_0 coupling to gluons can also be described in terms of the
 900 parametrization above, according to

$$\mathcal{L}_0^g = -\frac{1}{4} \left(c_\alpha \kappa_{Hgg} g_{Hgg} G_{\mu\nu}^a G^{a,\mu\nu} + s_\alpha \kappa_{Agg} g_{Agg} G_{\mu\nu}^a \tilde{G}^{a,\mu\nu} \right) X_0. \quad (2.59)$$

901 where $g_{Hgg} = -\alpha_s/3\pi v$ and $g_{Agg} = \alpha_s/2\pi v$. Under the assumption that the top quark
 902 dominates the gluon-fusion process at LHC energies, $\kappa_{Hgg} \rightarrow \kappa_{Htt}$ and $\kappa_{Agg} \rightarrow \kappa_{Att}$,
 903 so that the ratio between the gluon-gluon fusion cross section for X_0 and for the SM
 904 Higgs prediction can be written as

$$\frac{\sigma_{NLO}^{gg \rightarrow X_0}}{\sigma_{NLO,SM}^{gg \rightarrow H}} = c_\alpha^2 \kappa_{Htt}^2 + s_\alpha^2 \left(\kappa_{Att} \frac{g_{Agg}}{g_{Hgg}} \right)^2. \quad (2.60)$$

905 If the rescaling parameters are set to

$$\kappa_{Htt} = 1, \quad \kappa_{Att} = \left| \frac{g_{Hgg}}{g_{Agg}} \right| = \frac{2}{3}. \quad (2.61)$$

906 the gluon-fusion SM cross section is reproduced for every value of the CP-mixing
 907 angle α ; therefore, by imposing that condition to the Lagrangian density 2.58, the
 908 CP-mixing angle is not constrained by current data. Figure 2.16 shows the NLO cross
 909 sections for t-channel tX_0 (blue) and $t\bar{t}X_0$ (red) associated production processes as
 910 a function of the CP-mixing angle α . X_0 is a generic spin-0 particle with top quark
 911 CP-violating coupling. Rescaling factors κ_{Htt} and κ_{Att} have been set to reproduce
 912 the SM gluon-fusion cross sections.

913 It is interesting to notice that the tX_0 cross section is enhanced, by a factor of
 914 about 10, when a continuous rotation in the scalar-pseudoscalar plane is applied; this
 915 enhancement is similar to the enhancement produced when the H-t coupling is flipped
 916 in sign with respect to the SM ($y_t = -y_{t,SM}$ in the plot), as showed in section 2.4. In

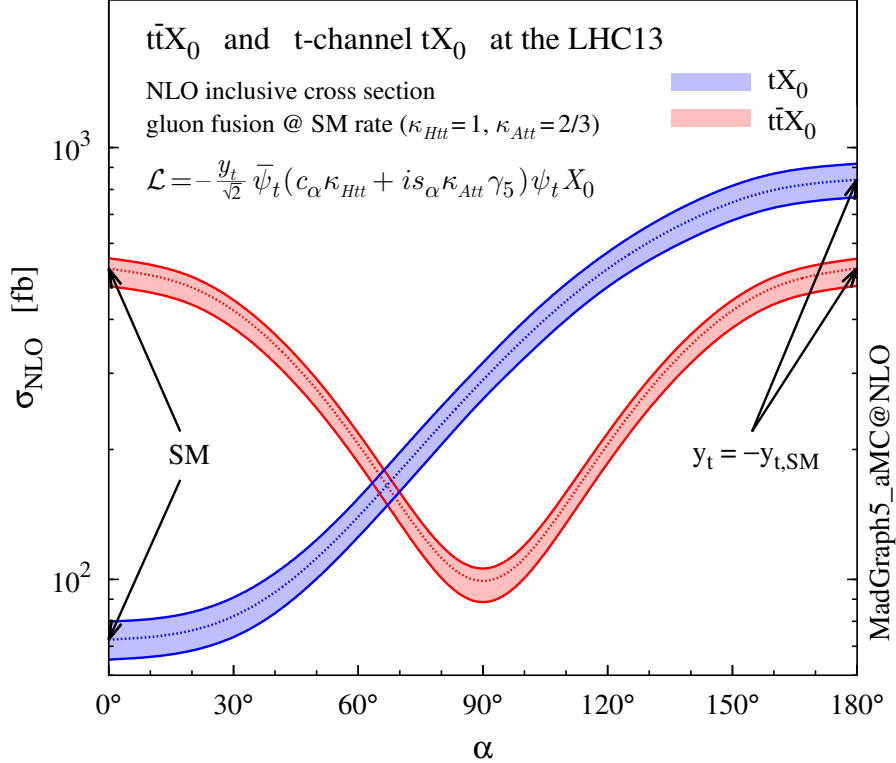


Figure 2.16: NLO cross sections for t-channel tX_0 (blue) and $t\bar{t}X_0$ (red) associated production processses as a function of the CP-mixing angle α . X_0 is a generic spin-0 particle with top quark CP-violating coupling [43].

917 contrast, the degeneracy in the $t\bar{t}X_0$ cross section is still present given that it depends
 918 quadratically on the H-t coupling, but more insteresting is to notice that $t\bar{t}X_0$ cross
 919 section is exceeded by tX_0 cross section after $\alpha \sim 60^\circ$.

920 A similar parametrization can be used to investigate the tHW process sensitivity to
 921 CP-violating H-t coupling. As said in 2.4, the interference in the W-associated chan-
 922 nel is more complicated because there are more than two contributions and also there
 923 is interference with the $t\bar{t}H$ production process.

924

925 Figure 2.17 shows the NLO cross sections for t-channel tX_0 (blue), $t\bar{t}X_0$ (red) asso-
 926 ciated production and for the combined $tWX_0 + t\bar{t}X_0 +$ interference (orange) as a

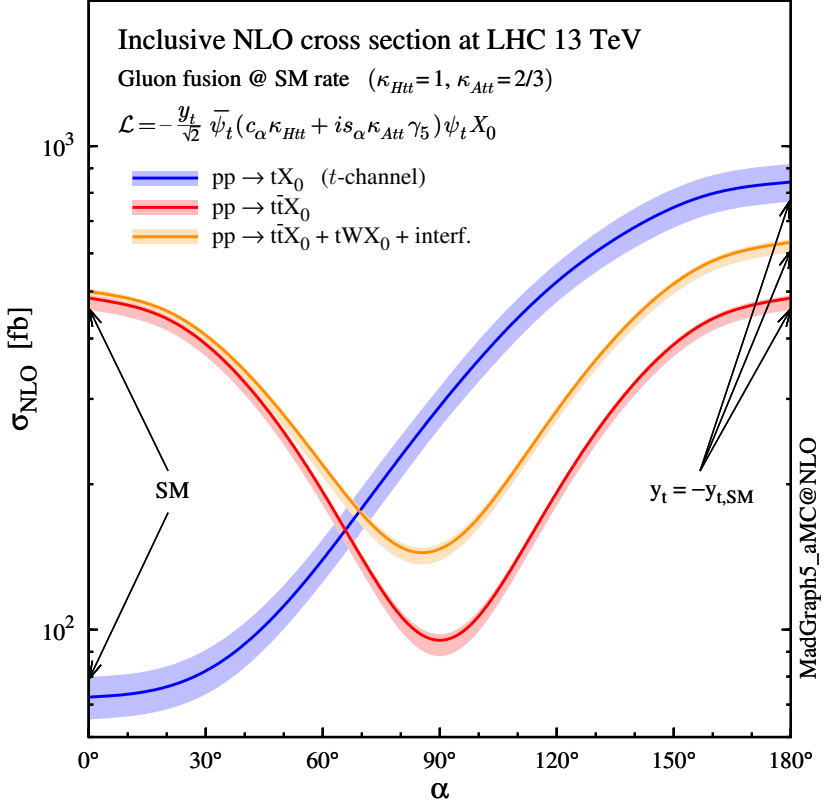


Figure 2.17: NLO cross sections for t-channel tX_0 (blue), $t\bar{t}X_0$ (red) associated production processes and combined $tWX_0 + t\bar{t}X_0$ (including interference) production as a function of the CP-mixing angle α [43].

function of the CP-mixing angle. It is clear that the effect of the interference in the combined case is the lifting of the degeneracy present in the $t\bar{t}X_0$ production. The constructive interference enhances the cross section from about 500 fb at SM ($\alpha = 0$) to about 600 fb ($\alpha = 180^\circ \rightarrow y_t = -y_{t,SM}$).

An analysis combining tHq and tHW processes will be made in this thesis taking advantage of the sensitivity improvement.

933 **2.6 Experimantal status of the anomalous**
 934 **Higg-fermion coupling.**

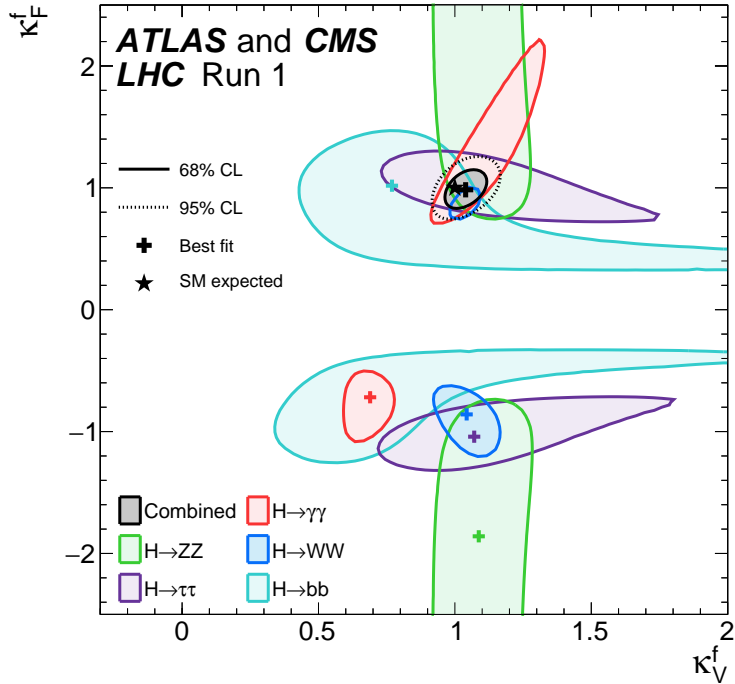


Figure 2.18: Combination of the ATLAS and CMS fits for coupling modifiers κ_t - κ_V ; also shown the individual decay channels combination and their global combination. No assumptions have been made on the sign of the coupling modifiers [53].

935 ATLAS and CMS have performed analysis of the anomalous H-f coupling by making
 936 likelihood scans for the two coupling modifiers, κ_t and κ_V , under the assumption that
 937 $\kappa_Z = \kappa_W = \kappa_V$ and $\kappa_t = \kappa_\tau = \kappa_b = \kappa_f$. Figure 2.18 shows the result of the combination
 938 of ATLAS and CMS fits; also the individual decay channels combination and the
 939 global combination results are shown.

940 While all the channels are compatible for positive values of the modifiers, for negative
 941 values of κ_t there is no compatibility. The best fit for individual channels is compatible
 942 with negative values of κ_t except for the $H \rightarrow bb$ channel which is expected to be the

943 most sensitive channel; therefore, the best fit for the global fit yields $\kappa_t \geq 0$. Thus,
944 the anomalous H-t coupling cannot be excluded completely.

₉₄₅ **Chapter 3**

₉₄₆ **The CMS experiment at the LHC**

₉₄₇ **3.1 Introduction**

₉₄₈ Located on the Swiss-French border, the European Council for Nuclear Research
₉₄₉ (CERN) is the largest scientific organization leading the particle physics research.
₉₅₀ About 13000 people in a broad range of fields including users, students, scientists,
₉₅₁ engineers, among others, contribute to the data taking and analysis, with the goal
₉₅₂ of unveiling the secrets of nature and revealing the fundamental structure of the
₉₅₃ universe. CERN is also the home of the Large Hadron Collider (LHC), the largest
₉₅₄ circular particle accelerator around the world, where protons (or heavy ions) traveling
₉₅₅ close to the speed of light, are made to collide. These collisions open a window
₉₅₆ to investigate how particles (and their constituents if they are composite) interact
₉₅₇ with each other, providing clues about the laws of nature. This chapter presents an
₉₅₈ overview of the LHC structure and operation. A detailed description of the CMS
₉₅₉ detector is offered, given that the data used in this thesis have been taken with this
₉₆₀ detector.

961 3.2 The LHC

962 With 27 km of circumference, the LHC is currently the largest and most powerful
 963 circular accelerator in the world. It is installed in the same tunnel where the Large
 964 Electron-Positron (LEP) collider was located, taking advantage of the existing infras-
 965 tructure. The LHC is also the larger accelerator in the CERN's accelerator complex
 966 and is assisted by several successive accelerating stages before the particles are in-
 967 jected into the LHC ring where they reach their maximum energy (see figure 3.1).

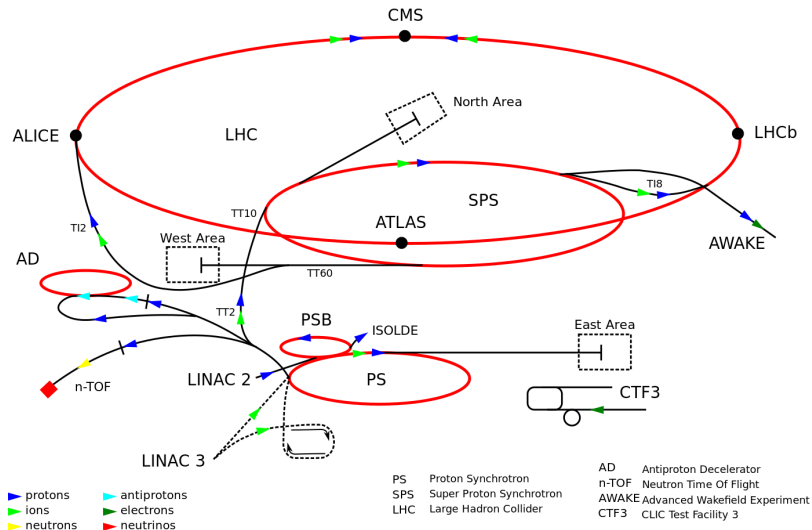


Figure 3.1: CERN accelerator complex. Blue arrows show the path followed by protons along the acceleration process [54].

968 LHC runs in three modes depending on the particles being accelerated

- 969 • Proton-Proton collisions (pp) for multiple physics experiments.
- 970 • Lead-Lead collisions ($Pb-Pb$) for heavy ion experiments.
- 971 • Proton-Lead collisions ($p-Pb$) for quark-gluon plasma experiments.

972 In this thesis only pp collisions will be considered.

973

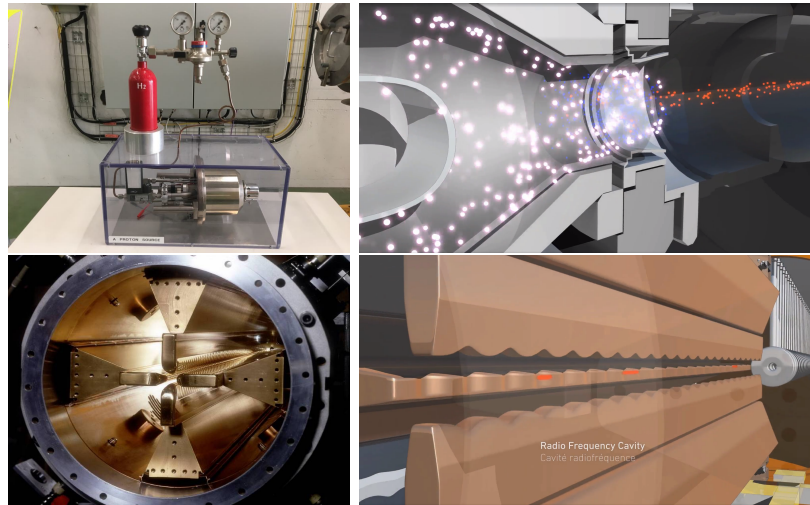


Figure 3.2: LHC protons source and the first acceleration stage. Top: the bottle contains hydrogen gas (white dots) which is injected into the metal cylinder to be broken down into electrons(blue dots) and protons(red dots); Bottom: the obtained protons are directed towards the radio frequency quadrupole which perform the first acceleration, focus the beam and create the bunches of protons. [58, 59]

974 Collection of protons starts with hydrogen atoms taken from a bottle, containing hy-
 975 drogen gas, and injecting them in a metal cylinder; hydrogen atoms are broken down
 976 into electrons and protons by an intense electric field (see figure3.2 top). The result-
 977 ing protons leave the metal cylinder towards a radio frequency quadrupole (RFQ)
 978 that focus the beam, accelerates the protons and creates the packets of protons called
 979 bunches. In the RFQ, an electric field is generated by a RF wave at a frequency that
 980 matches the resonance frequency of the cavity where the electrodes are contained.
 981 The beam of protons traveling on the RFQ axis experiences an alternating electric
 982 field gradient that generates the focusing forces.

983

984 In order to accelerate the protons, a longitudinal time-varying electric field component
 985 is added to the system; it is done by giving the electrodes a sinus-like profile as shown
 986 in figure 3.2 bottom. By matching the speed and phase of the protons with the
 987 longitudinal electric field the bunching is performed; protons synchronized with the

988 RFQ (synchronous proton) do not feel an accelerating force, but those protons in the
 989 beam that have more (or less) energy than the synchronous proton (asynchronous
 990 protons) will feel a decelerating (accelerating) force; therefore, asynchronous protons
 991 will oscillate around the synchronous ones forming bunches of protons [56]. From the
 992 RFQ protons emerge with energy 750 keV in bunches of about 1.15×10^{11} protons [57].

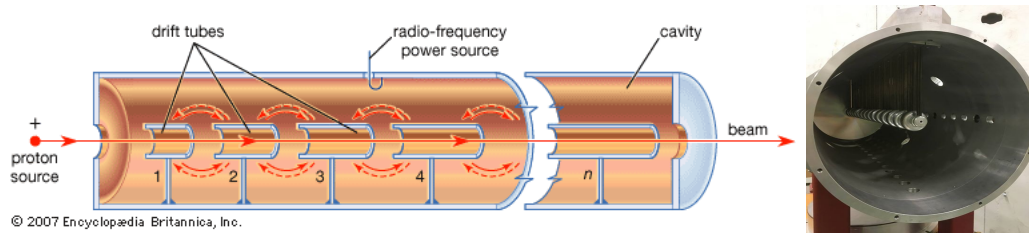


Figure 3.3: The LINAC2 accelerating system at CERN. Electric fields generated by radio frequency (RF) create acceleration and deceleration zones inside the cavity; deceleration zones are blocked by drift tubes where quadrupole magnets focus the proton beam. [60]

993 Proton bunches coming from the RFQ go to the linear accelerator 2 (LINAC2) where
 994 they are accelerated to reach 50 MeV energy. In the LINAC2 stage, acceleration
 995 is performed using electric fields generated by radio frequency which create zones
 996 of acceleration and deceleration as shown in figure 3.3. In the deceleration zones,
 997 the electric field is blocked using drift tubes where protons are free to drift while
 998 quadrupole magnets focus the beam.

999

1000 The beam coming from LINAC2 is injected into the proton synchrotron booster
 1001 (PSB) to reach 1.4 GeV in energy. The next acceleration is provided at the pro-
 1002 ton synchrotron (PS) up to 26 GeV, followed by the injection into the super proton
 1003 synchrotron (SPS) where protons are accelerated to 450 GeV. Finally, protons are
 1004 injected into the LHC where they are accelerated to the target energy of 6.5 TeV.
 1005 PSB, PS, SPS and LHC accelerate protons using the same RF acceleration technique
 1006 described before.

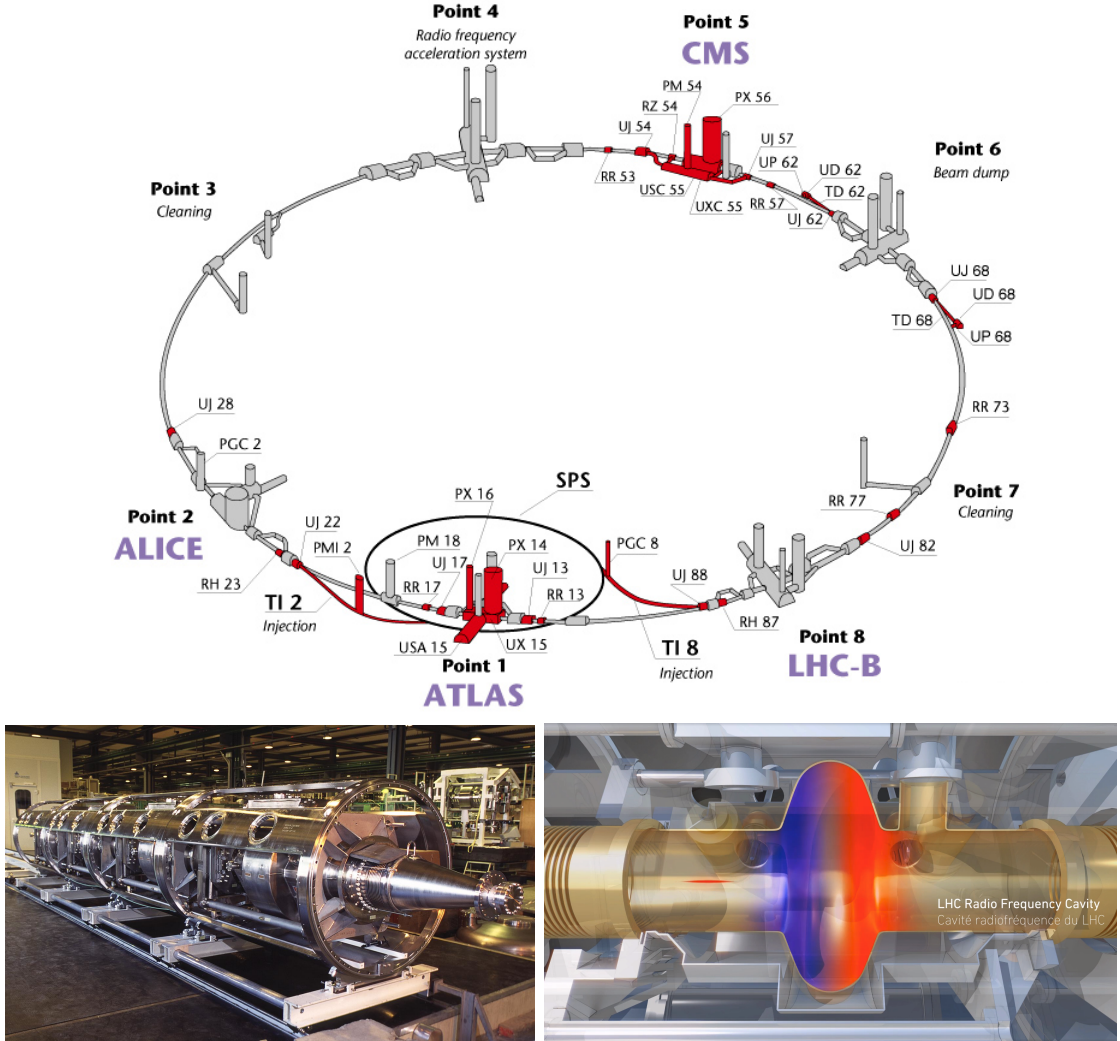


Figure 3.4: Top: LHC layout. The red zones indicate the infrastructure additions to the LEP installations, built to accommodate the ATLAS and CMS experiments which exceed the size of the former experiments located there [55]. Bottom: LHC RF cavities. A module accommodates 4 cavities that accelerate protons and preserve the bunch structure of the beam. [59, 61]

1007 LHC has a system of 16 RF cavities located in the so-called point 4, as shown in
 1008 figure 3.4 top, tuned at a frequency of 400 MHz and the protons are carefully timed,
 1009 so in addition to the acceleration effect the bunch structure of the beam is preserved.
 1010 Bottom side of figure 3.4 shows a picture of a RF module composed of 4 RF cavities
 1011 working in a superconducting state at 4.5 K; also is showed a representation of the

1012 accelerating electric field that accelerates the protons in the bunch.

1013

1014 While protons are accelerated in one section of the LHC ring, where the RF cavities
 1015 are located, in the rest of their path they have to be kept in the curved trajectory
 1016 defined by the LHC ring. Technically, LHC is not a perfect circle; RF, injection, beam
 1017 dumping, beam cleaning and sections before and after the experimental points where
 1018 protons collide are all straight sections. In total, there are 8 arcs 2.45 Km long each
 1019 and 8 straight sections 545 m long each. In order to curve the proton's trajectory in
 1020 the arc sections, superconducting dipole magnets are used.

1021

1022 Inside the LHC ring, there are two proton beams traveling in opposite directions in
 1023 two separated beam pipes; the beam pipes are kept at ultra-high vacuum ($\sim 10^{-9}$
 1024 Pa) to ensure that there are no particles that interact with the proton beams. The
 1025 superconducting dipole magnets used in LHC are made of a NbTi alloy, capable of
 1026 transporting currents of about 12000 A when cooled at a temperature below 2K using
 1027 liquid helium (see figure 3.5).

1028

1029 Protons in the arc sections of LHC feel a centripetal force exerted by the dipole
 1030 magnets which is perpendicular to the beam trajectory; The magnitude of magnetic
 1031 field needed can be found assuming that protons travel at $v \approx c$, using the standard
 1032 values for proton mass and charge and the LHC radius, as

$$F_m = \frac{mv^2}{r} = qBv \quad \rightarrow B = 8.33T \quad (3.1)$$

1033 which is about 100000 times the Earth's magnetic field. A representation of the mag-
 1034 netic field generated by the dipole magnets is shown on the bottom left side of figure

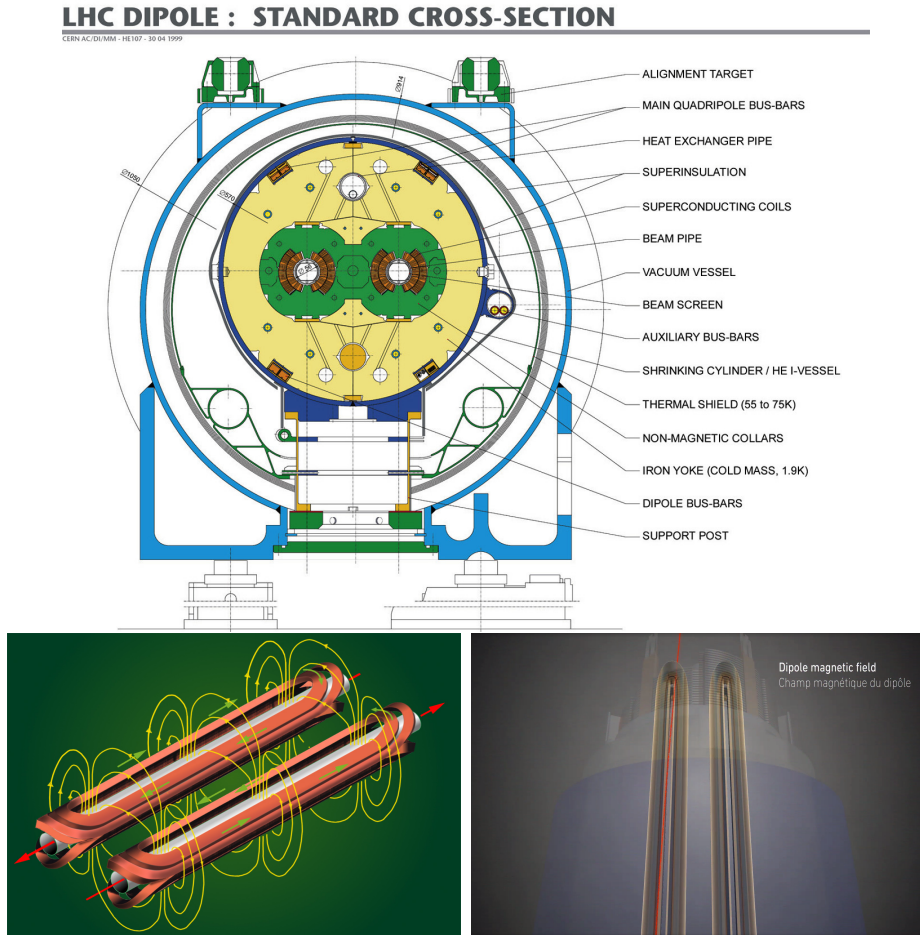


Figure 3.5: Top: LHC dipole magnet transverse view; cooling, shielding and mechanical support are indicated. Bottom left: Magnetic field generated by the dipole magnets; note that the direction of the field inside one beam pipe is opposite with respect to the other beam pipe which guarantee that both proton beams are curved in the same direction towards the center of the ring. The effect of the dipole magnetic field on the proton beam is represented on the bottom right side [59, 62, 63].

1035 3.5. The bending effect of the magnetic field on the proton beam is shown on the
 1036 bottom right side of figure 3.5. Note that the dipole magnets are not curved; the arc
 1037 section of the LHC ring is composed of straight dipole magnets of about 15 m. In
 1038 total there are 1232 dipole magnets along the LHC ring.

1039

1040 In addition to bending the beam trajectory, the beam has to be focused so it stays

1041 inside the beam pipe. The focusing is performed by quadrupole magnets installed in
 1042 a different straight section; in total 858 quadrupole magnets are installed along the
 1043 LHC ring. Other effects like electromagnetic interaction among bunches, interaction
 1044 with electron clouds from the beam pipe, the gravitational force on the protons, dif-
 1045 ferences in energy among protons in the same bunch, among others, are corrected
 1046 using sextupole and other magnetic multipoles.

1047

1048 The two proton beams inside the LHC ring are made of bunches with a cylindrical
 1049 shape of about 7.5 cm long and about 1 mm in diameter; when bunches are close
 1050 to the collision point (CP), the beam is focused up to a diameter of about 16 μm in
 1051 order to maximize the number of collisions per unit area and per second, known as
 1052 luminosity (L). Luminosity can be calculated using

$$L = fn \frac{N_1 N_2}{4\pi\sigma_x\sigma_y} \quad (3.2)$$

1053 where f is the revolution frequency, n is the number of bunches per beam, N_1 and
 1054 N_2 are the numbers of protons per bunch (1.5×10^{11}), σ_x and σ_y are the gaussian
 1055 transverse sizes of the bunches. The expected luminosity is about

$$f = \frac{v}{2\pi r_{LHC}} \approx \frac{3 \times 10^8 \text{ m/s}}{27 \text{ km}} \approx 11.1 \text{ kHz},$$

$$n = 2808$$

$$N_1 = N_2 = 1.5 \times 10^{11}$$

$$\sigma_x = \sigma_y = 16 \mu\text{m}$$

1056

$$L = 1.28 \times 10^{34} \text{ cm}^{-2} \text{ s}^{-1} = 1.28 \times 10^{-5} \text{ fb}^{-1} \text{ s}^{-1} \quad (3.3)$$

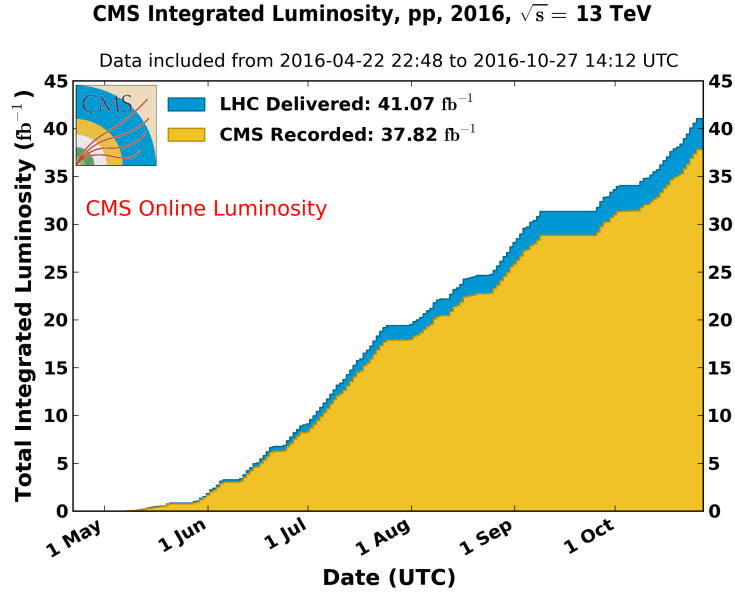


Figure 3.6: Integrated luminosity delivered by LHC and recorded by CMS during 2016. The difference between the delivered and the recorded luminosity is due to fails and issues occurred during the data taking in the CMS experiment [64].

1057 Luminosity is a fundamental aspect of LHC given that the bigger luminosity the
 1058 bigger number of collisions, which means that for processes with a very small cross
 1059 section the number of expected occurrences is increased and so the chances of being
 1060 detected. The integrated luminosity, i.e., the total luminosity, collected by the CMS
 1061 experiment during 2016 is shown in figure 3.6; the data analyzed in this thesis corre-
 1062 sponds to an integrated luminosity of 35.9 fb^{-1} at a center of mass-energy $\sqrt{s} = 13$
 1063 TeV.

1064

1065 A way to increase L is increasing the number of bunches in the beam. Currently, the
 1066 separation between two consecutive bunches in the beam is 7.5 m which corresponds
 1067 to a time separation of 25 ns. In the full LHC ring the allowed number of bunches is
 1068 $n = 27\text{km}/7.5\text{m} = 3600$; however, there are some gaps in the bunch pattern intended
 1069 for preparing the dumping and injection of the beam, thus, the proton beams are

1070 composed of 2808 bunches.

1071

1072 Once the proton beams reach the desired energy, they are brought to cross each other
 1073 producing proton-proton collisions. The bunch crossing happens in precise places
 1074 where the four LHC experiments are located, as seen in the top of figure 3.7. In 2008,
 1075 the first set of collisions involved protons with $\sqrt{s} = 7$ TeV; the energy was increased
 1076 to 8 TeV in 2012 and to 13 TeV in 2015.

1077

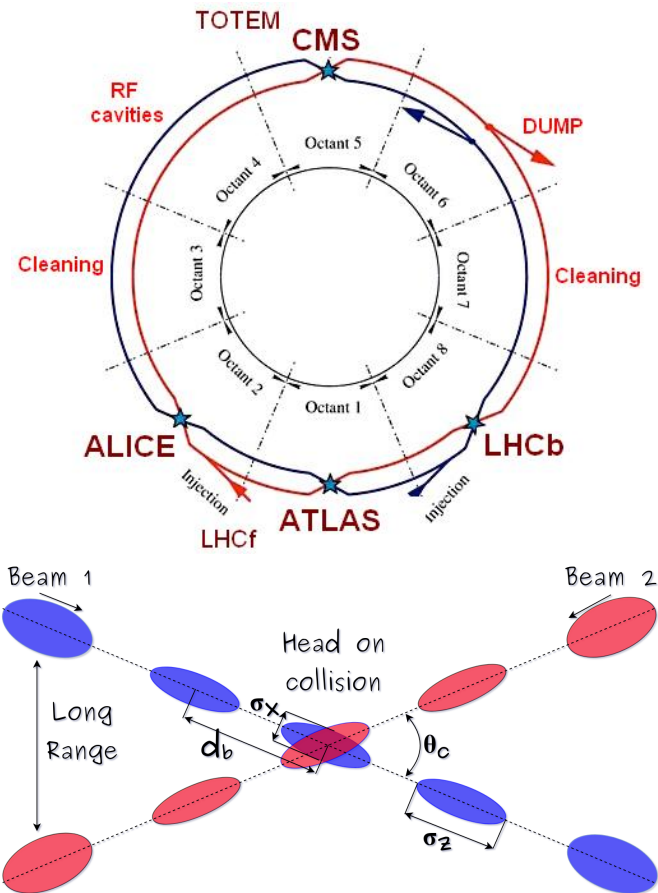


Figure 3.7: Top: LHC interaction points. Bunch crossing occurs where the LHC experiments are located [65]. Sections indicated as cleaning are dedicated to collimate the beam in order to protect the LHC ring from collisions with protons in very spreaded bunches. Bottom: bunch crossing scheme. Since the bunch crossing is not perfectly head-on, the luminosity is reduced in a factor of 17%; adapted from reference [77].

1078 CMS and ATLAS experiments, which are multi-purpose experiments, are enabled
 1079 to explore physics in any of the collision modes. LHCb experiment is optimized
 1080 to explore bottom quark physics, while ALICE is optimized for heavy ion collisions
 1081 searches; TOTEM and LHCf are dedicated to forward physics studies; MoEDAL (not
 1082 indicated in the figure) is intended for monopoles or massive pseudo stable particles
 1083 searches.

1084

1085 At the CP there are two interesting details that need to be addressed. The first one
 1086 is that the bunch crossing does not occur head-on but at a small crossing angle “ θ_c ”
 1087 (280 μ rad in CMS and ATLAS) as shown in the bottom side of figure 3.7, affecting
 1088 the overlapping between bunches; the consequence is a reduction of about 17% in
 1089 the luminosity (represented by a factor not included in eqn: 3.2). The second one
 1090 is the occurrence of multiple pp collisions in the same bunch crossing; this effect is
 1091 called pile-up (PU). A fairly simple estimation of the PU follows from estimating the
 1092 probability of collision between two protons, one from each of the bunches in course
 1093 of collision; it depends roughly on the ratio of proton size and the cross section of the
 1094 bunch in the interaction point, i.e.,

$$P(pp\text{-}collision) \sim \frac{d_{proton}^2}{\sigma_x \sigma_y} = \frac{(1\text{fm})^2}{(16\mu\text{m})^2} \sim 4 \times 10^{-21} \quad (3.4)$$

1095 however, there are $N = 1.15 \times 10^{11}$ protons in a bunch, thus the estimated number of
 1096 collisions in a bunch crossing is

$$PU = N^2 * P(pp\text{-}collision) \sim 50 \text{ } pp\text{-}collision \text{ per bunch crossing}, \quad (3.5)$$

1097 about 20 of those pp collisions are inelastic. Each collision generates a vertex, but
 1098 only the most energetic is considered as a primary vertex; the rest are considered as

1099 PU vertices. A multiple pp collision event in a bunch crossing at CMS is showed in
 1100 figure3.8. Unstable particles outgoing from the primary vertex will eventually decay;
 1101 this decay vertex is known as a secondary vertex.

1102

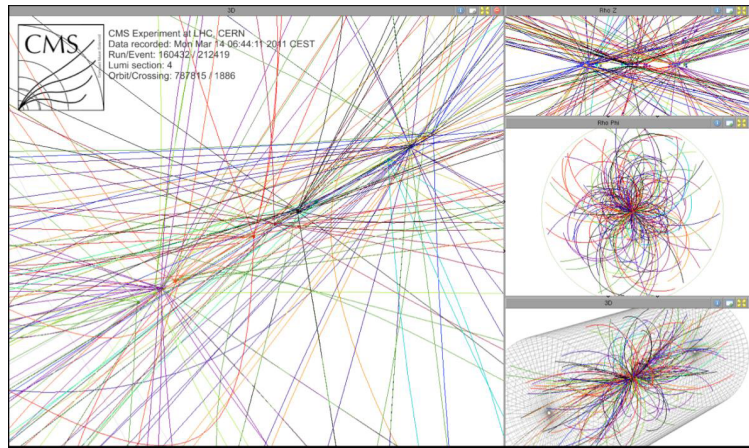


Figure 3.8: Multiple pp collision bunch crossing at CMS. Only the most energetic vertex is considered and the rest are catalogued as PU vertices [66].

1103 Next section presents a description of the CMS detector which it is the detector used
 1104 to collect the data used in this thesis.

1105 3.3 The CMS experiment

1106 CMS is a general-purpose detector designed to conduct research in a wide range
 1107 of physics from the standard model to new physics like extra dimensions and dark
 1108 matter. Located at the point 5 in the LHC layout as shown in figure 3.4, CMS is
 1109 composed of several detection systems distributed in a cylindrical structure; in total,
 1110 CMS weights about 12500 tons in a very compact 21.6 m long and 14.6 m diameter
 1111 cylinder. It was built in 15 separate sections at the ground level and lowered to the
 1112 cavern individually to be assembled. A complete and detailed description of the CMS

1113 detector and its components is given in reference [67] on which this section is based on.

1114

1115 Figure 3.9 shows the layout of the CMS detector. The design is driven by the require-
 1116 ments on the identification, momentum resolution and unambiguous charge determi-
 1117 nation of the muons; therefore, a large bending power is provided by the solenoid
 1118 magnet made of superconducting cable capable to generate a 3.8 T magnetic field.
 1119 The detection system is composed of (from the innermost to the outermost)

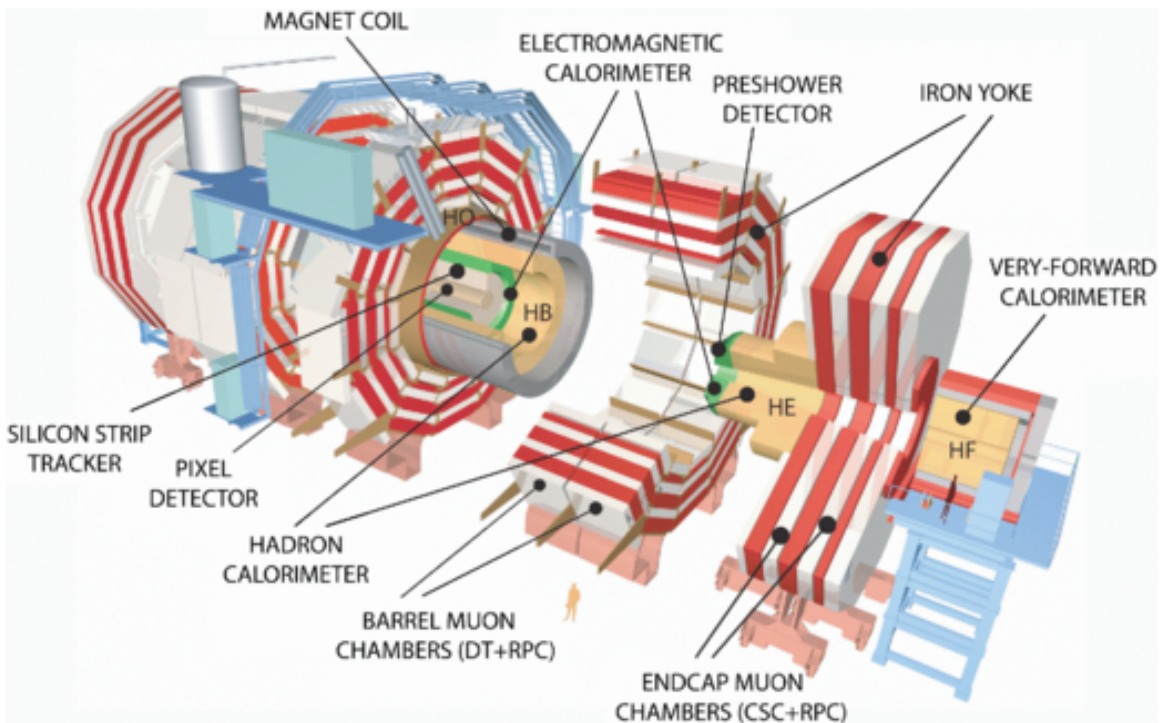


Figure 3.9: Layout of the CMS detector. The several subdetectors are indicated. The central region of the detector is referred as the Barrel section while the endcaps are referred as the forward sections. [68].

1120 • Pixel detector.

1121 • Silicon strip tracker.

1122 • Preshower detector.

1123 • Electromagnetic calorimeter.

1124 • Hadronic calorimeter.

1125 • Muon chambers (Barrel and endcap)

1126 The central region of the detector is commonly referred as the barrel section while the
 1127 endcaps are referred as the forward sections of the detector; thus, each subdetector
 1128 is composed of a barrel section and a forward section.

1129 3.3.1 Coordinate system

1130 The coordinate system used by CMS is centered in the geometrical center of the
 1131 detector which is the same as the CP as shown in figure 3.10. The z -axis is parallel
 1132 to the beam direction, while the Y -axis pointing vertically upward, and the X -axis
 1133 pointing radially inward toward the center of the LHC.

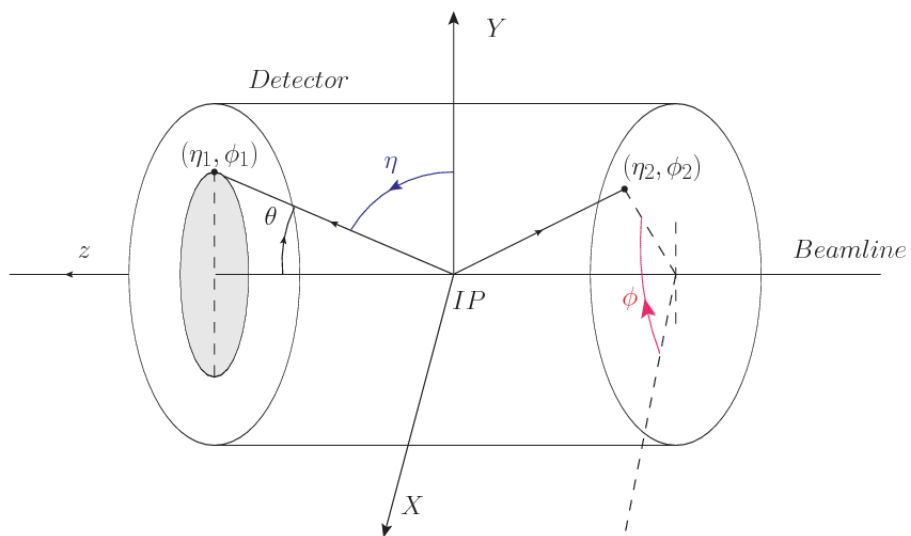


Figure 3.10: CMS detector coordinate system.

1134 In addition to the common cartesian and cylindrical coordinate systems, two coordi-
 1135 nates are of particular utility in particle physics: rapidity(y) and pseudorapidity(η),

1136 defined in connection to the polar angle θ , energy and longitudinal momentum com-
 1137 ponent (momentum along the z -axis) according to

$$y = \frac{1}{2} \ln \frac{E + p_z}{E - p_z} \quad \eta = -\ln \left(\tan \frac{\theta}{2} \right) \quad (3.6)$$

1138 Rapidity is related to the angle between the XY -plane and the direction in which the
 1139 products of a collision are emitted; it has the nice property that the difference between
 1140 the rapidities of two particles is invariant with respect to Lorentz boosts along the z -
 1141 axis. Thus, data analysis becomes more simple when based on rapidity; however, it is
 1142 not simple to measure the rapidity of highly relativistic particles, as those produced
 1143 after pp collisions. Under the highly relativistic motion approximation, y can be
 1144 rewritten in terms of the polar angle, concluding that rapidity is approximately equal
 1145 to the pseudorapidity defined above, i.e., $y \approx \eta$. Note that η is easier to measure than y
 1146 given the direct relationship between the former and the polar angle. Angular distance
 1147 between two objects in the detector (ΔR) is defined in terms of their coordinates
 1148 $(\eta_1, \phi_1), (\eta_2, \phi_2)$ as

$$\Delta R = \sqrt{(\Delta\eta)^2 - (\Delta\phi)^2} \quad (3.7)$$

1149 3.3.2 Pixels detector

1150 The CMS tracking system is designed to provide a precise measurement of the tra-
 1151 jectory (*track*) followed by the charged particles created after the pp collisions; also,
 1152 the precise reconstruction of the primary and secondary origins (*vertices*) is expected
 1153 in an environment where, each 25 ns, the bunch crossing produce about 20 inelastic
 1154 collisions and about 1000 particles. An increment in the luminosity is ongoing which
 1155 implies that the PU will increase accordingly.

1157 The pixel detector was replaced during the 2016-2017 extended year-end technical
1158 stop, due to the increasingly challenging operating conditions like the higher particle
1159 flow and more radiation harsh environment, among others. The new one is respond-
1160 ing as expected, reinforcing its crucial role in the successful way to fulfill the new
1161 LHC physics objectives after the discovery of the Higgs boson. The last chapter of
1162 this thesis is dedicated to describe my contribution to the “Forward Pixel Phase 1
1163 upgrade”.

1164

1165 The current pixel detector is composed of 1856 silicon pixel detector modules orga-
1166 nized in four-barrel layers in the central region and three disks in the forward region;
1167 it is designed to record efficiently and with high precision, up to $10\mu\text{m}$ in the XY -
1168 plane and $20\mu\text{m}$ in the z -direction, the first four space-points (*hits*) near to the CP
1169 region (see figure 3.11 left side) in the range $|\eta| \leq 2.5$. The first barrel layer is located
1170 at a radius of 30 mm from the beamline, while the fourth layer is located at a radius
1171 of 160 mm closer to the strip tracker inner barrel layer (see section 3.3.3) in order to
1172 reduce the rate of fake tracks. The high granularity of the detector is represented in
1173 its about 123 Mpixels, each of size $100 \times 150\mu\text{m}^2$, which is almost twice the channels
1174 of the old detector. The transverse momentum resolution of tracks can be measured
1175 with a resolution of 1-2% for muons of $p_T = 100$ GeV.

1176

1177 Some of the improvements with respect to the previous pixel detector include a higher
1178 average tracking efficiency and lower average fake rate as well as higher track impact
1179 parameter resolution which is fundamental in order to increase the efficiency in the
1180 identification of jets originating from b quarks (b-tagging). A significant source of
1181 improvement comes from the overall reduction in the material budget of the detector
1182 which results in fewer photon conversions and less multiple scattering from charged

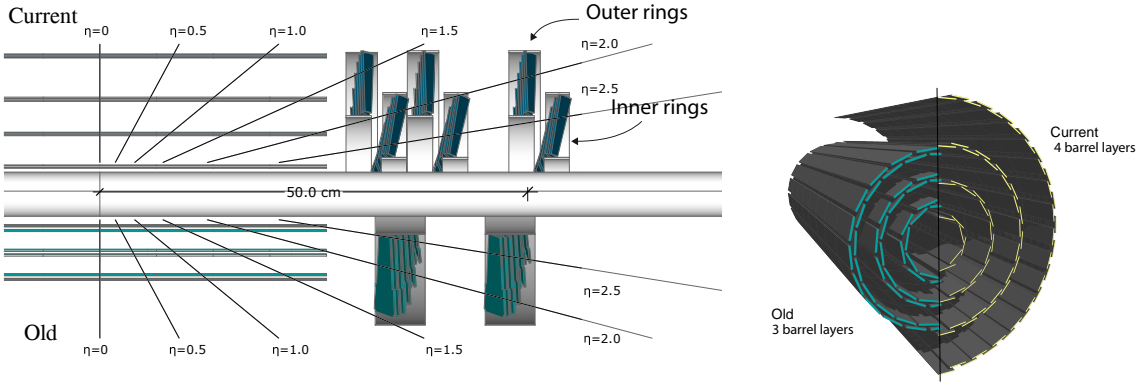


Figure 3.11: CMS pixel detector schematic view. Left: layout comparing the layers and disks in the old and current pixel detectors. Right: Transverse-oblique view comparing the pixel barrel layers in the two [70].

1183 particles.

1184 3.3.3 Silicon strip tracker

1185 The silicon strip tracker (SST) is the second stage in the CMS tracking system. The
 1186 top side of figure 3.12 shows a schematic of the SST. The inner tracker region is com-
 1187 posed of the tracker inner barrel (TIB) and the tracker inner disks (TID) covering the
 1188 region $r < 55$ cm and $|z| < 118$ cm. The TIB is composed of 4 layers while the TID
 1189 is composed of 3 disks at each end. The silicon sensors in the inner tracker are 320
 1190 μm thick, providing a resolution of about 13-38 μm in the $r\phi$ position measurement.
 1191

1192 The modules indicated in blue in the schematic view of figure 3.12 are two modules
 1193 mounted back-to-back and rotated in the plane of the module by a “stereo” angle of
 1194 100 mrad; the hits from these two modules, known as “stereo hits”, are combined to
 1195 provide a measurement of the second coordinate (z in the barrel and r on the disks)
 1196 allowing the reconstruction of hit positions in 3-D.

1197

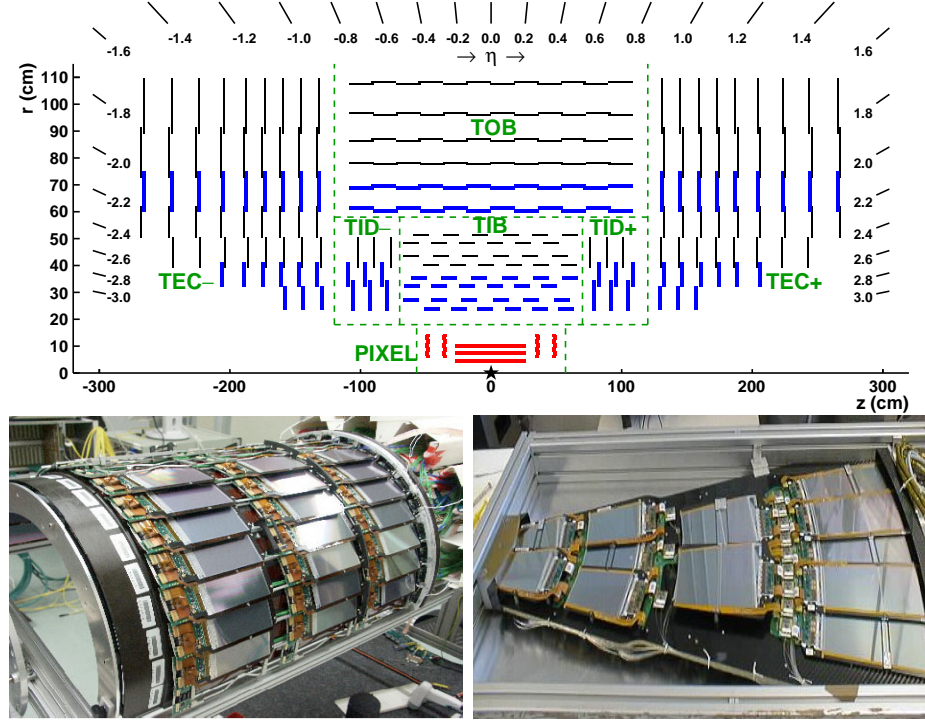


Figure 3.12: Top: CMS Silicon Strip Tracker (SST) schematic view. The SST is composed of the tracker inner barrel (TIB), the tracker inner disks (TID), the tracker outer barrel (TOB) and the tracker endcaps (TEC). Each part is made of silicon strip modules; the modules in blue represent two modules mounted back-to-back and rotated in the plane of the module by a stereo angle of 120 mrad in order to provide a 3-D reconstruction of the hit positions. Bottom: pictures of the TIB (left) and TEC (right) modules [71–73].

1198 The outer tracker region is composed of the tracker outer barrel (TOB) and the
 1199 tracker endcaps (TEC). The six layers of the TOB offer coverage in the region $r > 55$
 1200 cm and $|z| < 118$ cm, while the 9 disks of the TEC cover the region $124 < |z| < 282$
 1201 cm. The resolution offered by the outer tracker is about $13\text{--}38 \mu\text{m}$ in the $r\phi$ position
 1202 measurement. The inner four TEC disks use silicon sensors $320 \mu\text{m}$ thick; those in
 1203 the TOB and the outer three TEC disks use silicon sensors of $500 \mu\text{m}$ thickness. The
 1204 silicon strips run parallel to the z -axis and the distance between strips varies from 80
 1205 μm in the inner TIB layers to $183 \mu\text{m}$ in the inner TOB layers; in the endcaps the
 1206 wedge-shaped sensors with radial strips, whose pitch range between $81 \mu\text{m}$ at small
 1207 radii and $205 \mu\text{m}$ at large radii.

1208

1209 The whole SST has 15148 silicon modules, 9.3 million silicon strips and cover a total
 1210 active area of about 198 m^2 .

1211 **3.3.4 Electromagnetic calorimeter**

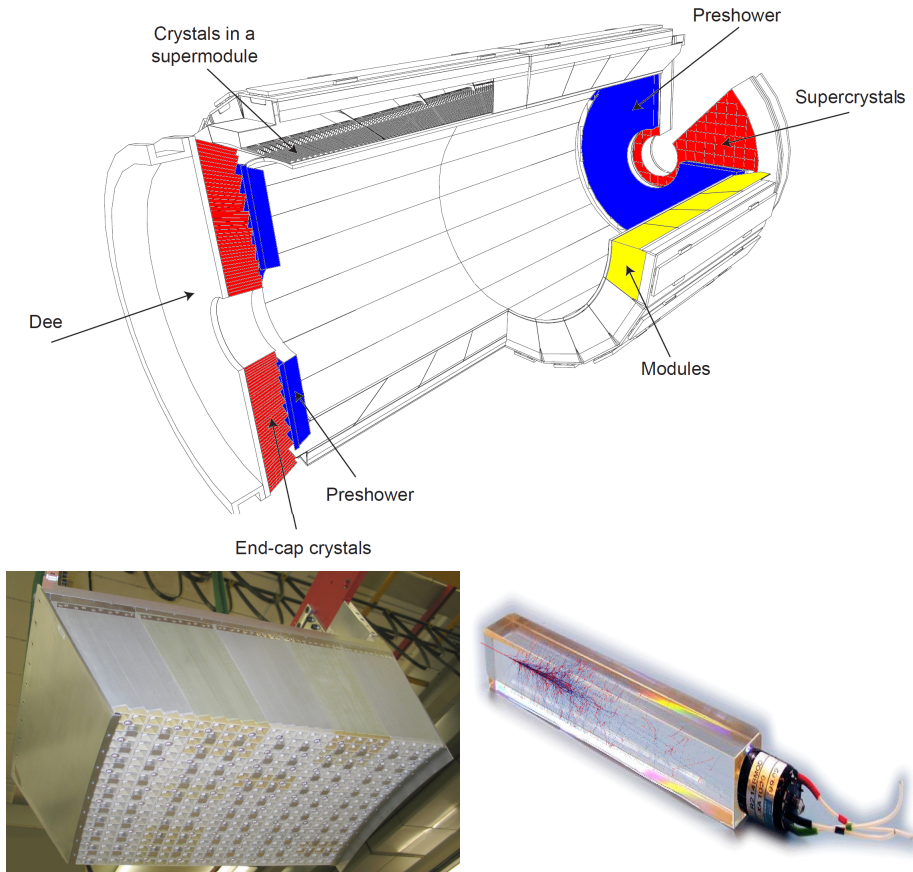


Figure 3.13: Top: CMS ECAL schematic view. Bottom: Module equipped with the crystals (left); ECAL crystal(right).

1212 The CMS electromagnetic calorimeter (ECAL) is designed to measure the energy of
 1213 electrons and photons. It is composed of 75848 lead tungstate crystals which have a
 1214 short radiation length (0.89 cm) and fast response, since 80% of the light is emitted
 1215 within 25 ns; however, they are combined with Avalanche photodiodes (APDs) as

1216 photodetectors given that crystals themselves have a low light yield ($30\gamma/\text{MeV}$). A
 1217 schematic view of the ECAL is shown in figure 3.13.

1218

1219 Energy is measured when electrons and photons are absorbed by the crystals which
 1220 generates an electromagnetic “shower”, as seen in bottom right picture of the fig-
 1221 ure3.13; the shower is seen as a *cluster* of energy which depending on the amount
 1222 of energy deposited can involve several crystals. The ECAL barrel (EB) covers the
 1223 region $|\eta| < 1.479$, using crystals of depth of 23 cm and $2.2 \times 2.2 \text{ cm}^2$ transverse
 1224 section; the ECAL endcap (EE) covers the region $1.479 < |\eta| < 3.0$ using crystals
 1225 of depth 22 cm and transverse section of $2.86 \times 2.86 \text{ cm}^2$; the photodetectors used
 1226 are vacuum phototriodes (VPTs). Each EE is divided in two structures called “Dees”.

1227

1228 In front of the EE, it is installed the preshower detector (ES) which covers the region
 1229 $1.653 < |\eta| < 2.6$. The ES provides a precise measurement of the position of electro-
 1230 magnetic showers, which allows to distinguish electrons and photons signals from π^0
 1231 decay signals. The ES is composed of a layer of lead absorber followed by a layer of
 1232 plastic scintillators

1233 3.3.5 Hadronic calorimeter

1234 Hadrons are not absorbed by the ECAL but by the hadron calorimeter (HCAL),
 1235 which is made of a combination of alternating brass absorber layers and silicon photo-
 1236 multiplier(SiPM) layers; therefore, particles passing through the scintillator material
 1237 produce showers, as in the ECAL, as a result of the inelastic scattering of the hadrons
 1238 with the detector material. Since the particles are not absorbed in the scintillator,
 1239 their energy is sampled; therefore the total energy is not measured but estimated from

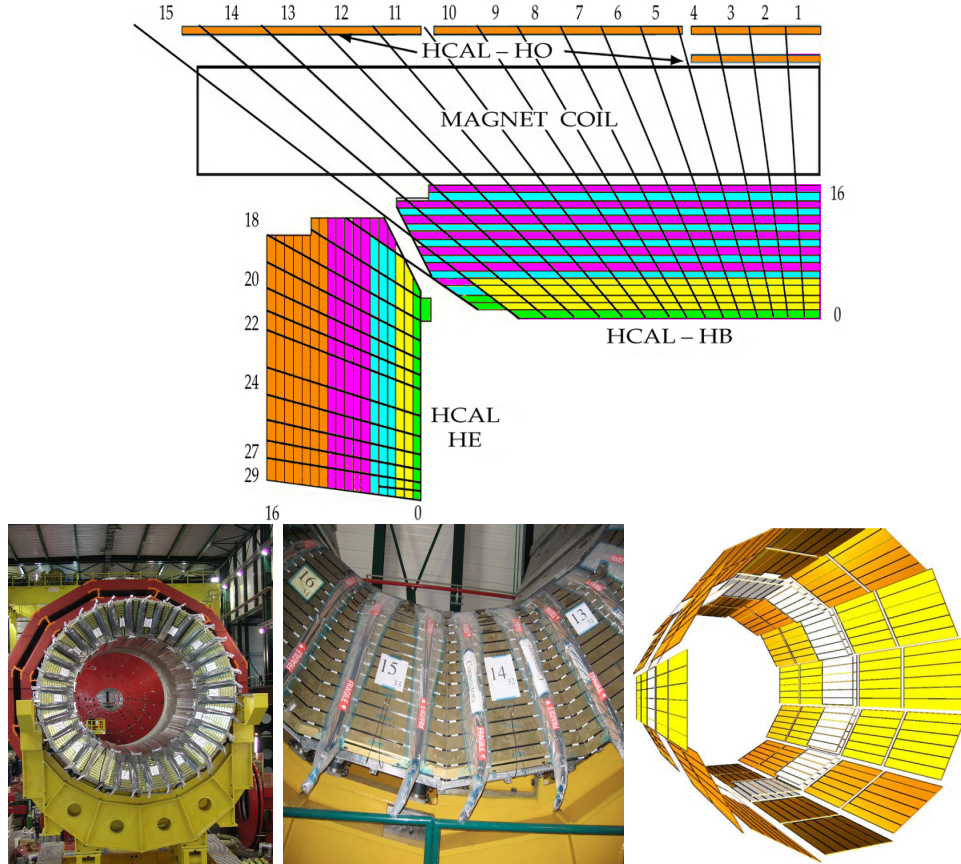


Figure 3.14: Top: CMS HCAL schematic view, the colors indicate the layers that are grouped into the same readout channels. Bottom: picture of a section of the HB; the absorber material is the golden region and scintillators are placed in between the absorber material (left and center). Schematic view of the HO (right). [74,75]

1240 the energy clusters, which reduce the resolution of the detector. Brass was chosen
 1241 as the absorber material due to its short interaction length ($\lambda_I = 16.42\text{cm}$) and its
 1242 non-magnetivity. Figure 3.14 shows a schematic view of the CMS HCAL.

1243

1244 The HCAL is divided into four sections; the Hadron Barrel (HB), the Hadron Outer
 1245 (HO), the Hadron Endcap (HE) and the Hadron Forward (HF) sections. The HB
 1246 covers the region $0 < |\eta| < 1.4$, while the HE covers the region $1.3 < |\eta| < 3.0$. The HF,
 1247 made of quartz fiber scintillator and steel as absorption material, covers the forward

region $3.0 < |\eta| < 5.2$. Both the HB and HF are located inside the solenoid. The HO is placed outside the magnet as an additional layer of scintillators with the purpose of measure the energy tails of particles passing through the HB and the magnet (see figure 3.14 top and bottom right). The upgrades made to the HCAL during the technical stop 2016-2017 consisted in the replacement of the photo transducer, in order to improve the efficiency.

3.3.6 Superconducting solenoid magnet

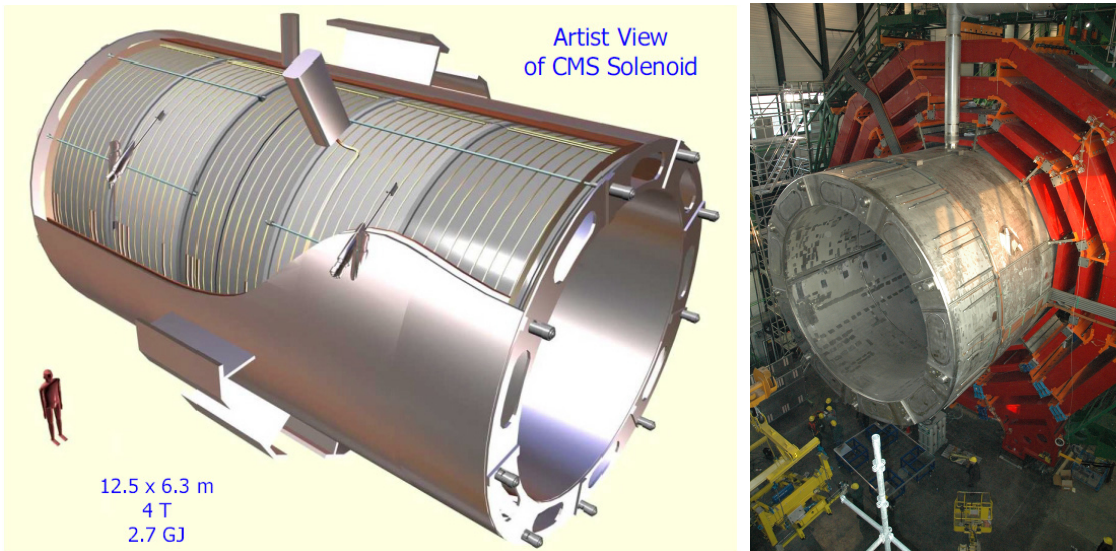


Figure 3.15: Artistic representation of the CMS solenoid magnet(left). The magnet is supported on an iron yoke (right) which also serves as the house of the muon detector and as mechanical support for the whole CMS detector [69].

The superconducting magnet installed in the CMS detector is designed to provide an intense and highly uniform magnetic field in the central part of the detector. In fact, the tracking system takes advantage of the bending power of the magnetic field to measure with precision the momentum of the particles that traverse it; the unambiguous determination of the sign for high momentum muons was a driven principle during the design of the magnet. The magnet has a diameter of 6.3 m, a length of 12.5

1261 m and a cold mass of 220 t; the generated magnetic field reaches a strength of 3.8T.
 1262 Since it is made of Ni-Tb superconducting cable it has to operate at a temperature
 1263 of 4.7 K by using a helium cryogenic system; the current circulating in the cables
 1264 reaches 18800 A under normal running conditions. The left side of figure 3.15 shows
 1265 an artistic view of the CMS magnet, while the right side shows a transverse view of
 1266 the cold mass where the winding structure is visible.

1267

1268 The yoke (see figure 3.15), composed of 5 barrel wheels and 6 endcap disks made
 1269 of iron, serves not only as the media for magnetic flux return but also provides the
 1270 house for the muon detector system and structural stability to the full detector.

1271 3.3.7 Muon system

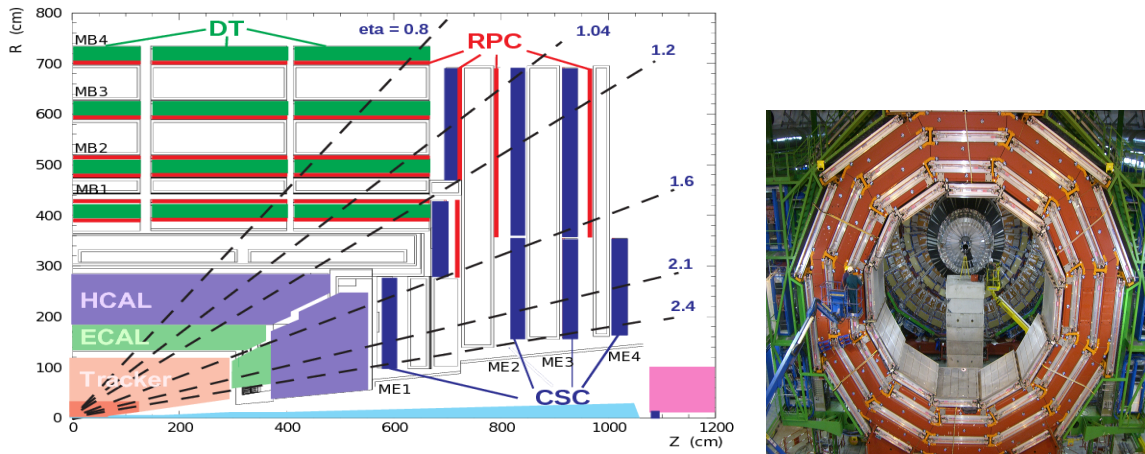


Figure 3.16: Left: CMS muon system schematic view; Right: one of the yoke rings with the muon DTs and RPCs installed; in the back it is possible to see the muon endcap [76].

1272 Muons are the only charged particles able to pass through all the CMS detector due
 1273 to their low ionization energy loss; thus, muons can be separated easily from the
 1274 high amount of particles produced in a pp collision. Also, muons are expected to be
 1275 produced in the decay of several new particles; therefore, a good detection of muons

1276 was on the leading principles when designing the CMS detector.

1277

1278 The CMS muon detection system (muon spectrometer) is embedded in the return
1279 yoke as seen in figure 3.16. It is composed of three different detector types, the drift
1280 tube chambers (DT), Cathode strip chambers (CSC), and resistive plate chambers
1281 (RPC); DT are located in the central region $\eta < 1.2$ arranged in four layers of drift
1282 chambers filled with an Ar/CO₂ gas mixture.

1283

1284 The muon endcaps are made of CSCs covering the region $\eta < 2.4$ and filled with a
1285 mixture of Ar/CO₂/CF₄. The reason behind using a different detector type lies on
1286 the different conditions in the forward region like the higher muon rate and higher
1287 residual magnetic field compared to the central region.

1288

1289 The third type of detector used in the muon system is a set of four disks of RPCs
1290 working in avalanche mode. The RPCs provide good spatial and time resolutions.
1291 The track of $high - p_T$ muon candidates is built combining information from the
1292 tracking system and the signal from up to six RPCs and four DT chambers.

1293 The muon tracks are reconstructed from the hits in the several layers of the muon
1294 system.

1295 3.3.8 CMS trigger system

1296 Under normal conditions, CMS expects pp collisions every 25 ns, i.e., an interaction
1297 rate of 40 MHz for which it is not possible to store the recorded data in full. In order
1298 to handle this high event rate data, an online event selection, known as triggering, is
1299 performed; triggering reduce the event rate to 100 Hz for storage and further offline

1300 analysis.

1301

1302 The trigger system starts with a reduction of the event rate to 100 kHz in the so-called
 1303 “level 1 trigger (L1)”. L1 is based on dedicated programmable hardware like Field
 1304 Programmable Gate Arrays (FPGAs) and Application Specific Integrated Circuits
 1305 (ASICs), partly located in the detector itself; another portion is located in the CMS
 1306 under-ground cavern. Hit patterns information from the muon chambers and the en-
 1307 ergy deposits in the calorimeter are used to decide if an event is accepted or rejected,
 1308 according to selection requirements previously defined, which reflect the interesting
 1309 physics processes. Figure 3.17 shows the L1 trigger architecture.

1310

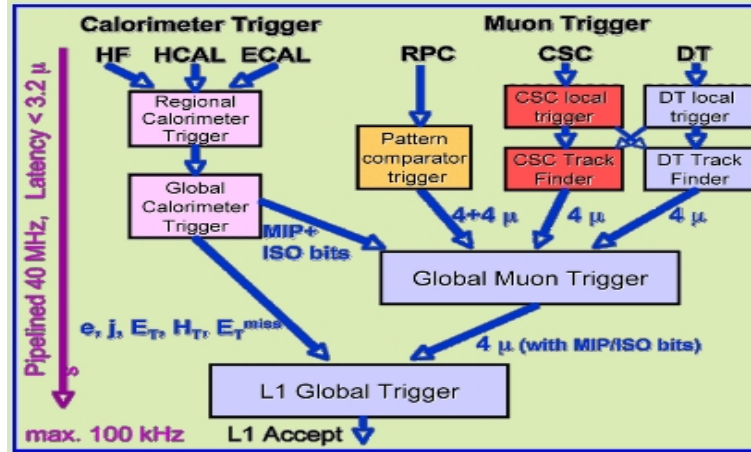


Figure 3.17: CMS Level-1 trigger architecture [77].

1311 The second stage in the trigger system is called “high-level trigger (HLT)”; events
 1312 accepted by L1 are passed to HLT in order to make an initial reconstruction of them.
 1313 HLT is software based and runs on a dedicated server farm, using selection algo-
 1314 rithms and high-level object definitions; the event rate at HLT is reduced to 100 Hz.
 1315 The first HLT stage takes information from the muon detectors and the calorimeters
 1316 to make the initial object reconstruction; in the next HLT stage, information from

1317 the pixel and strip detectors is used to do first fast-tracking and then full tracking
1318 online. This initial object reconstruction is used in further steps of the trigger system.

1319

1320 Events and preliminary reconstructed physics objects from HLT are sent to be fully
1321 reconstructed at the CERN computing center. Again, the pixel detector information
1322 provides high-quality seeds for the track reconstruction algorithm offline, primary ver-
1323 tex reconstruction, electron and photon identification, muon reconstruction, τ iden-
1324 tification, and b-tagging. After full reconstruction, data sets are made available for
1325 offline analyses.

1326

1327 During the 2016-2017 technical stop, the L1 system was updated in order to improve
1328 the physics object identification by improving the algorithms and accounting for the
1329 increasing pile-up scenario.

1330 **3.3.9 CMS computing**

1331 After the data, coming from the experiment, are processed at several levels, they have
1332 to be stored and made available for further analysis; in order to cope all the tasks
1333 implied in the offline data processing, like transfer, simulation, reconstruction and
1334 reprocessing, among others, a big computing power is required. The CMS computing
1335 system is based on the distributed architecture concept, where users of the system
1336 and physical computer centers are distributed worldwide and interconnected by high-
1337 speed networks.

1338 The worldwide LHC computing grid (WLCG) is the mechanism used to provide that
1339 distributed environment. WLCG is a tiered structure connecting computing centers
1340 around the world, which provides the necessary storage and computing facilities. The

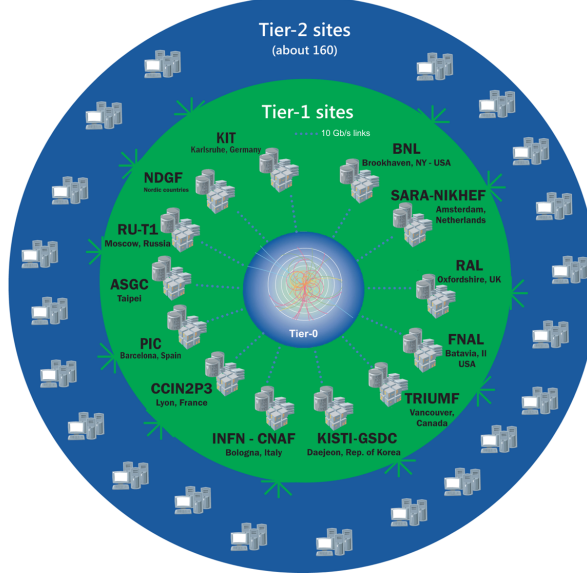


Figure 3.18: WLCG structure. The primary computer centers (Tier-0) are located at CERN (data center) and at the Wigner datacenter in Budapest. Tier-1 is composed of 13 centers and Tier-2 is composed of about 160 centers. [78].

1341 primary computing centers of the WLCG are located at the CERN and the Wigner
 1342 datacenter in Budapest and are known as Tier-0 as shown in figure 3.18. The main
 1343 responsibilities for each tier level are [78]

- 1344 • **Tier-0:** initial reconstruction of recorded events and storage of the resulting
 1345 datasets, the distribution of raw data to the Tier-1 centers.
- 1346 • **Tier-1:** provide storage capacity, support for the Grid, safe-keeping of a pro-
 1347 portional share of raw and reconstructed data, large-scale reprocessing and safe-
 1348 keeping of corresponding output, generation of simulated events, distribution
 1349 of data to Tier 2s, safe-keeping of a share of simulated data produced at these
 1350 Tier 2s.
- 1351 • **Tier-2:** store sufficient data and provide adequate computing power for specific
 1352 analysis tasks, provide analysis requirements and proportional share of simu-
 1353 lated event production and reconstruction.

1354 Aside from the general computing strategy to manage the huge amount of data pro-
1355 duced by experiments, CMS uses a framework to perform a variety of processing,
1356 selection and analysis tasks. The central concept of the CMS data model referred to
1357 as “event data model” (EDM) is the “Event”; therefore, an event is the unit that con-
1358 tains the information from a single bunch crossing as well as any data derived from
1359 that information like the reconstructed objects, the details under which additional
1360 data are derived.

1361

1362 Events are passed as the input to the “physics modules” that obtain information from
1363 them and create new one; for instance, “event data producers” add new data into the
1364 events, “analyzers” produce an information summary from an event set, “filters” per-
1365 form selection and triggering.

1366

1367 CMS uses several event formats with different levels of detail and precision

1368 • **Raw format:** events in this format contain the full recorded information from
1369 the detector as well as trigger decision and other metadata. An extended version
1370 of raw data is used to store information from the CMS Monte Carlo simulation
1371 tools. Raw data are stored permanently, occupying about 2MB/event

1372 • **RECO format:** events in this format correspond to raw data that have been
1373 submitted to reconstruction algorithms like primary and secondary vertex re-
1374 construction, particle ID, track-finding. RECO events contain physical objects
1375 and all the information used to reconstruct them; average size is about 0.5
1376 MB/event.

1377 • **AOD format:** Analysis Object Data (AOD) is the data format used in the
1378 physics analyses given that it contains the parameters describing the high-level

1379 physics objects in addition to enough information to allow a kinematic refitting if
 1380 needed. AOD events are filtered versions of the RECO events to which skimming
 1381 or other kind processes have been applied. Requires about 100 kB/event.

1382 • **Non-event data** are data needed to interpret and reconstruct events. Some
 1383 of the non-event data used by CMS contains information about the detector
 1384 contraction and condition data like calibrations, alignment, and detector status.

1385 Figure 3.19 shows the data flow scheme between CMS detector and hardware tiers.

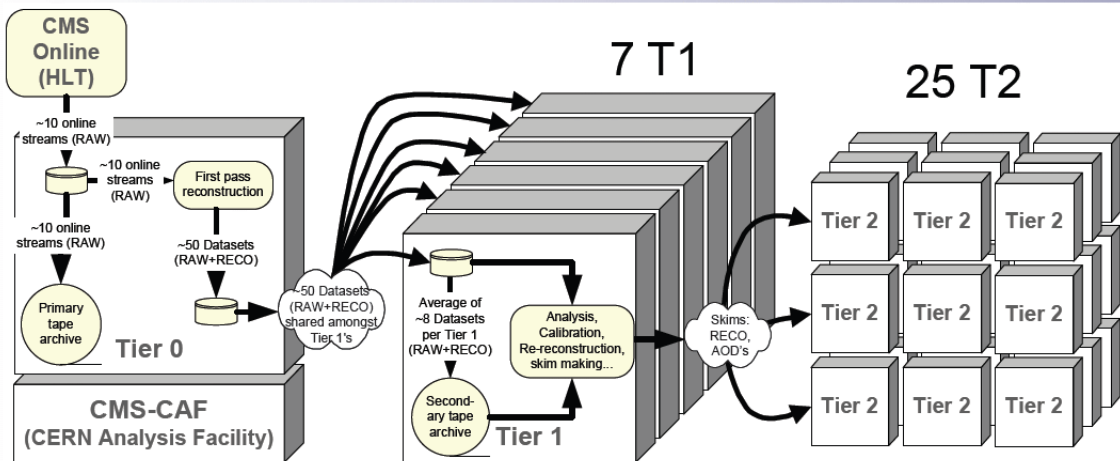


Figure 3.19: Data flow from CMS detector through hardware Tiers.

1386 The whole collection of software built as a framework is referred to as “CMSSW”. This
 1387 framework provides the services needed by the simulation, calibration and alignment,
 1388 and reconstruction modules that process event data, so that physicists can perform
 1389 analysis. The CMSSW event processing model is composed of one executable, called
 1390 cmsRun, and several plug-in modules which contains all the tools (calibration, recon-
 1391 struction algorithms) needed to process an event. The same executable is used for
 1392 both detector and Monte Carlo data [79].

₁₃₉₃ **Chapter 4**

₁₃₉₄ **Event generation, simulation and
reconstruction**

₁₃₉₆ The process of analyzing the data recorded by the CMS experiment involves several
₁₃₉₇ stages where the data are processed in order to interpret the information provided by
₁₃₉₈ all the detection systems; in those stages, the particles produced after the pp collision
₁₃₉₉ are identified by reconstructing their trajectories and measuring their features. In
₁₄₀₀ addition, the SM provides a set of predictions that have to be compared with the
₁₄₀₁ experimental results; however, in most of the cases, theoretical predictions are not
₁₄₀₂ directly comparable to experimental results due to the diverse source of uncertainties
₁₄₀₃ introduced by the experimental setup and theoretical approximations among others.

₁₄₀₄

₁₄₀₅ The strategy to face these conditions consist in using statistical methods implemented
₁₄₀₆ in computational algorithms to produce numerical results that can be contrasted with
₁₄₀₇ the experimental results. These computational algorithms are commonly known as
₁₄₀₈ Monte Carlo (MC) methods and, in the case of particle physics, they are designed to
₁₄₀₉ apply the SM rules and produce predictions about the physical observables measured

in the experiments. Since particle physics is governed by quantum mechanics principles, predictions are not allowed for single events; therefore, a high number of events are “generated” and predictions are produced in the form of statistical distributions for the observables. Effects of the detector presence are included in the predictions by introducing simulations of the detector itself.

1415

1416 This chapter presents a description of the event generation strategy and the tools
 1417 used to perform the detector simulation and physics objects reconstruction. A comprehensive review of event generators for LHC physics can be found in reference [80]
 1419 on which this chapter is based.

1420 4.1 Event generation

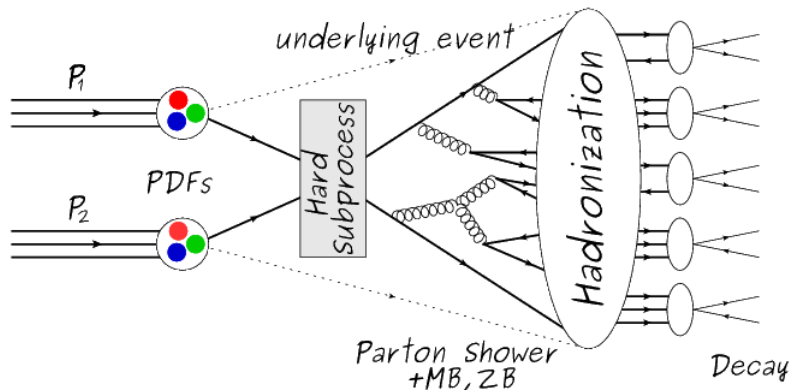


Figure 4.1: Event generation process. In the first step, the PDF of the colliding particles is considered so the specific interaction is described. The actual interaction is generated in the hard subprocess; the cross-section of the process is calculated from the matrix element connecting the initial and final states. The parton shower describes the evolution of the partons from the hard subprocess according to the DGLAP equations. At this step, the underlying event and PU effects are included in the generation. The resulting partons from the parton shower are recombined to form hadrons in the hadronization step; most of them are unstable, therefore, their decays are also generated in agreement to the known branching ratios. Modified from reference [81].

1421 The event generation is intended to create events that mimic the behavior of actual
 1422 events produced in the collisions; they obey a sequence of steps from the particles colli-
 1423 sion hard process to the decay process into the final state particles. Figure 4.1 shows
 1424 a schematic view of the event generation process; the fact that the full process can
 1425 be treated as several independent steps is based on the QCD factorization theorem.

1426

1427 Generation starts by taking into account the PDFs of the incoming particles. Event
 1428 generators offer the option to choose from several PDF sets depending on the partic-
 1429 ular process under simulation¹; in the following pp collisions will be considered. The
 1430 *hard subprocess* describes the actual interaction between partons from the incoming
 1431 protons; it is represented by the matrix element connecting the initial and final states
 1432 of the interaction. Normally, the matrix element can be written as a sum over Feyn-
 1433 man diagrams and consider interferences between terms in the summation. During
 1434 the generation of the hard subprocess, the production cross section is calculated.

1435

1436 The order to which the cross section is calculated depends on the order of the Feyn-
 1437 man diagrams involved in the calculation; therefore, radiative corrections are included
 1438 by considering a higher order Feynman diagrams where QCD radiation dominates.
 1439 Currently, cross sections calculated to LO do not offer a satisfactory description of the
 1440 processes, i.e., the results are only reliable for the shape of distributions; therefore,
 1441 NLO calculations have to be performed with the implication that the computing time
 1442 needed is highly increased.

1443

1444 The final parton content of the hard subprocess is subjected to the *parton shower*
 1445 which generates the gluon radiation. Parton shower evolves the partons; i.e., gluons

¹ Tool in Reference [82] allows to plot different PDF sets under customizable conditions.

1446 split into quark-antiquark pairs and quarks of enough energy radiate gluons giving rise
 1447 to further parton multiplication, following the DGLAP (Dokshitzer-Gribov-Lipatov-
 1448 Altarelli-Parisi) equations. Showering continues until the energy scale is low enough
 1449 to reach the non-perturbative limit.

1450

1451 In the simulation of LHC processes that involve b quarks like the single top quark or
 1452 Higgs associated production, it is needed to consider that the b quark is heavier than
 1453 the proton; in this sense, the QCD interaction description is made in two different
 1454 schemes [83]

1455 • four-flavor (4F) scheme. b quarks appear only in the final state because they
 1456 are heavier than the proton and therefore they can be produced only from the
 1457 splitting of a gluon into pairs or singly in association with a t quark in high
 1458 energy-scale interactions. During the simulation, the b -PDFs are set to zero
 1459 because it cannot be part of the proton. Calculations in this scheme are more
 1460 complicated due to the presence of the second b quark but the full kinematics is
 1461 considered already at LO and therefore the accuracy of the description is better.

1462 • five-flavor (5F) scheme. b quarks are considered massless, therefore they can
 1463 appear in both initial and final states since it can now be part of the proton; thus,
 1464 during the simulation b -PDFs are not set to zero. In this scheme, calculations
 1465 are simpler than in the 4F scheme and possible logarithmic divergences are
 1466 absorbed by the PDFs through the DGLAP evolution.

1467 In this thesis, the tHq events are generated using the 4F scheme in order to reduce
 1468 uncertainties, while the tHW events are generated using the 5F scheme to eliminate
 1469 LO interference with the $t\bar{t}H$ process [48].

1470

1471 Partons involved in the pp collision are the focus of the simulation, however, the rest
 1472 of the partons inside the incoming protons are also affected because the remnants are
 1473 colored objects; also, multiple parton interactions can occur. The hadronization of
 1474 the remnants and multiple parton interactions are known as “underlying event” and
 1475 it has to be included in the simulation. In addition, multiple pp collisions in the same
 1476 bunch crossing (pile-up mentioned in 3.2) occurs, actually in two forms

- 1477 • *in-time PU* which refers to multiple pp collision in the bunch crossing but that
 1478 are not considered as primary vertices.
- 1479 • *Out-of-time PU* which refers to overlapping pp collisions from consecutive bunch
 1480 crossings; this can occurs due to the time-delays in the detection systems where
 1481 information from one bunch crossing is assigned to the next or previous one.

1482 While the underlying event effects are included in generation using generator-specific
 1483 tools, PU effects are added to the generation by overlaying Minimum-bias (MB) and
 1484 Zero-bias (ZB) events to the generated events. MB events are inelastic events selected
 1485 by using a loose (minimum bias) trigger with as little bias as possible, therefore ac-
 1486 cepting a large fraction of the overall inelastic event; ZB events correspond to random
 1487 events recorded by the detector when collisions are likely. MB model in-time PU and
 1488 ZB model out-of-time PU.

1489

1490 The next step in the generation process is called “hadronization”. Since particles
 1491 with a net color charge are not allowed to exits isolated, they have to recombine
 1492 to form bound states. This is precisely the process by which the partons resulting
 1493 from the parton shower arrange themselves as color singlets to form hadrons. At
 1494 this step, the energy-scale is low and the strong coupling constant is large, there-
 1495 fore hadronization process is non-perturbative and the evolution of the partons is

1496 described using phenomenological models. Most of the baryons and mesons produced
 1497 in the hadronization are unstable and hence they will decay in the detector.

1498

1499 The last step in the generation process corresponds to the decay of the unstable
 1500 particles generated during hadronization; it is also simulated in the hadronization
 1501 step, based on the known branching ratios.

1502 4.2 Monte Carlo Event Generators.

1503 The event generation described in the previous section has been implemented in
 1504 several software packages for which a brief description is given.

- 1505 • **PYTHIA 8.** It is a program designed to perform the generation of high en-
 1506 ergy physics events which describe the collisions between particles such as elec-
 1507 trons, protons. Several theories and models are implemented in it, in order to
 1508 describe physical aspects like hard and soft interaction, parton distributions,
 1509 initial and final-state parton showers, multiple parton interactions, beam rem-
 1510 nants, hadronization² and particle decay. Thanks to extensive testing, several
 1511 optimized parametrizations, known as “tunings”, have been defined in order
 1512 to improve the description of actual collisions to a high degree of precision; for
 1513 analysis at $\sqrt{s} = 13$ TeV, the underline event CUETP8M1 tune is employed [85].
 1514 The calculation of the matrix element is performed at LO which is not enough
 1515 for the current required level of precision; therefore, pythia is often used for
 1516 parton shower, hadronization and decays, while other event generators are used
 1517 to generate the matrix element at NLO.

² based in the Lund string model [84]

1518 • **MadGraph5_aMC@NLO.** MadGraph is a matrix element generator which
 1519 calculates the amplitudes for all contributing Feynman diagrams of a given pro-
 1520 cess but does not provide a parton shower while MC@NLO incorporate NLO
 1521 QCD matrix elements consistently into a parton shower framework; thus, Mad-
 1522 Graph5_aMC@NLO, as a merger of the two event generators MadGraph5 and
 1523 aMC@NLO, is an event generator capable to calculate tree-level and NLO cross
 1524 sections and perform the matching of those with the parton shower. It is one of
 1525 the most frequently used matrix element generators; however, it has the partic-
 1526 ular feature of the presence of negative event weights which reduce the number
 1527 of events used to reproduce the properties of the objects generated [86].

1528

1529 • **POWHEG.** It is an NLO matrix element generator where the hardest emis-
 1530 sion of color charged particles is generated in such a way that the negative event
 1531 weights issue of MadGraph5_aMC@NLO is overcome; however, the method re-
 1532 quires an interface with p_T -ordered parton shower or a parton shower generator
 1533 where this highest emission can be vetoed in order to avoid double counting of
 1534 this highest-energetic emission. PYTHIA is a commonly matched to POWHEG
 1535 event generator [87].

1536 Events resulting from the whole generation process are known as MC events.

1537 4.3 CMS detector simulation.

1538 After generation, MC events contain the physics of the collisions but they are not
 1539 ready to be compared to the events recorded by the experiment since these recorded
 1540 events correspond to the response of the detection systems to the interaction with

1541 the particles traversing them. The simulation of the CMS detector has to be applied
1542 on top of the event generation; it is simulated with a MC toolkit for the simulation
1543 of particles passing through matter called Geant4 which is also able to simulate the
1544 electronic signals that would be measured by all detectors inside CMS.

1545

1546 The simulation takes the generated particles contained in the MC events as input,
1547 makes them pass through the simulated geometry, and models physics processes that
1548 particles experience during their passage through matter. The full set of results from
1549 particle-matter interactions correspond to the simulated hit which contains informa-
1550 tion about the energy loss, momentum, position. Particles of the input event are
1551 called “primary”, while the particles originating from GEANT4-modeled interactions
1552 of a primary particle with matter are called a “secondary”. Simulated hits are the in-
1553 put of subsequent modules that emulate the response of the detector readout system
1554 and triggers. The output from the emulated detection systems and triggers is known
1555 as digitization [88, 89].

1556

1557 The modeling of the CMS detector corresponds to the accurate modeling of the
1558 interaction among particles, the detector material, and the magnetic field. This
1559 simulation procedure includes the following standard steps

- 1560 • Modeling of the Interaction Region.
- 1561 • Modeling of the particle passage through the hierarchy of volumes that compose
1562 CMS detector and of the accompanying physics processes.
- 1563 • Modeling of the effect of multiple interactions per beam crossing and/or the
1564 effect of events overlay (Pile-Up simulation).

1565 • Modeling of the detector’s electronics response, signal shape, noise, calibration
 1566 constants (digitization).

1567 In addition to the full simulation, i.e. a detailed detector simulation, a faster simula-
 1568 tion (FastSim) have been developed, that may be used where much larger statistics
 1569 are required. In FastSim, detector material effects are parametrized and included in
 1570 the hits; those hits are used as input of the same higher-level algorithms³ used to an-
 1571 alyze the recorded events. In this way, comparisons between fast and full simulations
 1572 can be performed [91].

1573

1574 After the full detector simulation, the output events can be directly compared with
 1575 events actually recorded in the CMS detector. The collection of MC events that
 1576 reproduce the expected physics for a given process are known as MC samples.

1577 4.4 Event reconstruction.

1578 In contrast to MC samples for which all the particles’ information is available from
 1579 it’s identity to its mass and energy, recorded events contain the electronic signals,
 1580 provided by the CMS detection systems, encoding the interaction of physical parti-
 1581 cles with the detector matter; these electronic signals have to be combined in order
 1582 to identify these particles and measure their features i.e., particles have to be “recon-
 1583 structed” using the signals provided by the detection systems. The CMS experiment
 1584 use the “particle-flow event reconstruction algorithm (PF)” to do the reconstruction
 1585 of particles produced in pp collisions. Next sections will present a basic description

³ track fitting, calorimeter clustering, b tagging, electron identification, jet reconstruction and calibration, trigger algorithms which will be considered in the next sections

1586 of the *Elements* used by PF (tracker tracks, energy clusters, and muon tracks), based
 1587 in the references [92, 93] where more detailed descriptions can be found.

1588 **4.4.1 Particle-Flow Algorithm.**

1589 Each of the several sub detection systems of the CMS detector is dedicated to identi-
 1590 fying a specific type of particles, i.e., photons and electrons are absorbed by the ECAL
 1591 and their reconstruction is based on ECAL information; hadrons are reconstructed
 1592 from clusters in the HCAL while muons are reconstructed from hits in the muon
 1593 chambers. PF is designed to correlate signals from all the detector layers (tracks and
 1594 energy clusters) in order to reconstruct and identify each final state particle and its
 1595 properties as sketched in figure 4.2.

1596

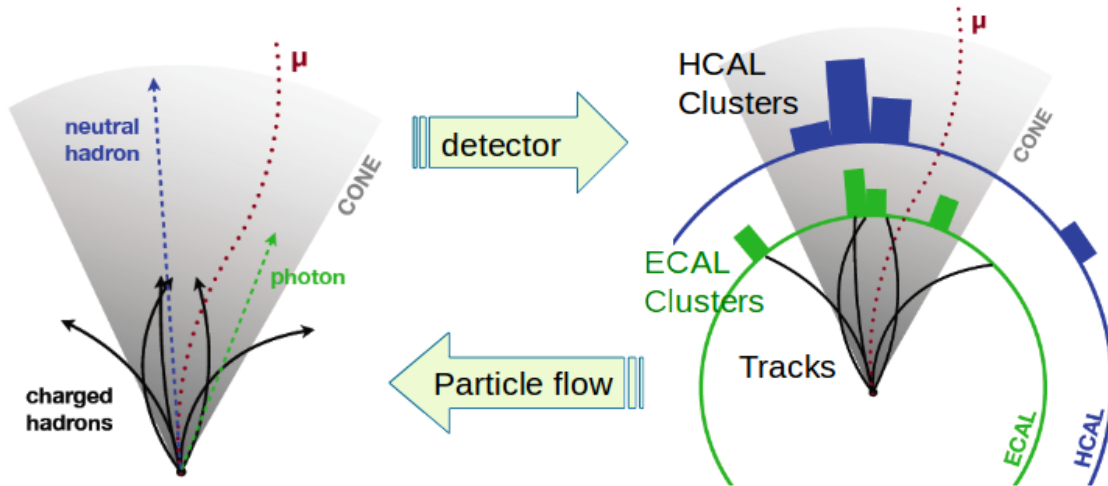


Figure 4.2: Particle flow algorithm. Information from the several CMS detection systems if provided as input to the algorithm which then combine it to identify and reconstruct all the particles in the final state and their properties. Reconstruction of simulated events is also performed by providing information from MC samples, detector and trigger simulation [94].

1597 For instance, a charged hadron is identified by a geometrical connection, know as *link*
 1598 between one or more calorimeter clusters and a track in the tracker provided there

1599 are no hits in the muon system; combining several measurements allows a better
 1600 determination of the energy and charge sign of the charged hadron.

1601 **Charged-particle track reconstruction.**

1602 The strategy used by PF in order to reconstruct tracks is called “Iterative Tracking”
 1603 which occurs in four steps

1604 • Seed generation where initial track candidates are found by looking for a combi-
 1605 nation of hits in the pixel detector, strip tracker, and muon chambers. In total
 1606 ten iterations are performed, each one with a different seeding requirement.
 1607 Seeds are used to estimate the trajectory parameters and uncertainties at the
 1608 time of the full track reconstruction. Seeds are also considered track candidates.

1609 • Track finding using a tracking software known as Combinatorial Track Finder
 1610 (CTF) [95]. The seed trajectories are extrapolated along the expected flight
 1611 path of a charged particle, in agreement to the trajectory parameters obtained
 1612 in the first step, in an attempt to find additional hits that can be assigned to
 1613 the track candidates.

1614 • Track-fitting where the found tracks are passed as input to a module which
 1615 provides the best estimate of the parameters of each trajectory.

1616 • Track selection where track candidates are submitted to a selection which dis-
 1617 cards those that fail a set of defined quality criteria.

1618 Iterations differ in the seeding configuration and the final track selection as elaborated
 1619 in references [92, 93]. In the first iteration, high p_T tracks and tracks produced near
 1620 to the interaction region are identified and those hits are masked thereby reducing
 1621 the combinatorial complexity. Next iterations search for more complicated tracks,

1622 like low p_T tracks and tracks from b hadron decays, which tend to be displaced from
 1623 the interaction region.

1624 **Vertex reconstruction.**

1625 During the track reconstruction, an extrapolation toward to the calorimeters is per-
 1626 formed in order to match energy deposits; that extrapolation is performed also toward
 1627 the beamline in order to find the origin of the track known as *vertex*. The vertex re-
 1628 construction is performed by selecting from the available reconstructed tracks, those
 1629 that are consistent with being originated in the interaction region where pp collisions
 1630 are produced. The selection involves a requirement on the number of tracker (pixel
 1631 and strip) hits and the goodness of the track fit.

1632

1633 Selected tracks are clustered using a “deterministic annealing algorithm (DA)”⁴. A
 1634 set of candidate vertices and their associated tracks, resulting from the DA, are then
 1635 fitted with an “adaptive vertex fitter (AVF)” to produce the best estimate of the
 1636 vertices locations.

1637

1638 The p_T of the several tracks associated to a reconstructed vertex is added, squared and
 1639 used to organize the vertices; the vertex with the highest squared sum is designated
 1640 as the *primary vertex (PV)* while the rest are designated as PU vertices.

1641 **Calorimeter clustering.**

1642 After traversing the CMS tracker system, electrons, photons and hadrons deposit their
 1643 energy in the ECAL and HCAL cells. The PF clustering algorithm aims to provide
 1644 a high detection efficiency even for low-energy particles and an efficient distinction

⁴ DA algorithm and AVF are described in detail in references [97,98]

1645 between close energy deposits. The clustering runs independently in the ECAL barrel
 1646 and endcaps, HCAL barrel and endcaps, and the two preshower layers, following two
 1647 steps

- 1648 • cells with an energy larger than a given seed threshold and larger than the energy
 1649 of the neighboring cells are identified as cluster seeds. The neighbor cells are
 1650 those that either share a side with the cluster seed candidate, or the eight closest
 1651 cells including cells that only share a corner with the seed candidate.
- 1652 • cells with at least a corner in common with a cell already in the cluster seed
 1653 and with an energy above a cell threshold are grouped into topological clusters.

1654 Clusters formed in this way are known as *particle-flow clusters*. With this clustering
 1655 strategy, it is possible to detect and measure the energy and direction of photons and
 1656 neutral hadrons as well as differentiate these neutral particles from the charged hadron
 1657 energy deposits. In cases involving charged hadrons for which the track parameters
 1658 are not determined accurately, for instance, low-quality and high- p_T tracks, clustering
 1659 helps in the energy measurements.

1660 Electron track reconstruction.

1661 Although the charged-particle track reconstruction described above works for elec-
 1662 trons, they lose a significant fraction of their energy via bremsstrahlung photon radi-
 1663 ation before reaching the ECAL; thus, the reconstruction performance depends on the
 1664 ability to measure also the radiated energy. The reconstruction strategy, in this case,
 1665 requires information from the tracking system and from the ECAL. Bremsstrahlung
 1666 photons are emitted at similar η values to that of the electron but at different values
 1667 of ϕ ; therefore, the radiated energy can be recovered by grouping ECAL clusters in a
 1668 η window over a range of ϕ around the electron direction. The group is called ECAL

1669 supercluster.

1670

1671 Electron candidates from the track-seeding and ECAL super clustering are merged
 1672 into a single collection which is submitted to a full electron tracking fit with a
 1673 Gaussian-sum filter (GSF) [96]. The electron track and its associated ECAL su-
 1674 percluster form a *particle-flow electron*.

1675 Muon track reconstruction.

1676 Given that the CMS detector is equipped with a muon spectrometer capable to iden-
 1677 tify and measure the momentum of the muons traversing it, the muon reconstruction
 1678 is not specific to PF; therefore, three different muon types are defined

- 1679 • *Standalone muon*. A clustering on the DTs or CSCs hits is performed to form
 1680 track segments; those segments are used as seeds for the reconstruction in the
 1681 muon spectrometer. All DTs, CSCs, and RPCs hits along the muon trajectory
 1682 are combined and fitted to form the full track. The fitting output is called a
 1683 *standalone-muon track*.
- 1684 • *tracker muon*. Each track in the inner tracker with p_T larger than 0.5 GeV and
 1685 a total momentum p larger than 2.5 GeV is extrapolated to the muon system. A
 1686 *tracker muon track* corresponds to the extrapolated tracks that match at least
 1687 one muon segment.
- 1688 • *Global muon*. When tracks in the inner tracker (inner tracks) and standalone-
 1689 muon tracks are matched and turn out being compatibles, their hits are com-
 1690 bined and fitted to form a *global-muon track*.

1691 Global muons sharing the same inner track with tracker muons are merged into a
 1692 single candidate. PF muon identification uses the muon energy deposits in ECAL,
 1693 HCAL, and HO associated with the muon track to improve the muon identification.

1694 **Particle identification and reconstruction.**

1695 PF elements are connected by a linker algorithm that tests the connection between any
 1696 pair of elements; if they are found to be linked, a geometrical distance that quantifies
 1697 the quality of the link is assigned. Two elements may be linked indirectly through
 1698 common elements. Linked elements form *PF blocks* and a PF block may contain
 1699 elements originating in one or more particles. Links can be established between
 1700 tracks, between calorimeter clusters, and between tracks and calorimeter clusters.
 1701 The identification and reconstruction start with a PF block and proceeds as follows

1702 • Muons. An “isolated global muon” is identified by evaluating the presence of
 1703 inner track and energy deposits close to the global muon track in the (η, ϕ)
 1704 plane, i.e., in a particular point of the global muon track, inner tracks and
 1705 energy deposits are sought within a radius of $\Delta R = 0.3$ (see eqn. 3.7) from the
 1706 muon track; if they exist and the p_T of the found track added to the E_T of the
 1707 found energy deposit does not exceed 10% of the muon p_T then the global muon
 1708 is an isolated global muon. This isolation condition is stringent enough to reject
 1709 hadrons misidentified as muons.

1710 “Non-isolated global muons” are identified using additional selection require-
 1711 ments on the number of track segments in the muon system and energy deposits
 1712 along the muon track. Muons inside jets are identified with more stringent crite-
 1713 ria in isolation and momentum as described in reference [99]. The PF elements
 1714 associated with an identified muon are masked from the PF block.

- 1715 ● Electrons are identified and reconstructed as described above plus some addi-
 1716 tional requirements on fourteen variables like the amount of energy radiated,
 1717 the distance between the extrapolated track position at the ECAL and the po-
 1718 sition of the associated ECAL supercluster among others, which are combined
 1719 in a specialized multivariate analysis strategy that improves the electron iden-
 1720 tification. Tracks and clusters used to identify and reconstruct electrons are
 1721 masked in the PF block.
- 1722 ● Isolated photons are identified from ECAL superclusters with E_T larger than 10
 1723 GeV, for which the energy deposited at a distance of 0.15, from the supercluster
 1724 position on the (η, ϕ) plane, does not exceed 10% of the supercluster energy;
 1725 note that this is an isolation requirement. In addition, there must not be links
 1726 to tracks. Clusters involved in the identification and reconstruction are masked
 1727 in the PF block.
- 1728 ● Bremsstrahlung photons and prompt photons tend to convert to electron-positron
 1729 pairs inside the tracker, therefore, a dedicated finder algorithm is used to link
 1730 tracks that seem to originate from a photon conversion; in case those two tracks
 1731 are compatible with the direction of a bremsstrahlung photon, they are also
 1732 linked to the original electron track. Photon conversion tracks are also masked
 1733 in the PF block.
- 1734 ● The remaining elements in the PF block are used to identify hadrons. In the
 1735 region $|\eta| \leq 2.5$, neutral hadrons are identified with HCAL clusters not linked
 1736 to any track while photons from neutral pion decays are identified with ECAL
 1737 clusters without links to tracks. In the region $|\eta| > 2.5$ ECAL clusters linked to
 1738 HCAL clusters are identified with a charged or neutral hadron shower; ECAL
 1739 clusters with no links are identified with photons. HCAL clusters not used yet,

1740 are linked to one or more unlinked tracks and to an unlinked ECAL in order to
 1741 reconstruct charged-hadrons or a combination of photons and neutral hadrons
 1742 according to certain conditions on the calibrated calorimetric energy.

- 1743 • Charged-particle tracks may be liked together when they converge to a “sec-
 1744 ondary vertex (SV) ” displaced from the interaction point where the PV and
 1745 PU vertices are reconstructed; at least three tracks are needed in that case,
 1746 of which at most one has to be an incoming track with hits in tracker region
 1747 between a PV and the SV.

1748

1749 The linker algorithm, as well as the whole PF algorithm, has been validated and
 1750 commissioned; results from that validation are presented in the references [92].

1751 **Jet reconstruction.**

1752 Quarks and gluons may be produced in the pp collisions, therefore, their hadronization
 1753 will be seen in the detector as a shower of hadrons and their decay products in the
 1754 form of a “jet”. The anti- k_t algorithm [100] is used to perform the jet reconstruction
 1755 by clustering those PF particles within a cone (see figure 4.3); previously, isolated
 1756 electrons, isolated muons, and charged particles associated with other interaction
 1757 vertices are excluded from the clustering.

1758 The anti- k_t algorithm proceeds in a sequential recombination of PF particles; the
 1759 distance between particles i and j (d_{ij}) and the distance between particles and the
 1760 beam are defined as

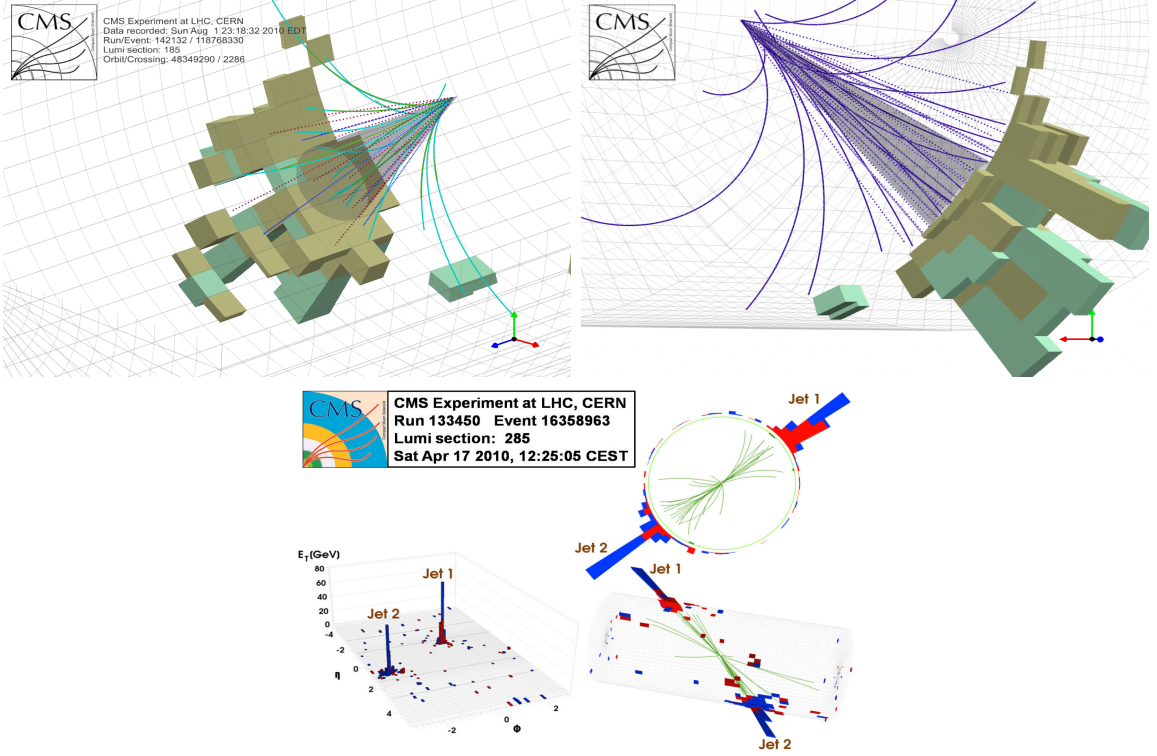


Figure 4.3: Jet reconstruction performed by the anti- k_t algorithm. Top: Two different views of a CMS recorded event are presented. Continuous lines correspond to the tracks left by charged particles in the tracker while dotted lines are the imaginary paths followed by neutral particles. The green cubes represent the ECAL cells while the blue ones represent the HCAL cells; in both cases, the height of the cube represent the amount of energy deposited in the cells [101]. Bottom: Reconstruction of a recorded event with two jets [102].

$$d_{ij} = \min\left(\frac{1}{k_{ti}^2}, \frac{1}{k_{tj}^2}\right) \frac{\Delta_{ij}^2}{R^2}$$

$$d_{iB} = \frac{1}{k_{ti}^2} \quad (4.1)$$

1761 where $\Delta_{ij}^2 = (y_i - y_j)^2 + (\phi_i - \phi_j)^2$, k_{ti} , y_i and ϕ_i are the transverse momentum, ra-
 1762 pidity and azimuth of particle i respectively and R is the called jet radius. For all
 1763 the remaining PF particles, after removing the isolated ones, d_{ij} and d_{iB} are calcu-

1764 lated⁵ and the smallest is identified; if it is a d_{ij} , particles i and j are replaced with
 1765 a new object whose momentum is the vectorial sum of the combined particles. If the
 1766 smallest distance is a d_{iB} the clustering process ends, the object i (which at this stage
 1767 should be a combination of several PF particles) is declared as a *Particle-flow-jet* (PF
 1768 jet) and all the associated PF particles are removed from the detector. The clustering
 1769 process is repeated until no PF particles remain.

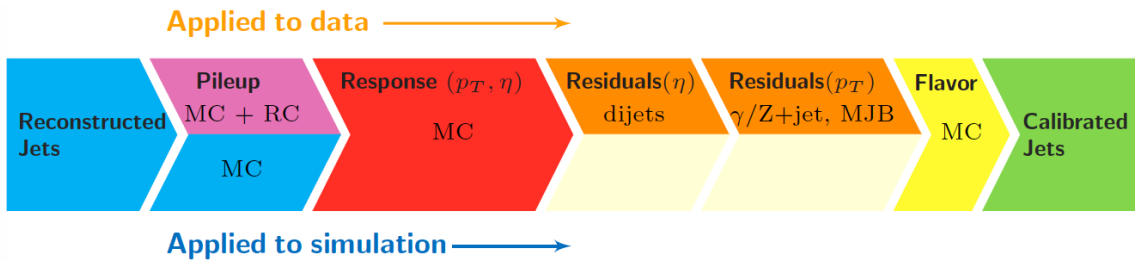


Figure 4.4: Jet energy correction diagram. Correction levels are applied sequentially in the indicated fixed order [104].

Even though jets can be reconstructed efficiently, there are some effects that are not included in the reconstruction and that lead to discrepancies between the reconstructed results and the predicted results; in order to overcome these discrepancies, a factorized model has been designed in the form of jet energy corrections (JEC) [103, 104] applied sequentially as shown in the diagram of figure 4.4.

1775 At each level, the jet four-momentum is multiplied by a scaling factor based on jet
1776 properties, i.e., η , flavor, etc.

- 1777 • Level 1 correction removes the energy coming from pile-up. The scale factor is
1778 determined using a MC sample of QCD dijet events with and without pileup
1779 overlay; it is parametrized in terms of the offset energy density ρ , jet area A ,
1780 jet η and jet p_T . Different corrections are applied to data and MC due to the
1781 detector simulation.

⁵ Notice that this is a combinatorial calculation.

- 1782 • MC-truth correction accounts for differences between the reconstructed jet en-
- 1783 ergy and the MC particle-level energy. The correction is determined on a QCD
- 1784 dijet MC sample and is parametrized in terms of the jet p_T and η .
- 1785 • Residuals correct remaining small differences within jet response in data and
- 1786 MC. The Residuals η -dependent correction compares jets of similar p_T in the
- 1787 barrel reference region. The Residuals p_T -dependent correct the jet absolute
- 1788 scale (JES vs p_T).
- 1789 • Jet-flavor corrections are derived in the same way as MC-truth corrections but
- 1790 using QCD pure flavor samples.

1791 ***b*-tagging of jets.**

1792 A particular feature of the hadrons containing bottom quarks (b-hadrons) is that
 1793 they have a lifetime long enough to travel some distance before decaying, but it is
 1794 not as long as those of light quark hadrons; therefore, when looking at the hadrons
 1795 produced in pp collisions, b-hadrons decay typically inside the tracker rather than
 1796 reach the calorimeters as some light-hadrons do. As a result, a b-hadron decay gives
 1797 rise to a displaced vertex (secondary vertex) with respect to the primary vertex as
 1798 shown in figure 4.5; the SV displacement is in the order of a few millimeters. A jet
 1799 resulting from the decay of a b-hadron is called *b* jet; other jets are called light jets.

1800

1801 Several methods to identify *b*-jets (*b*-tagging) have been developed; the method used in
 1802 this thesis is known as “Combined Secondary Vertex” algorithm in its second version
 1803 (CSVv2) [105]. By using information of the impact parameter, the reconstructed
 1804 secondary vertices and the jet kinematics in a multivariate analysis that combines
 1805 the discrimination power of each variable in one global discriminator variable, three

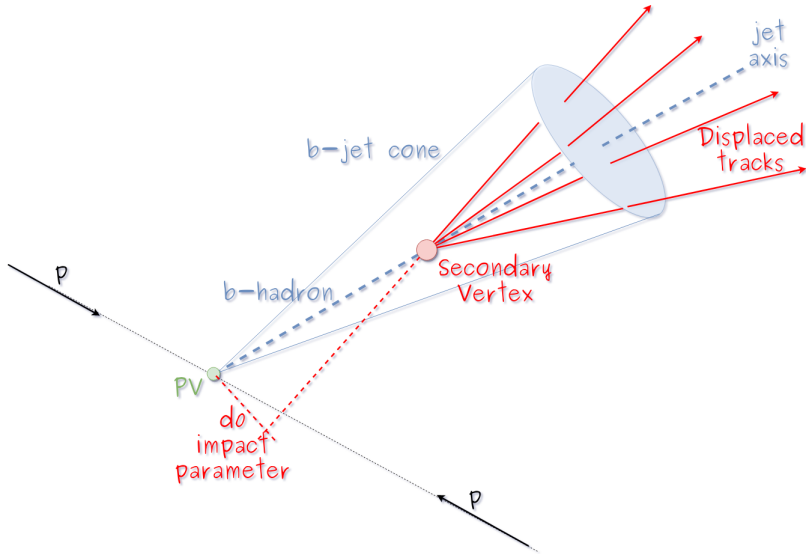


Figure 4.5: Secondary vertex in a b-hadron decay.

1806 working points (references): loose, medium and tight, are defined which quantify the
 1807 probabilities of mistag jets from light quarks as jets from b quarks; 10, 1 and 0.1 %
 1808 respectively. Although the mistagging probability decrease with the working point
 1809 strength, the efficiency to correctly tag b -jets also decrease as 83, 69 and 49 % for the
 1810 respective working point; therefore, a balance needs to be achieved according to the
 1811 specific requirements of the analysis.

1812 Missing transverse energy.

1813 The fact that proton bunches carry momentum along the z axis implies that for each
 1814 event, momentum balance in the transverse plane is expected. Imbalances are quan-
 1815 tified by the missing transverse energy (MET) and are attributed to several sources
 1816 including particles escaping undetected through the beam pipe, neutrinos produced in
 1817 weak interactions processes which do not interact with the detector and thus escaping
 1818 without leaving a sign, or even undiscovered particles predicted by models beyond
 1819 the SM.

1820

1821 The PF algorithm assign the negative sum of the momenta of all reconstructed PF
 1822 particles to the *particle-flow MET* according to

$$\vec{E}_T = - \sum_i \vec{p}_{T,i} \quad (4.2)$$

1823 JEC are propagated to the calculation of the \vec{E}_T as described in the reference [106].

1824

1825 4.4.2 Event reconstruction examples

1826 Figures 4.6-4.8 show the results of the reconstruction performed on 3 recorded events.
 1827 Descriptions are taken directly from the source.

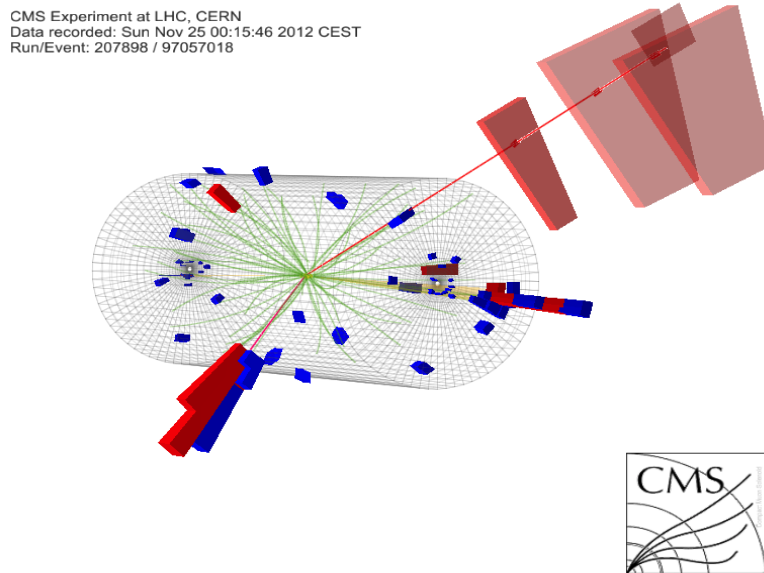


Figure 4.6: HIG-13-004 Event 1 reconstruction results; “HIG-13-004 Event 1: Event recorded with the CMS detector in 2012 at a proton-proton center-of-mass energy of 8 TeV. The event shows characteristics expected from the decay of the SM Higgs boson to a pair of τ leptons. Such an event is characterized by the production of two forward-going jets, seen here in opposite endcaps. One of the τ decays to a muon (red lines on the right) and neutrinos, while the other τ decays into a charged hadron and a neutrino.” [?].

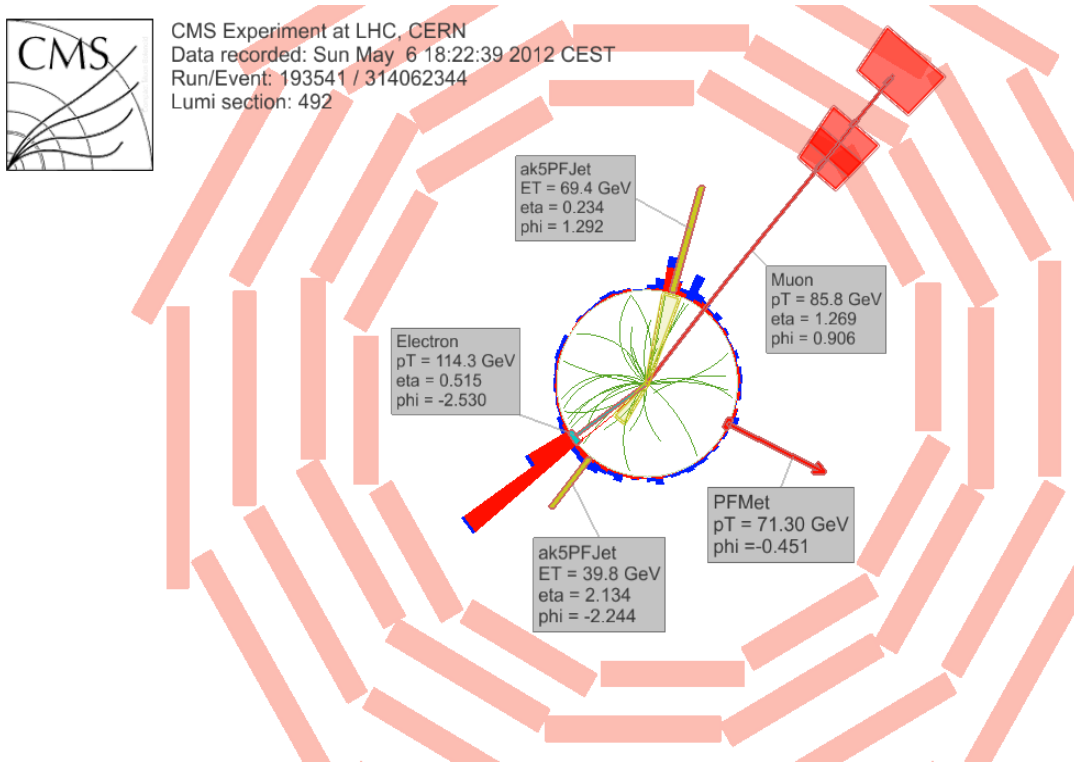


Figure 4.7: $e\mu$ event reconstruction results; “An $e\mu$ event candidate selected in 8 TeV data, as seen from the direction of the proton beams. The kinematics of the main objects used in the event selection are highlighted: two isolated leptons and two particle-flow jets. The reconstructed missing transverse energy is also displayed for reference” [?].

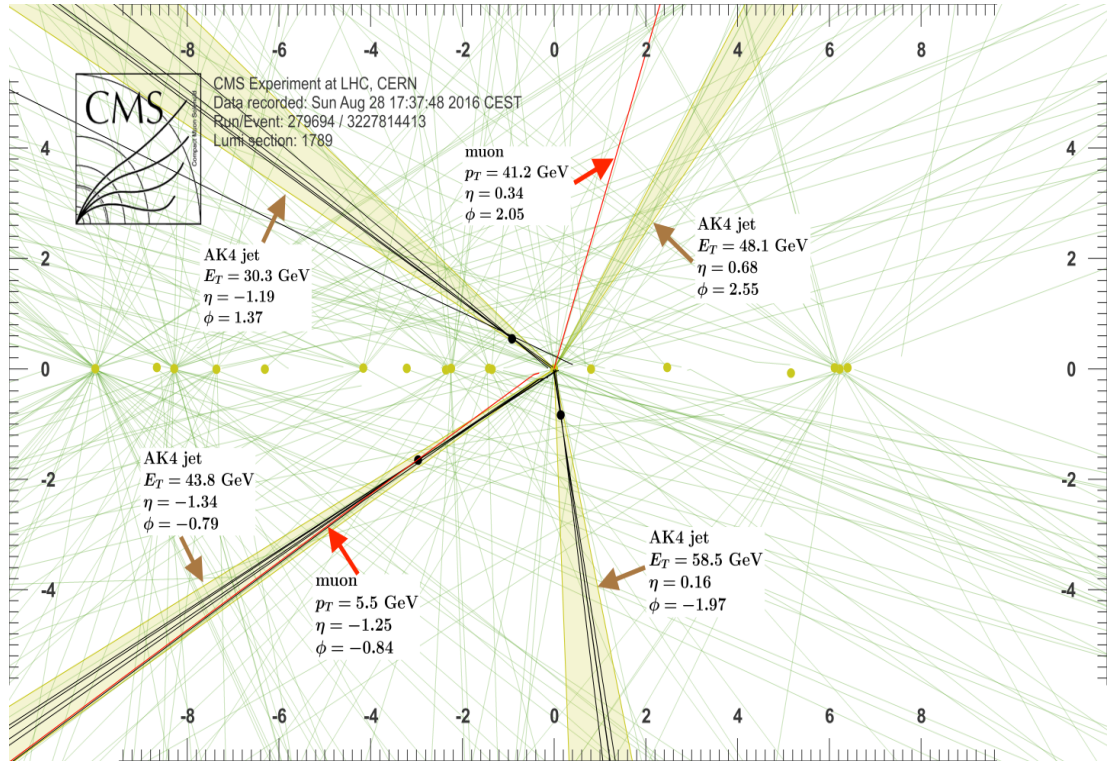


Figure 4.8: Recorded event reconstruction results;“Recorded event (ρ - z projection) with three jets with $p_T > 30$ GeV with one displaced muon track in 2016 data collected at 13 TeV. Each of the three jets has a displaced reconstructed vertex. The jet with $p_T(j) = 43.8$ GeV, $\eta(j) = -1.34$, $\phi(j) = -0.79$ contains muon with $p_T(\mu) = 5.5$ GeV, $\eta(\mu) = -1.25$, $\phi(\mu) = -0.84$. Event contains reconstructed isolated muon with $p_T(\mu) = 41.2$ GeV, $\eta(\mu) = 0.34$, $\phi(\mu) = 2.05$ and MET with $p_T = 72.5$ GeV, $\phi = -0.32$. Jet candidates for a b -jet from top quark leptonic and hadronic decays are tagged by CSVv2T algorithm. One of the other two jets is tagged by CharmT algorithm. Tracks with $p_T > 0.5$ GeV are shown. The number of reconstructed primary vertices is 18. Reconstructed $m_T(W)$ is 101.8 GeV. Beam spot position correction is applied. Reconstructed primary vertices are shown in yellow color, while reconstructed displaced vertices and associated tracks are presented in black color. Dimensions are given in cm” [107].

1828 **Chapter 5**

1829 **Statistical methods**

1830 In the course of analyzing the data sets provided by the CMS experiment and used in
1831 this thesis, several statistical tools have been employed; in this chapter, a description
1832 of these tools will be presented, starting with the general statement of the multivariate
1833 analysis method, followed by the particularities of the Boosted Decision Trees (BDT)
1834 method and its application to the classification problem. Statistical inference methods
1835 used will also be presented. This chapter is based mainly on the reference [108].

1836 **5.1 Multivariate analysis**

1837 Multivariate data analysis (MVA) makes reference to statistical techniques that an-
1838 alyze data containing information of more than one variable, commonly taking into
1839 account the effects of all variables on the response of the particular variable under
1840 investigation, i.e., considering all the correlations between variables. MVA is em-
1841 ployed in a variety of fields like consumer and market research, quality control and
1842 process optimization. From a MVA it is possible to identify the dominant patterns
1843 in the data, like groups, outliers and trends, and determine to which group a set of

1844 values belong; in the particle physics context, MVA methods are used to perform the
 1845 selection of certain type of events, from a large data set, using a potentially large
 1846 number of measurable properties for each event.

1847 Processes with small cross section, as the tHq process, normally are hidden behind
 1848 more common processes; therefore, the data set results in a subset of events with
 1849 characteristic features of interest (signal) mixed in randomly with a much larger
 1850 number of SM events that can mimic these features of interest (background) which
 1851 implies that it is not possible to say with certainty that a given event is signal or
 1852 background. In that sense, the problem can be formulated as one where a set of
 1853 events have to be classified according to some features; these features correspond to
 1854 the measurements of several parameters like energy, momentum organized in a set
 1855 of “input variables”. The measurements for each event can be written in a vector
 1856 $\mathbf{x} = (x_1, \dots, x_n)$ for which

- 1857 • Signal hypotheses $\rightarrow f(\mathbf{x}|s)$ is the probability density (“likelihood”) for \mathbf{x} given
 1858 it is a signal event
- 1859 • Background hypotheses $\rightarrow f(\mathbf{x}|b)$ is the probability density (“likelihood”) of \mathbf{x}
 1860 given it is a background event

1861 Figure 5.1 shows three ways to perform a classification of events for which mea-
 1862 surements of two properties, two input variables, have been performed; blue circles
 1863 represent signal events while red triangles represent background events. The classifi-
 1864 cation on (a) is “cut-based” requiring $x_1 < c_1$ and $x_2 < c_2$; usually the cut values are
 1865 chosen according to some knowledge about the event process. In (b), the classification
 1866 is performed by stating a cut involving a linear function of the input variables and
 1867 so the boundary, while in (c) the the relationship between the input variables is not
 1868 linear thus the boundary is not linear either.

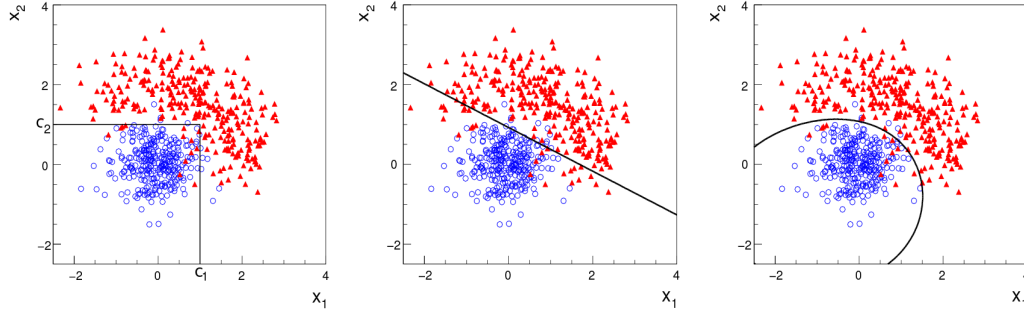


Figure 5.1: Scatter plots-MVA event classification. Distribution of two input variables x_1 and x_2 measured for a set of events; blue circles represent signal events and red triangles represent background events. The classification is based on (a) cuts, (b) linear boundary, and (c) nonlinear boundary [108]

1869 The boundary can be parametrized in terms of the input variables such that the
 1870 cut is set on the parametrization instead of on the variables, i.e., $y(\mathbf{x}) = y_{cut}$ with
 1871 y_{cut} a constant; thus, the acceptance or rejection of an event is based on what side
 1872 of the boundary is the event located. If $y(\mathbf{x})$ has functional form, it can be used to
 1873 determine the probability distribution functions $p(y|s)$ and $p(y|b)$ and then perform
 1874 a scalar test statistic with a single cut on the scalar variable y .

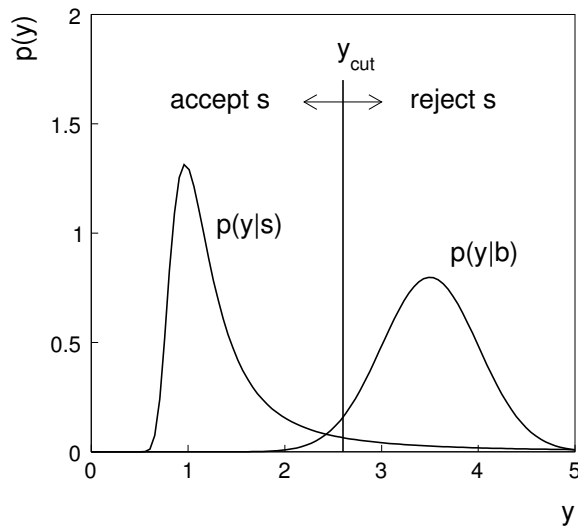


Figure 5.2: Distributions of the scalar test statistic $y(\mathbf{x})$ under the signal and background hypotheses. [108]

1875 Figure 5.2 illustrates what would be the probability distribution functions under
 1876 the signal and background hypotheses for a scalar test statistic with a cut on y .

1877 **5.1.1 Decision trees**

1878 For this thesis, the implementation of the MVA strategy, described above, is per-
 1879 formed through decision trees. In a simple picture, a decision tree classifies events
 1880 according to their input variables values by setting a cut on each input variable and
 1881 checking which events are on which side of the cut, just as proposed in the MVA
 1882 strategy, but in addition, as a machine learning algorithm, decision trees offer the
 1883 possibility to be trained and then perform the classification efficiently.

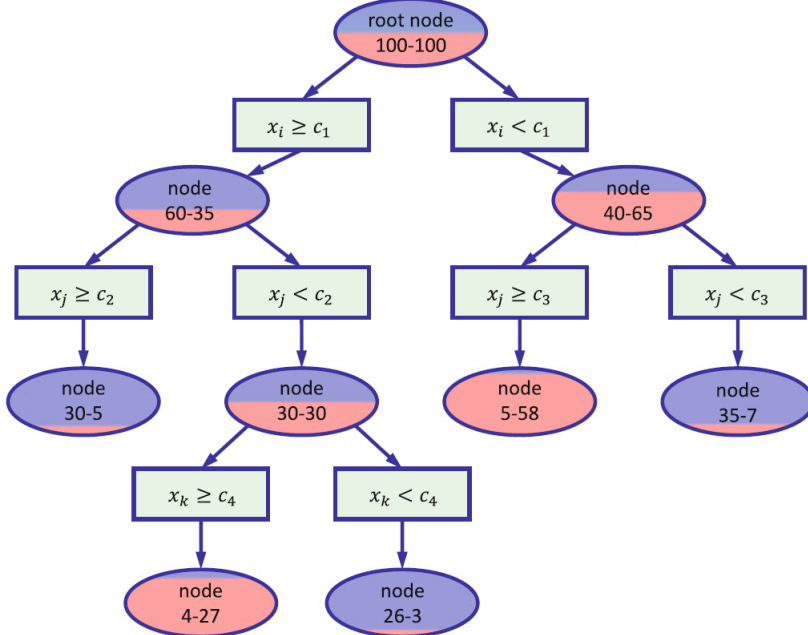


Figure 5.3: Example of a decision tree. Each node is fed with a MC sample mixing signal and background events (left-right numbers); nodes colors represent the relative amount of signal/background events [109].

1884 The training or growing of a decision tree is the process that defines the rules for
 1885 classifying events; this process is represented in figure 5.3 and consists of several steps

- 1886 • take MC samples of signal and background events and split them into two parts
- 1887 each; first parts form the training sample which will be used in the decision tree
- 1888 training, while the second parts form the test sample which will be used for
- 1889 testing the final classifier obtained from the training. Each event has associated
- 1890 a set of input variables $\mathbf{x} = (x_1, \dots, x_n)$ which serve to distinguish between signal
- 1891 and background events. The training sample is taken in at the root “node”.

- 1892 • pick one variable, say x_i

- 1893 • pick one value of x_i , each event has its own value of x_i , and split the training
- 1894 sample into two subsamples B_1 and B_2 ; B_1 contains events for which $x_i < c_1$
- 1895 while B_2 contains the rest of the training events;

- 1896 • scan all possible values of x_i and find the splitting value that provides the “best”
- 1897 classification¹, i.e., B_1 is mostly made of signal events while B_2 is mostly made
- 1898 of background events.

- 1899 • It is possible that variables other than the picked one produce a better classi-
- 1900 fication, hence, all the variables have to be evaluated. Pick the next variable,
- 1901 say x_j , and repeat the scan over its possible values.

- 1902 • At the end, all the variables and their values will have been scanned, the “best”
- 1903 variable and splitting value will have been identified, say x_1, c_1 , and there will
- 1904 be two nodes fed with the subsamples B_1 and B_2 .

- 1905 Nodes are further split by repeating the decision process until: a given number of
- 1906 final nodes is obtained, nodes are largely dominated by either signal or background
- 1907 events, or nodes has too few events to continue. Final nodes are called “leaves” and

¹ Quality of the classification will be treated in the next paragraph.

1908 they are classified as signal or background leaves according to the class of the majority
 1909 of events in them. Each “branch” in the tree corresponds to a sequence of cuts.

1910 The quality of the classification at each node is evaluated through a separation
 1911 criteria; there are several of them but the “Gini Index (G)” is the one used in the
 1912 decision trees trained for the analysis in this thesis. G is written in terms of the purity
 1913 (P), i.e. the fraction of signal events, of the samples after the separation is made; it
 1914 is given by

$$G = P(1 - P) \quad (5.1)$$

1915 notice that $P=0.5$ at the root node while $G=0$ for pure leaves. For a node A split
 1916 into two nodes B_1 and B_2 the G gain is

$$\Delta G = G(A) - G(B_1) - G(B_2) \quad (5.2)$$

1917 the “best” classification corresponds to that for which the gain of G is maximized;
 1918 hence, the scanning over all event’s variables and their values is of capital importance.

1919 The output of a decision tree is called “classifier”. Figure 5.4

1920 5.1.2 Boosted decision trees (BDT)

1921 Event misclassification occurs when a training event end up in the wrong leaf, i.e., a
 1922 signal event end up in a background leaf or a background event end up in a signal
 1923 leaf; a way to correct it is to assign a weight to the misclassified events such that when
 1924 used in the training of a new decision tree they get correctly classified. In the first
 1925 decision tree all the weights are set to the unity, hence, an event with increased weight
 1926 is a “boosted” event. The event reweighting if performed by a boosting algorithm
 1927 which also creates a set of trees, and hence a set of classifiers, which are combined

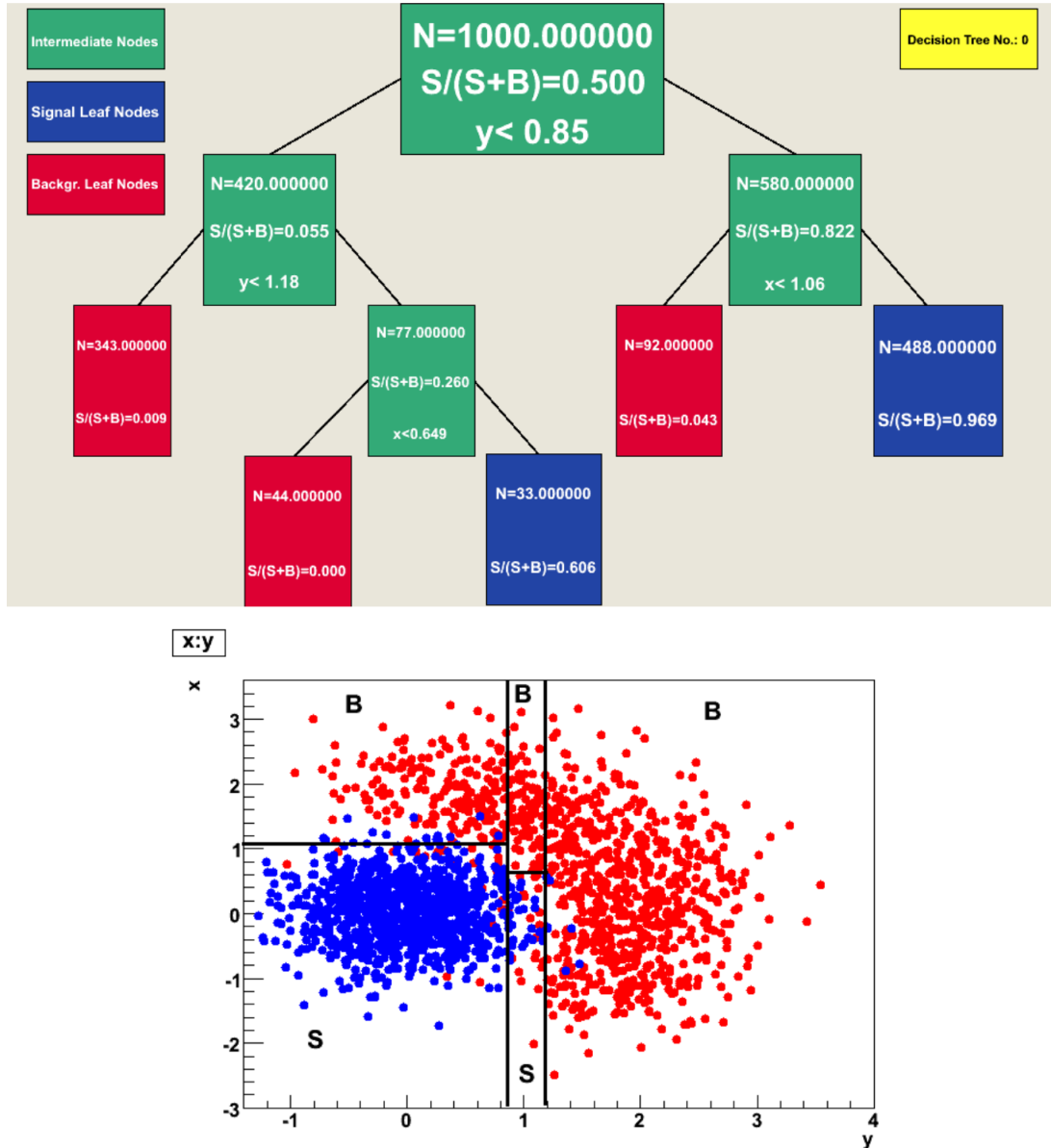


Figure 5.4: Example of a decision tree output. Each leaf, blue for signal events and red for background events, represent a region in the variables phase space [110].

1928 to create a new classifier; this new classifier offers more stability and has a smaller
 1929 misclassification rate than any individual ones.

1930 It is often applied to decision trees, precisely because they suffer from sensitivity
 1931 to statistical fluctuations in the training sample, but the technique can be applied to

1932 any classifier.

$$P = \frac{\sum_s w_s}{\sum_s w_s + \sum_b w_b} \quad (5.3)$$

1933 where w_s and w_b are the weights of the events in a weighted sample;

1934 By using a multitude of slightly altered decision trees and averaging over the
1935 predicted outcome

1936 Notice that the tails of the distributions indicate that some signal events fall
1937 on the rejection region and some background events fall on the acceptance region;
1938 therefore, it is convenient to define the “efficiency” with which events of a given type
1939 are accepted, thus, the signal and background efficiencies are given by

$$\varepsilon_s = P(\text{accept event}|s) = \int_A f(\mathbf{x}|s) d\mathbf{x} = \int_{-\infty}^{y_{\text{cut}}} p(y|s) dy, \quad (5.4)$$

$$\varepsilon_b = P(\text{accept event}|b) = \int_A f(\mathbf{x}|b) d\mathbf{x} = \int_{-\infty}^{y_{\text{cut}}} p(y|b) dy, \quad (5.5)$$

1940 where A is the acceptance region. Under these conditions, the background hy-
1941 pothesis corresponds to the “null hypothesis (H_0)”, the signal hypothesis corresponds
1942 to the “alternative hypothesis (H_1)”, the background efficiency is the significance level
1943 of the test, and signal efficiency is the power of the test; what is sought in an analysis
1944 is to maximize the power of the test relative to the significance level.

1945 ; it is achieved, according to the Neyman-Pearson lemma [111],

1946 by defining the acceptance region such that, for \mathbf{x} inside the region, the likelihood
1947 ratio, i.e., the ratio of probability distribution functions for signal and background,

- ¹⁹⁴⁸ **5.2 MVA methods, NN, BDT, boosting,**
¹⁹⁴⁹ **overtraining, variable ranking**
- ¹⁹⁵⁰ **5.3 statistical inference, likelihood**
¹⁹⁵¹ **parametrization**
- ¹⁹⁵² **5.4 nuisance parameters**
- ¹⁹⁵³ **5.5 exclusion limits**
- ¹⁹⁵⁴ **5.6 asymptotic limits**

¹⁹⁵⁵ **Chapter 6**

¹⁹⁵⁶ **Search for production of a Higgs**
¹⁹⁵⁷ **boson and a single top quark in**
¹⁹⁵⁸ **multilepton final states in pp**
¹⁹⁵⁹ **collisions at $\sqrt{s} = 13$ TeV**

¹⁹⁶⁰ **6.1 Introduction**

- ¹⁹⁶¹ Dont forget to mention previous constrains to ct check reference ?? and references
¹⁹⁶² <https://link.springer.com/content/pdf/10.1007%2FJHEP01>
¹⁹⁶³ A. Azatov, R. Contino and J. Galloway, "Model-Independent Bounds on a
¹⁹⁶⁴ Light Higgs," JHEP 1204 (2012) 127 [arXiv:1202.3415 [hep-ph]].
¹⁹⁶⁵ J. R. Espinosa, C. Grojean, M. Muhlleitner and M. Trott, "Fingerprinting
¹⁹⁶⁶ Higgs Suspects at the LHC," JHEP 1205 (2012) 097 [arXiv:1202.3697 [hep-ph]].
¹⁹⁶⁷ This chapter present the search for the associated production of a Higgs boson and
¹⁹⁶⁸ a single top quark events with three leptons in the final state, targeting Higgs decay

1969 modes to WW , ZZ , and $\tau\tau$. The analysis uses the 13 TeV dataset produced in 2016,
 1970 corresponding to an integrated luminosity of 35.9fb^{-1} . It is based on and expands
 1971 previous analyses at 8 TeV [?, ?] and searches for associated production of $t\bar{t}$ and
 1972 Higgs in the same channel [?], and complements searches in other decay channels
 1973 targeting $H \rightarrow b\bar{b}$ [?].
 1974 As showed in section 2.4, the cross section of the associated production of a Higgs
 1975 boson and a single top quark (tHq) process is driven by a destructive interference of
 1976 two contributions (see Figure 6.1), where the Higgs couples to either the W boson or
 1977 the top quark. Any deviation from the standard model (SM) in the Higgs coupling
 1978 structure could therefore lead to a large enhancement of the cross section, making
 1979 this analysis sensitive to such deviations. A second process, where the Higgs and
 1980 top quark are accompanied by a W boson (tHW) has similar behavior, albeit with a
 1981 weaker interference pattern.

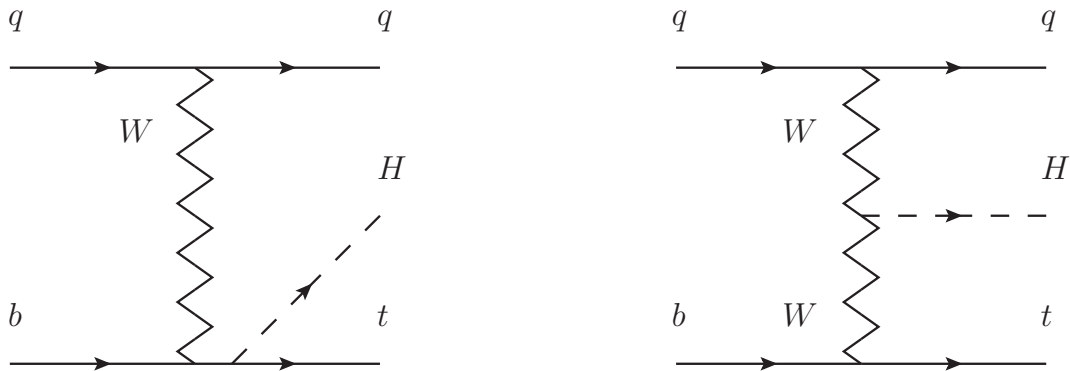


Figure 6.1: The two leading-order diagrams of tHq production.

1982 We selects events with three leptons and a b tagged jet in the final state. The tHq
 1983 signal contribution is then determined in a fit of the observed data to two multivariate
 1984 classifier outputs, each trained to discriminate against one of the two dominant back-
 1985 grounds of events with non-prompt leptons from $t\bar{t}$ and of associated production of $t\bar{t}$

1986 and vector bosons ($t\bar{t}W$, $t\bar{t}Z$). The fit result is then used to set an upper limit on the
 1987 combined $t\bar{t}H$, tHq and tHW production cross section, as a function of the relative
 1988 coupling strengths of Higgs and top quark and Higgs and W boson, respectively.

1989 6.2 Data and MC Samples

1990 The data considered in this analysis were collected by the CMS experiment dur-
 1991 ing 2016 and correspond to a total integrated luminosity of 35.9fb^{-1} . Only periods
 1992 when the CMS magnet was on were considered when selecting the data samples, that
 1993 corresponds to the 23 Sep 2016 (Run B to G) and PromptReco (Run H) versions
 1994 of the datasets. The MC samples used in this analysis correspond to the RunI-
 1995 ISummer16MiniAODv2 campaign produced with CMSSW 80X. The two signal sam-
 1996 ples (for tHq and tHW) were produced with MG5_aMC@NLO (version 5.222), in
 1997 leading-order mode, and are normalized to next-to-leading-order cross sections,
 1998 see Tab. 6.1. Each sample is generated with a set of event weights corresponding to
 1999 different values of κ_t and κ_V couplings as shown in Tab. 6.2.

2000 6.2.1 Full 2016 dataset and MC samples

Sample	σ [pb]	BF
/THQ_Hincl_13TeV-madgraph-pythia8_TuneCUETP8M1/	0.7927	0.324
/THW_Hincl_13TeV-madgraph-pythia8_TuneCUETP8M1/	0.1472	1.0

Table 6.1: Signal samples and their cross section and branching fraction used in this analysis. See Ref. [?] for more details.

2001 Different MC generators were used to generate the background processes. The
 2002 dominant sources ($t\bar{t}$, $t\bar{t}W$, $t\bar{t}Z$, $t\bar{t}H$) were produced using AMC@NLO interfaced
 2003 to PYTHIA8, and are scaled to NLO cross sections. Other processes are simulated

		<i>tHq</i>		<i>tHW</i>		
κ_V	κ_t	sum of weights	cross section [pb]	sum of weights	cross section [pb]	LHE weights
1.0	-3.0	35.700022	2.991	11.030445	0.6409	LHEweight_wgt[446]
1.0	-2.0	20.124298	1.706	5.967205	0.3458	LHEweight_wgt[447]
1.0	-1.5	14.043198	1.205	4.029093	0.2353	LHEweight_wgt[448]
1.0	-1.25	11.429338	0.9869	3.208415	0.1876	LHEweight_wgt[449]
1.0	-1.0		0.7927		0.1472	
1.0	-0.75	7.054998	0.6212	1.863811	0.1102	LHEweight_wgt[450]
1.0	-0.5	5.294518	0.4723	1.339886	0.07979	LHEweight_wgt[451]
1.0	-0.25	3.818499	0.3505	0.914880	0.05518	LHEweight_wgt[452]
1.0	0.0	2.627360	0.2482	0.588902	0.03881	LHEweight_wgt[453]
1.0	0.25	1.719841	0.1694	0.361621	0.02226	LHEweight_wgt[454]
1.0	0.5	1.097202	0.1133	0.233368	0.01444	LHEweight_wgt[455]
1.0	0.75	0.759024	0.08059	0.204034	0.01222	LHEweight_wgt[456]
1.0	1.0	0.705305	0.07096	0.273617	0.01561	LHEweight_wgt[457]
1.0	1.25	0.936047	0.0839	0.442119	0.02481	LHEweight_wgt[458]
1.0	1.5	1.451249	0.1199	0.709538	0.03935	LHEweight_wgt[459]
1.0	2.0	3.335034	0.2602	1.541132	0.08605	LHEweight_wgt[460]
1.0	3.0	10.516125	0.8210	4.391335	0.2465	LHEweight_wgt[461]
1.5	-3.0	45.281492	3.845	13.426212	0.7825	LHEweight_wgt[462]
1.5	-2.0	27.606715	2.371	7.809713	0.4574	LHEweight_wgt[463]
1.5	-1.5	20.476088	1.784	5.594971	0.3290	LHEweight_wgt[464]
1.5	-1.25	17.337465	1.518	4.635978	0.2749	LHEweight_wgt[465]
1.5	-1.0	14.483302	1.287	3.775902	0.2244	LHEweight_wgt[466]
1.5	-0.75	11.913599	1.067	3.014744	0.1799	LHEweight_wgt[467]
1.5	-0.5	9.628357	0.874	2.352505	0.1410	LHEweight_wgt[468]
1.5	-0.25	7.627574	0.702	1.789184	0.1081	LHEweight_wgt[469]
1.5	0.0	5.911882	0.5577	1.324946	0.08056	LHEweight_wgt[470]
1.5	0.25	4.479390	0.4365	0.959295	0.05893	LHEweight_wgt[471]
1.5	0.5	3.331988	0.3343	0.692727	0.04277	LHEweight_wgt[472]
1.5	0.75	2.469046	0.2558	0.525078	0.03263	LHEweight_wgt[473]
1.5	1.0	1.890565	0.2003	0.456347	0.02768	LHEweight_wgt[474]
1.5	1.25	1.596544	0.1689	0.486534	0.02864	LHEweight_wgt[475]
1.5	1.5	1.586983	0.1594	0.615638	0.03509	LHEweight_wgt[476]
1.5	2.0	2.421241	0.2105	1.170602	0.06515	LHEweight_wgt[477]
1.5	3.0	7.503280	0.5889	3.467546	0.1930	LHEweight_wgt[478]
0.5	-3.0	27.432685	2.260	8.929074	0.5136	LHEweight_wgt[479]
0.5	-2.0	13.956013	1.160	4.419093	0.2547	LHEweight_wgt[480]
0.5	-1.5	8.924438	0.7478	2.757611	0.1591	LHEweight_wgt[481]
0.5	-1.25	6.835341	0.5726	2.075247	0.1204	LHEweight_wgt[482]
0.5	-1.0	5.030704	0.4273	1.491801	0.08696	LHEweight_wgt[483]
0.5	-0.75	3.510528	0.2999	1.007273	0.05885	LHEweight_wgt[484]
0.5	-0.5	2.274811	0.1982	0.621663	0.03658	LHEweight_wgt[485]
0.5	-0.25	1.323555	0.1189	0.334972	0.01996	LHEweight_wgt[486]
0.5	0.0	0.656969	0.06223	0.147253	0.008986	LHEweight_wgt[487]
0.5	0.25	0.274423	0.02830	0.058342	0.003608	LHEweight_wgt[488]
0.5	0.5	0.176548	0.01778	0.068404	0.003902	LHEweight_wgt[489]
0.5	0.75	0.363132	0.03008	0.177385	0.009854	LHEweight_wgt[490]
0.5	1.0	0.834177	0.06550	0.385283	0.02145	LHEweight_wgt[491]
0.5	1.25	1.589682	0.1241	0.692099	0.03848	LHEweight_wgt[492]
0.5	1.5	2.629647	0.2047	1.097834	0.06136	LHEweight_wgt[493]
0.5	2.0	5.562958	0.4358	2.206057	0.1246	LHEweight_wgt[494]
0.5	3.0	14.843102	1.177	5.609519	0.3172	LHEweight_wgt[495]

Table 6.2: κ_V and κ_t combinations generated for the two signal samples and their NLO cross sections. The *tHq* cross section is multiplied by the branching fraction of the enforced leptonic decay of the top quark (0.324). See also Ref. [?].

Sample	σ [pb]
TTWJetsToLNu_TuneCUETP8M1_13TeV-amcatnloFXFX-madspin-pythia8	0.2043
TTZToLLNuNu_M-10_TuneCUETP8M1_13TeV-amcatnlo-pythia8	0.2529
tthJetToNonbb_M125_13TeV_amcatnloFXFX_madspin_pythia8_mWCutfix /store/cmst3/group/susy/gpetrucc/13TeV/u/TTLL_m1to10_L0_NoMS_for76X/	0.2151 0.0283
WGToLNuG_TuneCUETP8M1_13TeV-madgraphMLM-pythia8	585.8
ZGTo2LG_TuneCUETP8M1_13TeV-amcatnloFXFX-pythia8	131.3
TGJets_TuneCUETP8M1_13TeV_amcatnlo_madspin_pythia8	2.967
TGJets_TuneCUETP8M1_13TeV_amcatnlo_madspin_pythia8	2.967
TTGJets_TuneCUETP8M1_13TeV-amcatnloFXFX-madspin-pythia8	3.697
WpWpJJ_EWK_QCD_TuneCUETP8M1_13TeV-madgraph-pythia8	0.03711
ZZZ_TuneCUETP8M1_13TeV-amcatnlo-pythia8	0.01398
WWZ_TuneCUETP8M1_13TeV-amcatnlo-pythia8	0.1651
WZZ_TuneCUETP8M1_13TeV-amcatnlo-pythia8	0.05565
WW_DoubleScattering_13TeV-pythia8	1.64
tZq_ll_4f_13TeV-amcatnlo-pythia8_TuneCUETP8M1	0.0758
ST_tWll_5f_LO_13TeV-MadGraph-pythia8	0.01123
TTTT_TuneCUETP8M1_13TeV-amcatnlo-pythia8	0.009103
WZTo3LNu_TuneCUETP8M1_13TeV-powheg-pythia8	4.4296
ZZTo4L_13TeV_powheg_pythia8	1.256
TTJets_SingleLeptFromTbar_TuneCUETP8M1_13TeV-madgraphMLM-pythia8	182.1754
TTJets_SingleLeptFromT_TuneCUETP8M1_13TeV-madgraphMLM-pythia8	182.1754
TTJets_DiLept_TuneCUETP8M1_13TeV-madgraphMLM-pythia8	87.3
DYJetsToLL_M-10to50_TuneCUETP8M1_13TeV-amcatnloFXFX-pythia8	18610
DYJetsToLL_M-50_TuneCUETP8M1_13TeV-madgraphMLM-pythia8	6024
WJetsToLNu_TuneCUETP8M1_13TeV-amcatnloFXFX-pythia8	61526.7
ST_tW_top_5f_inclusiveDecays_13TeV-powheg-pythia8_TuneCUETP8M1	35.6
ST_tW_antitop_5f_inclusiveDecays_13TeV-powheg-pythia8_TuneCUETP8M1	35.6
ST_t-channel_4f_leptonDecays_13TeV-amcatnlo-pythia8_TuneCUETP8M1	70.3144
ST_t-channel_antitop_4f_leptonDecays_13TeV-powheg-pythia8_TuneCUETP8M1	26.2278
ST_s-channel_4f_leptonDecays_13TeV-amcatnlo-pythia8_TuneCUETP8M1	3.68064
WWTo2L2Nu_13TeV-powheg	10.481

Table 6.3: List of background samples used in this analysis (CMSSW 80X). In the first section of the table are listed the samples of the processes for which we use the simulation to extract the final yields and shapes, in the second section the samples of the processes we will estimate from data. The MC simulation is used to design the data driven methods and derive the associated systematics.

Sample	σ [pb]
ttWJets_13TeV_madgraphMLM	0.6105
ttZJets_13TeV_madgraphMLM	0.5297/0.692

Table 6.4: Leading-order $t\bar{t}W$ and $t\bar{t}Z$ samples used in the signal BDT training.

2004 using POWHEG interfaced to PYTHIA, or bare PYTHIA (see table 6.3 and [?] for
2005 more details).

Three lepton and Four lepton
HLT_DiMu9_Ele9_CaloIdL_TrackIdL_v*
HLT_Mu8_DiEle12_CaloIdL_TrackIdL_v*
HLT_TripleMu_12_10_5_v*
HLT_Ele16_Ele12_Ele8_CaloIdL_TrackIdL_v*
HLT_Mu23_TrkIsoVVL_Ele8_CaloIdL_TrackIdL_IsoVL_v*
HLT_Mu23_TrkIsoVVL_Ele8_CaloIdL_TrackIdL_IsoVL_DZ_v*
HLT_Mu8_TrkIsoVVL_Ele23_CaloIdL_TrackIdL_IsoVL_v*
HLT_Mu8_TrkIsoVVL_Ele23_CaloIdL_TrackIdL_IsoVL_DZ_v*
HLT_Ele23_Ele12_CaloIdL_TrackIdL_IsoVL_DZ_v*
HLT_Mu17_TrkIsoVVL_Mu8_TrkIsoVVL_DZ_v*
HLT_Mu17_TrkIsoVVL_TkMu8_TrkIsoVVL_DZ_v*
HLT_IsoMu22_v*
HLT_IsoTkMu22_v*
HLT_IsoMu22_eta2p1_v*
HLT_IsoTkMu22_eta2p1_v*
HLT_IsoMu24_v*
HLT_IsoTkMu24_v*
HLT_Ele27_WPTight_Gsf_v*
HLT_Ele25_eta2p1_WPTight_Gsf_v*
HLT_Ele27_eta2p1_WPLoose_Gsf_v*

Table 6.5: Table of high-level triggers that we consider in the analysis.

2006 6.2.2 Triggers

2007 We consider online-reconstructed events triggered by one, two, or three leptons.
 2008 Single-lepton triggers are included to boost the acceptance of events where the p_T of
 2009 the sub-leading lepton falls below the threshold of the double-lepton triggers. Ad-
 2010 ditionally, by including double-lepton triggers in the ≥ 3 lepton category, as well
 2011 as single-lepton triggers in all categories, we increase the efficiency, considering the
 2012 logical “or” of the trigger decisions of all the individual triggers in a given category.
 2013 Tab. 6.5 shows the lowest-threshold non-prescaled triggers present in the High-Level
 2014 Trigger (HLT) menus for both Monte-Carlo and data in 2016.

2015 6.2.2.1 Trigger efficiency scale factors

2016 The efficiency of events to pass the trigger is measured in simulation (trivially using
 2017 generator information) and in the data (using event collected by an uncorrelated

Category	Scale Factor
ee	1.01 ± 0.02
e μ	1.01 ± 0.01
$\mu\mu$	1.00 ± 0.01
3l	1.00 ± 0.03

Table 6.6: Trigger efficiency scale factors and associated uncertainties, shown here rounded to the nearest percent.

2018 MET trigger). Small differences between the data and MC efficiencies are corrected
 2019 by applying scale factors as shown in Tab. 6.6. The exact procedure and control plots
 2020 are documented in [?] for the current analysis.

2021 **6.3 Object Identification and event selection**

2022 **6.3.1 Jets and b tagging**

2023 The analysis uses anti- k_t (0.4) particle-flow (PF) jets, corrected for charged hadrons
 2024 not coming from the primary vertex (charged hadron subtraction), and having jet
 2025 energy corrections (`Summer16_23Sep2016V3`) applied as a function of the jet E_T and
 2026 η . Jets are only considered if they have a transverse energy above 25GeV.

2027 In addition, they are required to be separated from any lepton candidates passing
 2028 the fakeable object selections (see Tables 6.7 and 6.8) by $\Delta R > 0.4$.

2029 The loose and medium working points of the CSV b-tagging algorithm are used to
 2030 identify b jets. Data/simulation differences in the b tagging performance are corrected
 2031 by applying per-jet weights to the simulation, dependent on the jet p_T , eta, b tagging
 2032 discriminator, and flavor (from simulation truth) [?]. The per-event weight is taken
 2033 as the product of the per-jet weights, including those of the jets associated to the
 2034 leptons. More details can be found in the corresponding $t\bar{t}H$ documentation [?, ?].

2035 **6.3.2 Lepton selection**

Cut	Loose	Fakeable object	Tight
$ \eta < 2.4$	✓	✓	✓
p_T	$> 5\text{GeV}$	$> 15\text{GeV}$	$> 15\text{GeV}$
$ d_{xy} < 0.05 \text{ (cm)}$	✓	✓	✓
$ d_z < 0.1 \text{ (cm)}$	✓	✓	✓
$\text{SIP}_{3D} < 8$	✓	✓	✓
$I_{\text{mini}} < 0.4$	✓	✓	✓
is Loose Muon	✓	✓	✓
jet CSV	—	< 0.8484	< 0.8484
is Medium Muon	—	—	✓
tight-charge	—	—	✓
lepMVA > 0.90	—	—	✓

Table 6.7: Requirements on each of the three muon selections. In the cases where the cut values change between the selections, those values are listed in the table. Otherwise, whether the cut is applied is indicated. For the two p_T^{ratio} and CSV rows, the cuts marked with a † are applied to leptons that fail the lepton MVA cut, while the loose cut value is applied to those that pass the lepton MVA cut.

2036 The lepton reconstruction and selection is identical to that used in the $t\bar{t}H$ mul-
 2037 tilepton analysis, as documented in Refs. [?, ?]. For details on the reconstruction
 2038 algorithms, isolation, pileup mitigation, and a description of the lepton MVA dis-
 2039 criminator and validation plots thereof, we refer to that document since they are out
 2040 of the scope of this thesis. Three different selections are defined both for the electron
 2041 and muon object identification: the *Loose*, *Fakeable Object*, and *Tight* selection. As
 2042 described in more detail later, these are used for event level vetoes, the fake rate
 2043 estimation application region, and the final signal selection, respectively. The p_T of
 2044 fakeable objects is defined as $0.85 \times p_T(\text{jet})$, where the jet is the one associated to the
 2045 lepton object. This mitigates the dependence of the fake rate on the momentum of
 2046 the fakeable object and thereby improves the precision of the method.

2047 Tables 6.7 and 6.8 list the full criteria for the different selections of muons and
 2048 electrons.

Cut	Loose	Fakeable Object	Tight
$ \eta < 2.5$	✓	✓	✓
p_T	$> 7\text{GeV}$	$> 15\text{GeV}$	$> 15\text{GeV}$
$ d_{xy} < 0.05 \text{ (cm)}$	✓	✓	✓
$ d_z < 0.1 \text{ (cm)}$	✓	✓	✓
$\text{SIP}_{3D} < 8$	✓	✓	✓
$I_{\text{mini}} < 0.4$	✓	✓	✓
MVA ID $> (0.0, 0.0, 0.7)$	✓	✓	✓
$\sigma_{in\eta} < (0.011, 0.011, 0.030)$	—	✓	✓
$\text{H/E} < (0.10, 0.10, 0.07)$	—	✓	✓
$\Delta\eta_{in} < (0.01, 0.01, 0.008)$	—	✓	✓
$\Delta\phi_{in} < (0.04, 0.04, 0.07)$	—	✓	✓
$-0.05 < 1/E - 1/p < (0.010, 0.010, 0.005)$	—	✓	✓
p_T^{ratio}	—	$> 0.5^\dagger / -$	—
jet CSV	—	$< 0.3^\dagger / < 0.8484$	< 0.8484
tight-charge	—	—	✓
conversion rejection	—	—	✓
Number of missing hits	< 2	$== 0$	$== 0$
lepMVA > 0.90	—	—	✓

Table 6.8: Criteria for each of the three electron selections. In cases where the cut values change between selections, those values are listed in the table. Otherwise, whether the cut is applied is indicated. In some cases, the cut values change for different η ranges. These ranges are $0 < |\eta| < 0.8$, $0.8 < |\eta| < 1.479$, and $1.479 < |\eta| < 2.5$ and the respective cut values are given in the form (value₁, value₂, value₃).

2049 6.3.3 Lepton selection efficiency

2050 Efficiencies of reconstruction and selecting loose leptons are measured both for muons
 2051 and electrons using a tag and probe method on both data and MC, using $Z \rightarrow \ell^+ \ell^-$.
 2052 Corresponding scale factors are derived from the ratio of efficiencies and applied to the
 2053 selected These. Events are produced for the leptonic SUSY analyses using equivalent
 2054 lepton selections and recycled for the $t\bar{t}H$ analysis as well as for this analysis. The
 2055 efficiencies of applying the tight selection as defined in Tables 6.7 and 6.8, on the
 2056 loose leptons are determined again by using a tag and probe method on a sample of
 2057 DY-enriched events. They are documented for the $t\bar{t}H$ analysis in Ref. [?] and are
 2058 exactly equivalent for this analysis.

2059 6.4 Background predictions

2060 The modeling of reducible and irreducible backgrounds in this analysis uses the exact
 2061 methods, analysis code, and ROOT trees used for the $t\bar{t}H$ multilepton analysis. We
 2062 give a brief description of the methods and refer to the documentation of that analysis
 2063 in Refs. [?, ?] for any details.

2064 The backgrounds in three-lepton final states can be split in two broad categories:
 2065 irreducible backgrounds with genuine prompt leptons (i.e. from on-shell W and Z
 2066 boson decays); and reducible backgrounds where at least one of the leptons is “non-
 2067 prompt”, i.e. produced within a hadronic jet, either a genuine lepton from heavy
 2068 flavor decays, or simply mis-reconstructed jets.

2069 Irreducible backgrounds can be reliably estimated directly from Monte-Carlo sim-
 2070 ulated events, using higher-order cross sections or data control regions for the overall
 2071 normalization. This is done in this analysis for all backgrounds involving prompt lep-
 2072 tons: $t\bar{t}W$, $t\bar{t}Z$, $t\bar{t}H$, WZ , ZZ , $W^\pm W^\pm qq$, $t\bar{t}t\bar{t}$, tZq , tZW , WWW , WWZ , WZZ ,
 2073 ZZZ .

2074 Reducible backgrounds, on the other hand, are not well predicted by simulation,
 2075 and are estimated using data-driven methods. In the case of non-prompt leptons, a
 2076 fake rate method is used, where the contribution to the final selection is estimated by
 2077 extrapolating from a sideband (or “application region”) with a looser lepton definition
 2078 (the fakeable object definitions in Tabs. 6.7 and 6.8) to the signal selection. The tight-
 2079 to-loose ratios (or “fake rates”) are measured in several background dominated data
 2080 events with dedicated triggers, subtracting the residual prompt lepton contribution
 2081 using MC. Non-prompt leptons in our signal regions are predominantly produced in $t\bar{t}$
 2082 events, with a much smaller contribution, from Drell–Yan production. The systematic
 2083 uncertainty on the normalization of the non-prompt background estimation is on the

order of 50%, and thereby one of the dominant limitations on the performance of multilepton analyses in general and this analysis in particular. It consists of several individual sources, such as the result of closure tests of the method using simulated events, limited statistics in the data control regions due to necessary prescaling of lepton triggers, and the uncertainty in the subtraction of residual prompt leptons from the control region.

The fake background where the leptons pass the looser selection are weighted according to how many of them fail the tight criteria. Events with a single failing lepton are weighted with the factor $f/(1-f)$ for the estimate to the tight selection region, where f is the fake rate. Events with two failing leptons are given the negative weight $-f_i f_j / (1-f_i)(1-f_j)$, and for three leptons the weight is positive and equal to the product of $f/(1-f)$ factor evaluated for each failing lepton.

Figures 6.2 show the distributions of some relevant kinematic variables, normalized to the cross section of the respective processes and to the integrated luminosity.

6.5 Signal discrimination

The tHq signal is separated from the main backgrounds using a boosted decision tree (BDT) classifier, trained on simulated signal and background events. A set of discriminating variables are given as input to the BDT which produces a output distribution maximizing the discrimination power. Table 6.9 lists the input variables used while Figures 6.3 show their distributions for the relevant signal and background samples, for the three lepton channel. Two BDT classifiers are trained for the two main backgrounds expected in the analysis: events with prompt leptons from $t\bar{t}W$ and $t\bar{t}Z$ (also referred to as $t\bar{t}V$), and events with non-prompt leptons from $t\bar{t}$. The datasets used in the training are the tHq signal (see Tab. 6.1), and LO MADGRAPH samples

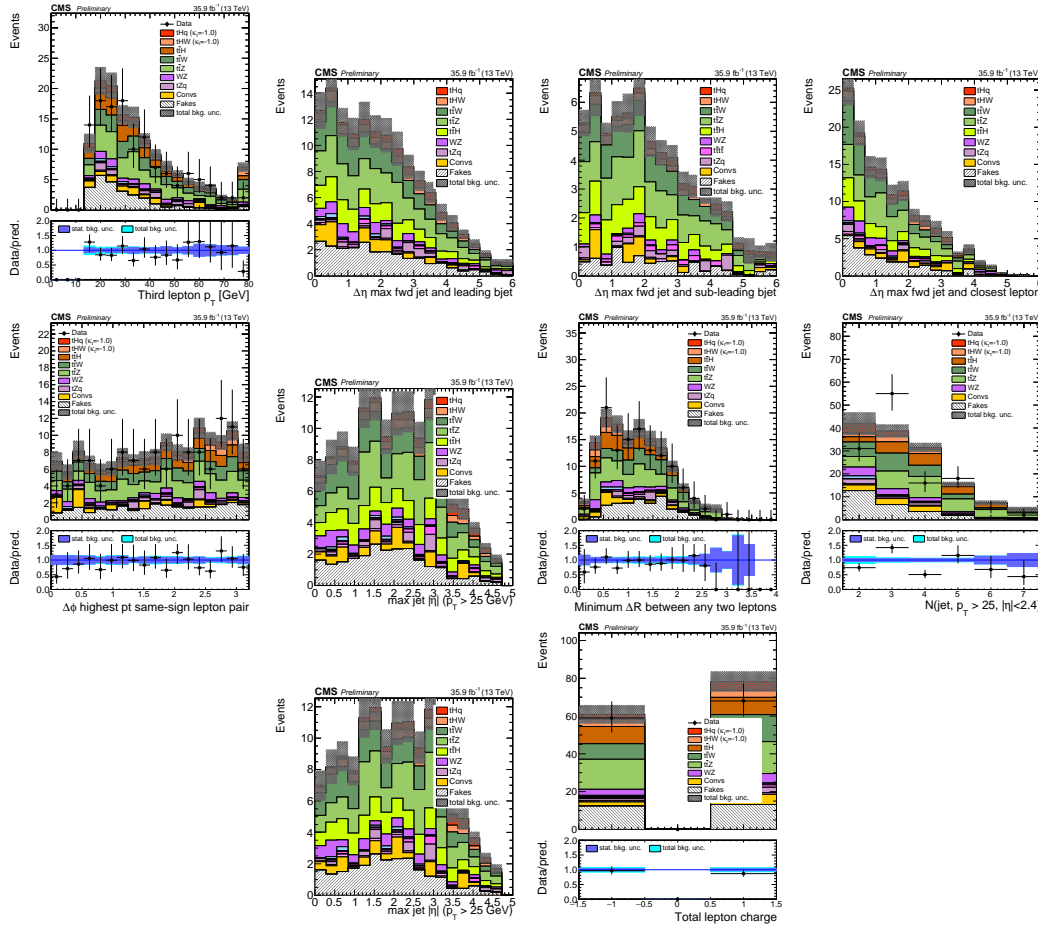


Figure 6.2: Distributions of input variables to the BDT for signal discrimination, three lepton channel, normalized to their cross section and to 35.9 fb^{-1} .

of $t\bar{t}W$ and $t\bar{t}Z$, in an admixture proportional to their respective cross sections (see Tab. 6.4).

The MVA analysis consist of two stages: first a “training” where the MVA method is trained to discriminate between simulated signal and background events, then a “test” stage where the trained algorithm is used to classify different events from the samples. The sample is obtained from a pre-selection (see Tab. ?? with pre-selection cuts). Figures 6.4 show the input variables distributions as seen by the MVA algorithm. Note that in contrast to the distributions in Fig. 6.3 only the main backgrounds ($t\bar{t}$ from simulation, $t\bar{t}V$) are included.

Variable name	Description
nJet25	Number of jets with $p_T > 25$ GeV, $ \eta < 2.4$
MaxEtaJet25	Maximum $ \eta $ of any (non-CSV-loose) jet with $p_T > 25$ GeV
totCharge	Sum of lepton charges
nJetEta1	Number of jets with $ \eta > 1.0$, non-CSV-loose
detaFwdJetBJet	$\Delta\eta$ between forward light jet and hardest CSV loose jet
detaFwdJet2BJet	$\Delta\eta$ between forward light jet and second hardest CSV loose jet (defaults to -1 in events with only one CSV loose jet)
detaFwdJetClosestLep	$\Delta\eta$ between forward light jet and closest lepton
dphiHighestPtSSPair	$\Delta\phi$ of highest p_T same-sign lepton pair
minDRll	minimum ΔR between any two leptons
Lep3Pt/Lep2Pt	p_T of the 3 rd lepton (2 nd for ss2l)

Table 6.9: MVA input discriminating variables

2117 Note that splitting the training in two groups reveals that some variables show
 2118 opposite behavior for the two background sources; potentially screening the discrimi-
 2119 nation power if they were to be used in a single discriminant. For some other variables
 2120 the distributions are similar in both background cases.

2121 From table 6.9, it is clear that the input variables are correlated to some extend.
 2122 These correlations play an important role for some MVA methods like the Fisher
 2123 discriminant method in which the first step consist of performing a linear transfor-
 2124 mation to an phase space where the correlations between variables are removed. In
 2125 case a boosted decision tree (BDT) method however, correlations do not affect the
 2126 performance. Figure 6.6 show the linear correlation coefficients for signal and back-
 2127 ground for the two training cases (the signal values are identical by construction). As
 2128 expected, strong correlations appears for variables related to the forward jet activity.
 2129 Same trend is seen in case of the same sign dilepton channel in Figure ??.

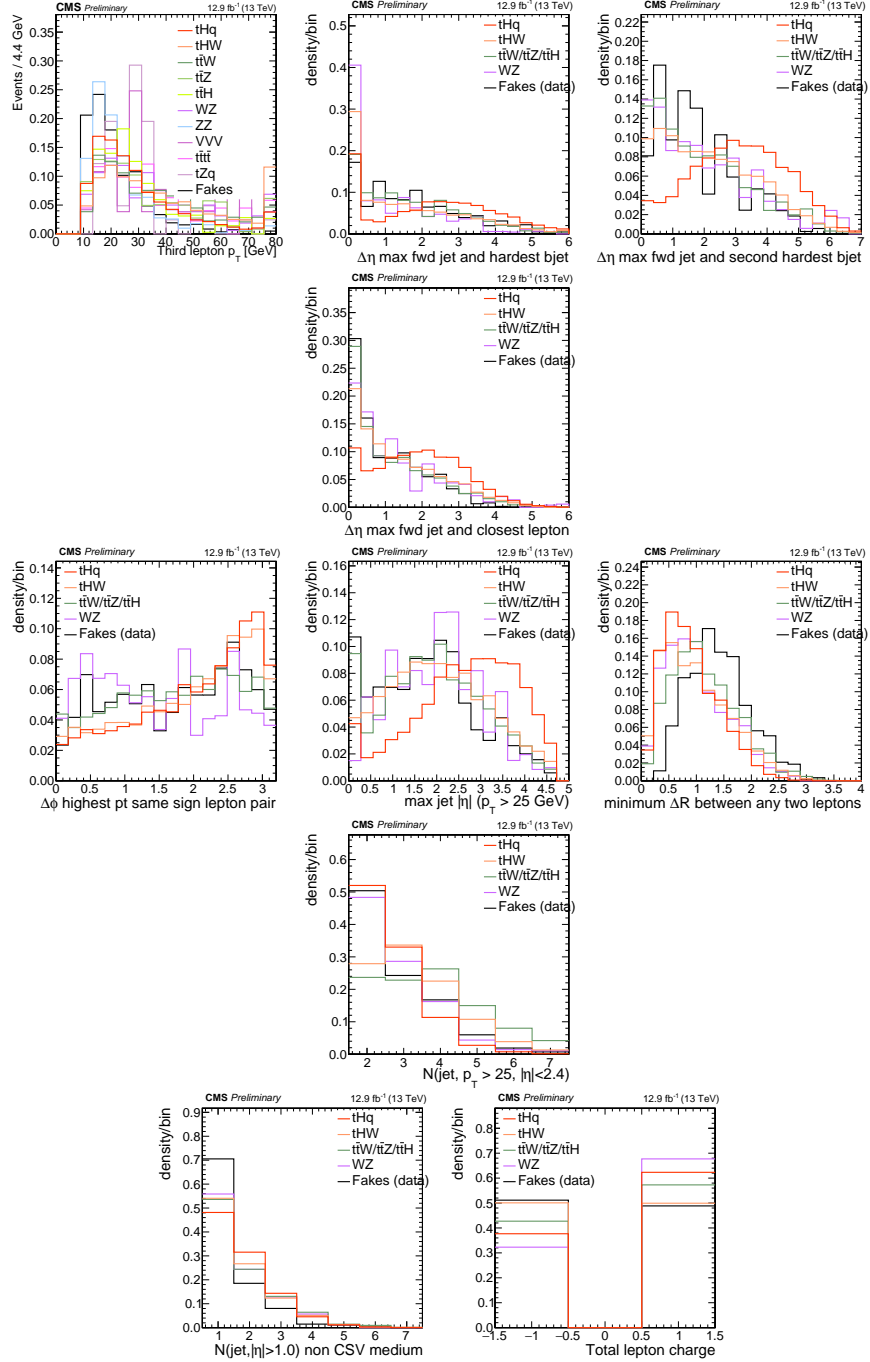


Figure 6.3: Distributions of input variables to the BDT for signal discrimination, three lepton channel.

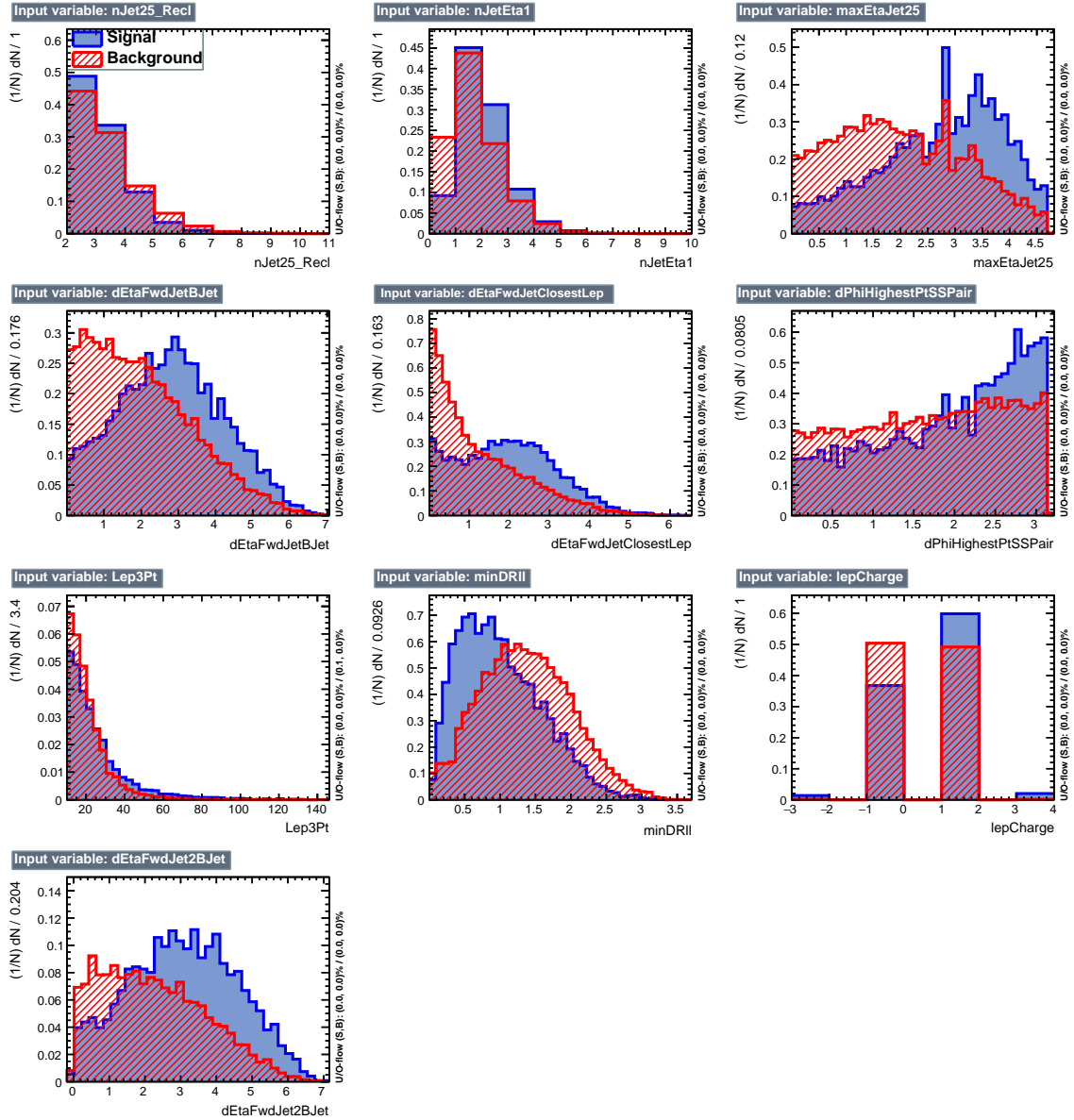


Figure 6.4: BDT inputs as seen by TMVA (signal, in blue, is tHq , background, in red, is $t\bar{t}$) for the three lepton channel, discriminated against $t\bar{t}$ (fakes) background.

2130 6.5.1 Classifiers response

2131 Several MVA algorithms were evaluated to determine the most appropriate method
 2132 for this analysis. The plots in Fig. 6.7 (top) show the background rejection as a
 2133 function of the signal efficiency for $t\bar{t}$ and $t\bar{t}V$ trainings (ROC curves) for the different

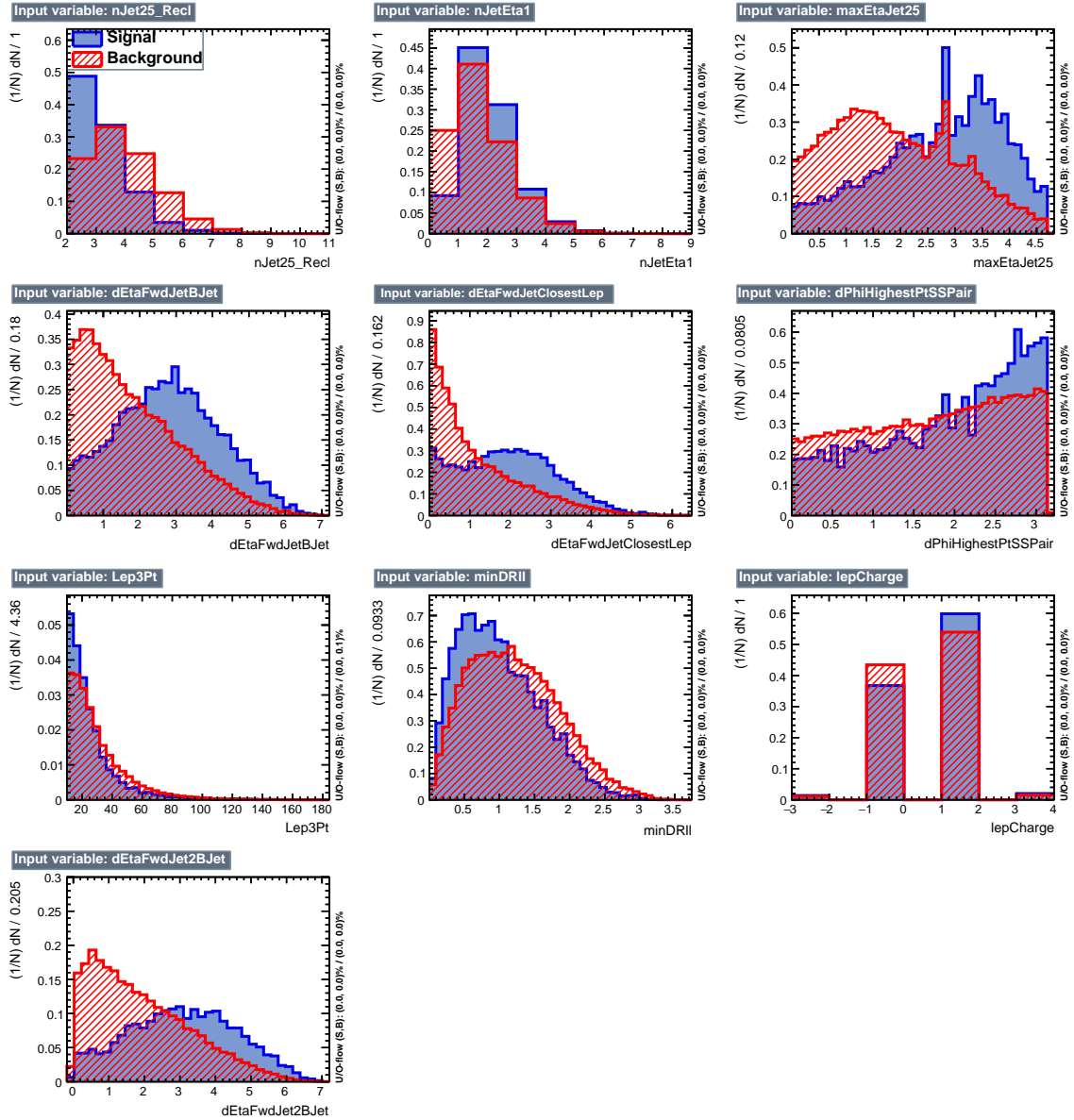


Figure 6.5: BDT inputs as seen by TMVA (signal, in blue, is tHq , background, in red, is $t\bar{t}W+t\bar{t}Z$) for the three lepton channel, discriminated against $t\bar{t}V$ background.

algorithms that were evaluated.

In both cases the gradient boosted decision tree (“BDTA_GRAD”) classifier offers the best results, followed by an adaptive BDT classifier (“BDTA”). The BDTA_GRAD classifier output distributions for signal and backgrounds are shown on the bottom of Fig. 6.7. As expected, a good discrimination power is obtained using default discrim-

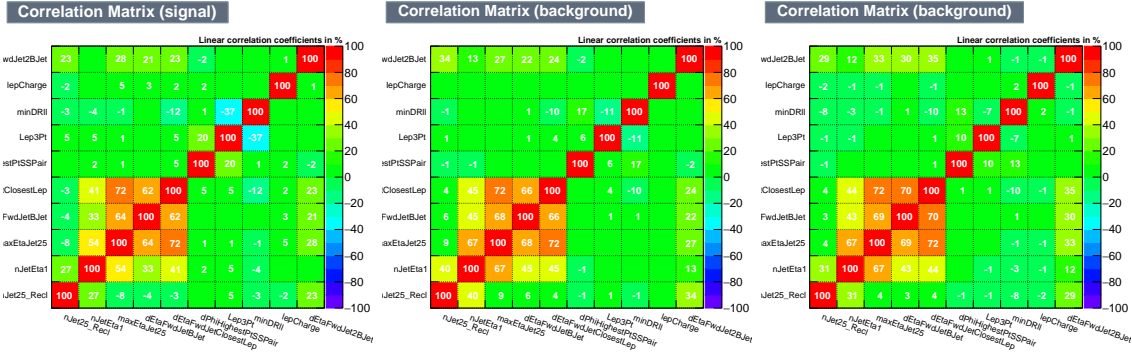


Figure 6.6: Signal (left), $t\bar{t}$ background (middle), and $t\bar{t}V$ background (right.) correlation matrices for the input variables in the TMVA analysis for the three lepton channel.

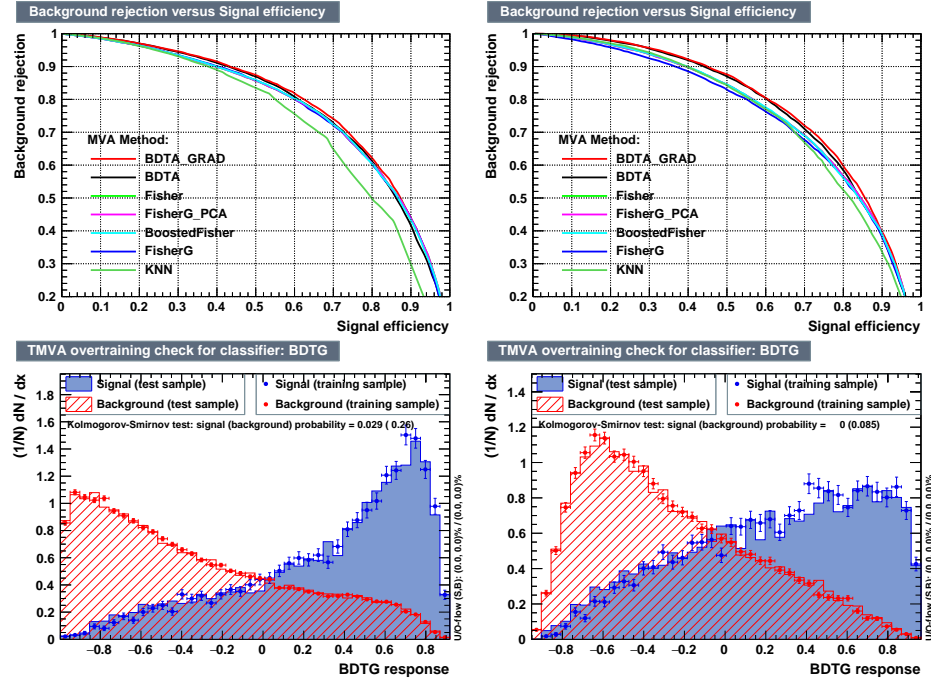


Figure 6.7: Top: background rejection vs signal efficiency (ROC curves) for various MVA classifiers (top) in the three lepton channel against $t\bar{t}V$ (left) and $t\bar{t}$ (right). Bottom: classifier output distributions for the gradient boosted decision trees, for training against $t\bar{t}V$ (left) and against $t\bar{t}$ (right).

2139 inator parameter values, with minimal overtraining. TMVA provides a ranking of the
 2140 input variables by their importance in the classification process, shown in Tab. 6.10.
 2141 The TMVA settings used in the BDT training are shown in Tab. 6.11.

ttbar training			ttV training		
Rank	Variable	Importance	Variable	Importance	
1	minDRll	1.329e-01	dEtaFwdJetBJet	1.264e-01	
2	dEtaFwdJetClosestLep	1.294e-01	Lep3Pt	1.224e-01	
3	dEtaFwdJetBJet	1.209e-01	maxEtaJet25	1.221e-01	
4	dPhiHighestPtSSPair	1.192e-01	dEtaFwdJet2BJet	1.204e-01	
5	Lep3Pt	1.158e-01	dEtaFwdJetClosestLep	1.177e-01	
6	maxEtaJet25	1.121e-01	minDRll	1.143e-01	
7	dEtaFwdJet2BJet	9.363e-02	dPhiHighestPtSSPair	9.777e-02	
8	nJetEta1	6.730e-02	nJet25_Recl	9.034e-02	
9	nJet25_Recl	6.178e-02	nJetEta1	4.749e-02	
10	lepCharge	4.701e-02	lepCharge	4.116e-02	

Table 6.10: TMVA input variables ranking for BDTA_GRAD method for the trainings in the three lepton channel. For both trainings the rankings show almost the same 5 variables in the first places.

```

TMVA.Types.kBDT
NTrees=800
BoostType=Grad
Shrinkage=0.10
!UseBaggedGrad
nCuts=50
MaxDepth=3
NegWeightTreatment=PairNegWeightsGlobal
CreateMVAPdfs

```

Table 6.11: TMVA configuration used in the BDT training.

2142 6.6 Additional discriminating variables

2143 Two additional discriminating variables were tested considering the fact that the
 2144 forward jet in the background could come from the pileup; since we have a real
 2145 forward jet in the signal, it could give some improvement in the discriminating power.
 2146 The additional variables describe the forward jet momentum (fwdJetPt25) and the
 2147 forward jet identification(fwdJetPUID). Distributions for these variables in the three
 2148 lepton channel are shown in the figure 6.8. The forward jet identification distribution
 2149 show that for both, signal and background, jets are mostly real jets.
 2150 The testing was made including in the MVA input one variable at a time, so we

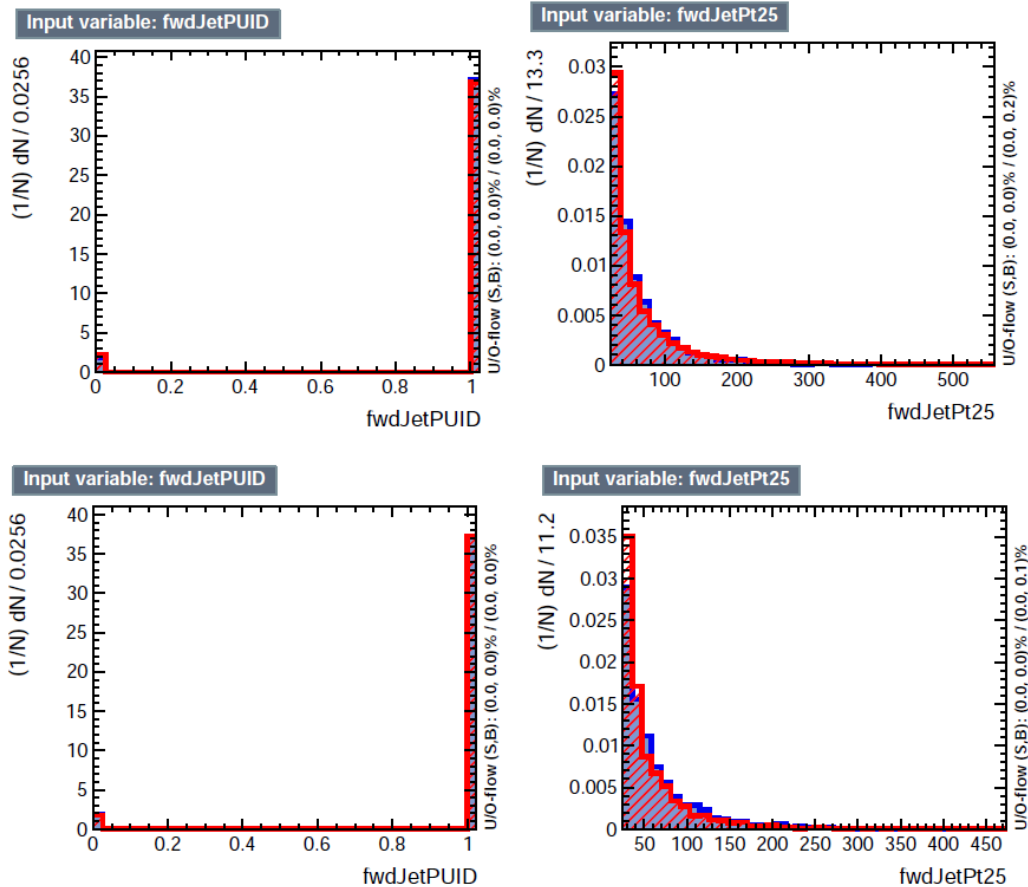


Figure 6.8: Additional discriminating variables distributions for ttV training (Top row) and tt training (bottom row) in the three lepton channel. The origin of the jets in the forward jet identification distribution is tagged as 0 for “pileup jets” while “real jets” are tagged as 1.

2151 can evaluate the discrimination power of each variable, and then both simultaneously.
 2152 fwdJetPUID was ranked in the last place in importance (11) in both training (ttV
 2153 and tt) while fwdJetPt25 was ranked 3 in the ttV training and 7 in the tt training.
 2154 When training using 12 variables, fwdJetPt25 was ranked 5 and 7 in the ttV and tt
 2155 trainings respectively, while fwdJetPUID was ranked 12 in both cases.

2156 The improvement in the discrimination performance provided by the additional
 2157 variables is about 1%, so it was decided not to include them in the procedure. Table
 2158 6.12 show the ROC-integral for all the testing cases we made.

ROC-integral	
base 10 var ttv	0.848
+ fwdJetPUID ttv	0.849
+ fwdJetPt25 ttv	0.856
12 var ttv	0.856
<hr/>	
base 10 var tt	0.777
+ fwdJetPUID tt	0.777
+ fwdJetPt25 tt	0.787
12 var	0.787

Table 6.12: ROC-integral for all the testing cases we made in the evaluation of the additional variables discriminating power. The improvement in the discrimination performance provided by the additional variables is about 1%

²¹⁵⁹ **References**

- 2160 [1] J. Schwinger. "Quantum Electrodynamics. I. A Covariant Formulation". Physical Review. 74 (10): 1439-61, (1948).
- 2161
- 2162 [2] R. P. Feynman. "Space-Time Approach to Quantum Electrodynamics". Physical Review. 76 (6): 769-89, (1949).
- 2163
- 2164 [3] S. Tomonaga. "On a Relativistically Invariant Formulation of the Quantum Theory of Wave Fields". Progress of Theoretical Physics. 1 (2): 27-42, (1946).
- 2165
- 2166 [4] D.J. Griffiths, "Introduction to electrodynamics". 4th ed. Pearson, (2013).
- 2167 [5] F. Mandl, G. Shaw. "Quantum field theory." Chichester: Wiley (2009).
- 2168 [6] F. Halzen, and A.D. Martin, "Quarks and leptons: An introductory course in modern particle physics". New York: Wiley, (1984) .
- 2169
- 2170 [7] File: Standard_Model_of_Elementary_Particle_dark.svg. (2017, June 12) Wikimedia Commons, the free media repository. Retrieved November 27, 2017 from <https://www.collegiate-advanced-electricity.com/single-post/2017/04/10/The-Standard-Model-of-Particle-Physics>.
- 2171
- 2172
- 2173
- 2174 [8] E. Noether, "Invariante Variationsprobleme", Nachrichten von der Gesellschaft der Wissenschaften zu Göttingen, mathematisch-physikalische Klasse, vol. 1918, pp. 235-257, (1918).
- 2175
- 2176

- 2177 [9] C. Patrignani et al. (Particle Data Group), Chin. Phys. C, 40, 100001 (2016)
2178 and 2017 update.
- 2179 [10] M. Goldhaber, L. Grodzins, A.W. Sunyar “Helicity of Neutrinos”, Phys. Rev.
2180 109, 1015 (1958).
- 2181 [11] Palanque-Delabrouille N et al. “Neutrino masses and cosmology with Lyman-
2182 alpha forest power spectrum”, JCAP 11 011 (2015).
- 2183 [12] M. Gell-Mann. “A Schematic Model of Baryons and Mesons”. Physics Letters.
2184 8 (3): 214-215 (1964).
- 2185 [13] G. Zweig. “An SU(3) Model for Strong Interaction Symmetry and its Breaking”
2186 (PDF). CERN Report No.8182/TH.401 (1964).
- 2187 [14] G. Zweig. “An SU(3) Model for Strong Interaction Symmetry and its Breaking:
2188 II” (PDF). CERN Report No.8419/TH.412(1964).
- 2189 [15] M. Gell-Mann. “The Interpretation of the New Particles as Displaced Charged
2190 Multiplets”. Il Nuovo Cimento 4: 848. (1956).
- 2191 [16] T. Nakano, K, Nishijima. “Charge Independence for V-particles”. Progress of
2192 Theoretical Physics 10 (5): 581-582. (1953).
- 2193 [17] N. Cabibbo, “Unitary symmetry and leptonic decays” Physical Review Letters,
2194 vol. 10, no. 12, p. 531, (1963).
- 2195 [18] M.Kobayashi, T.Maskawa, “CP-violation in the renormalizable theory of weak
2196 interaction,” Progress of Theoretical Physics, vol. 49, no. 2, pp. 652-657, (1973).
- 2197 [19] File: Weak Decay (flipped).svg. (2017, June 12). Wikimedia Com-
2198 mons, the free media repository. Retrieved November 27, 2017 from

- 2199 https://commons.wikimedia.org/w/index.php?title=File:Weak_Decay_(flipped)
2200 .svg&oldid=247498592.
- 2201 [20] Georgia Tech University. Coupling Constants for the Fundamental
2202 Forces(2005). Retrieved January 10, 2018, from http://hyperphysics.phy-
2203 astr.gsu.edu/hbase/Forces/couple.html#c2
- 2204 [21] M. Strassler. (May 31, 2013).The Strengths of the Known Forces. Retrieved Jan-
2205 uary 10, 2018, from https://profmattstrassler.com/articles-and-posts/particle-
2206 physics-basics/the-known-forces-of-nature/the-strength-of-the-known-forces/
- 2207 [22] S.L. Glashow. “Partial symmetries of weak interactions”, Nucl. Phys. 22 579-
2208 588, (1961).
- 2209 [23] A. Salam, J.C. Ward. “Electromagnetic and weak interactions”, Physics Letters
2210 13 168-171, (1964).
- 2211 [24] S. Weinberg, “A model of leptons”, Physical Review Letters, vol. 19, no. 21, p.
2212 1264, (1967).
- 2213 [25] M. Peskin, D. Schroeder, “An introduction to quantum field theory”. Perseus
2214 Books Publishing L.L.C., (1995).
- 2215 [26] A. Pich. “The Standard Model of Electroweak Interactions”
2216 https://arxiv.org/abs/1201.0537
- 2217 [27] F.Bellaiche. (2012, 2 September). “What’s this Higgs boson anyway?”. Retrieved
2218 from: https://www.quantum-bits.org/?p=233
- 2219 [28] M. Endres et al. Nature 487, 454-458 (2012) doi:10.1038/nature11255

- 2220 [29] F. Englert, R. Brout. “Broken Symmetry and the Mass of Gauge
2221 Vector Mesons”. Physical Review Letters. 13 (9): 321-23.(1964)
2222 doi:10.1103/PhysRevLett.13.321
- 2223 [30] P.Higgs. “Broken Symmetries and the Masses of Gauge Bosons”. Physical Re-
2224 view Letters. 13 (16): 508-509,(1964). doi:10.1103/PhysRevLett.13.508.
- 2225 [31] G.Guralnik, C.R. Hagen and T.W.B. Kibble. “Global Conservation Laws
2226 and Massless Particles”. Physical Review Letters. 13 (20): 585-587, (1964).
2227 doi:10.1103/PhysRevLett.13.585.
- 2228 [32] CMS collaboration. “Observation of a new boson at a mass of 125 GeV with
2229 the CMS experiment at the LHC”. Physics Letters B. 716 (1): 30-61 (2012).
2230 arXiv:1207.7235. doi:10.1016/j.physletb.2012.08.021
- 2231 [33] ATLAS collaboration. “Observation of a New Particle in the Search for the Stan-
2232 dard Model Higgs Boson with the ATLAS Detector at the LHC”. Physics Letters
2233 B. 716 (1): 1-29 (2012). arXiv:1207.7214. doi:10.1016/j.physletb.2012.08.020.
- 2234 [34] ATLAS collaboration; CMS collaboration (26 March 2015). “Combined Mea-
2235 surement of the Higgs Boson Mass in pp Collisions at $\sqrt{s}=7$ and 8 TeV with
2236 the ATLAS and CMS Experiments”. Physical Review Letters. 114 (19): 191803.
2237 arXiv:1503.07589. doi:10.1103/PhysRevLett.114.191803.
- 2238 [35] LHC InternationalMasterclasses“When protons collide”. Retrieved from http://atlas.physicsmasterclasses.org/en/zpath_protoncollisions.htm
- 2240 [36] CMS Collaboration, “SM Higgs Branching Ratios and Total Decay Widths (up-
2241 date in CERN Report4 2016)”. <https://twiki.cern.ch/twiki/bin/view/LHCPhysics/CERNYellowReportPageBR> , last accessed on 17.12.2017.

- 2243 [37] R.Grant V. “Determination of Higgs branching ratios in $H \rightarrow W^+W^- \rightarrow l\nu jj$
 2244 and $H \rightarrow ZZ \rightarrow l^+l^-jj$ channels”. Physics Department, University of Tennessee
 2245 (Dated: October 31, 2012). Retrieved from <http://aesop.phys.utk.edu/ph611/2012/projects/Riley.pdf>
- 2246
- 2247 [38] LHC Higgs Cross Section Working Group, Denner, A., Heinemeyer, S. et al.
 2248 “Standard model Higgs-boson branching ratios with uncertainties”. Eur. Phys.
 2249 J. C (2011) 71: 1753. <https://doi.org/10.1140/epjc/s10052-011-1753-8>
- 2250 [39] F. Maltoni, K. Paul, T. Stelzer, and S. Willenbrock, “Associated production
 2251 of Higgs and single top at hadron colliders”, Phys.Rev. D64 (2001) 094023,
 2252 [hep-ph/0106293].
- 2253 [40] S. Biswas, E. Gabrielli, F. Margaroli, and B. Mele, “Direct constraints on the
 2254 top-Higgs coupling from the 8 TeV LHC data,” Journal of High Energy Physics,
 2255 vol. 07, p. 073, (2013).
- 2256 [41] M. Farina, C. Grojean, F. Maltoni, E. Salvioni, and A. Thamm, “Lifting de-
 2257 generacies in Higgs couplings using single top production in association with a
 2258 Higgs boson,” Journal of High Energy Physics, vol. 05, p. 022, (2013).
- 2259 [42] T.M. Tait and C.-P. Yuan, “Single top quark production as a window to physics
 2260 beyond the standard model”, Phys. Rev. D 63 (2000) 014018 [hep-ph/0007298].
- 2261 [43] F. Demartin, F. Maltoni, K. Mawatari, and M. Zaro, “Higgs production in
 2262 association with a single top quark at the LHC,” European Physical Journal C,
 2263 vol. 75, p. 267, (2015).

- 2264 [44] CMS Collaboration, “Modelling of the single top-quark production in associa-
 2265 tion with the Higgs boson at 13 TeV.” <https://twiki.cern.ch/twiki/bin/viewauth/CMS/SingleTopHiggsGeneration13TeV>, last accessed on 16.01.2018.
- 2267 [45] CMS Collaboration, “SM Higgs production cross sections at $\sqrt{s} =$
 2268 13 TeV.” <https://twiki.cern.ch/twiki/bin/view/LHCPhysics/CERNYellowReportPageAt13TeV>, last accessed on 16.01.2018.
- 2270 [46] S. Dawson, The effective W approximation, Nucl. Phys. B 249 (1985) 42.
- 2271 [47] S. Biswas, E. Gabrielli and B. Mele, JHEP 1301 (2013) 088 [arXiv:1211.0499
 2272 [hep-ph]].
- 2273 [48] F. Demartin, B. Maier, F. Maltoni, K. Mawatari, and M. Zaro, “tWH associated
 2274 production at the LHC”, European Physical Journal C, vol. 77, p. 34, (2017).
 2275 arXiv:1607.05862
- 2276 [49] LHC Higgs Cross Section Working Group, “Handbook of LHC Higgs Cross
 2277 Sections: 4.Deciphering the Nature of the Higgs Sector”, arXiv:1610.07922.
- 2278 [50] J. Ellis, D. S. Hwang, K. Sakurai, and M. Takeuchi.“Disentangling Higgs-Top
 2279 Couplings in Associated Production”, JHEP 1404 (2014) 004, [arXiv:1312.5736].
- 2280 [51] CMS Collaboration, V. Khachatryan et al., “Precise determination of the mass
 2281 of the Higgs boson and tests of compatibility of its couplings with the standard
 2282 model predictions using proton collisions at 7 and 8 TeV,” arXiv:1412.8662.
- 2283 [52] ATLAS Collaboration, G. Aad et al., “Updated coupling measurements of the
 2284 Higgs boson with the ATLAS detector using up to 25 fb^{-1} of proton-proton
 2285 collision data”, ATLAS-CONF-2014-009.

- 2286 [53] ATLAS and CMS Collaborations, “Measurements of the Higgs boson produc-
2287 tion and decay rates and constraints on its couplings from a combined ATLAS
2288 and CMS analysis of the LHC pp collision data at $\sqrt{s} = 7$ and 8 TeV,” (2016).
2289 CERN-EP-2016-100, ATLAS-HIGG-2015-07, CMS-HIG-15-002.
- 2290 [54] File:Cern-accelerator-complex.svg. Wikimedia Commons,
2291 the free media repository. Retrieved January, 2018 from
2292 <https://commons.wikimedia.org/wiki/File:Cern-accelerator-complex.svg>
- 2293 [55] J.L. Caron , “Layout of the LEP tunnel including future LHC infrastructures.”,
2294 (Nov, 1993). A C Collection. Legacy of AC. Pictures from 1992 to 2002. Re-
2295 trieval from <https://cds.cern.ch/record/841542>
- 2296 [56] M. Vretenar, “The radio-frequency quadrupole”. CERN Yellow Report CERN-
2297 2013-001, pp.207-223 DOI:10.5170/CERN-2013-001.207. arXiv:1303.6762
- 2298 [57] L.Evans. P. Bryant (editors). “LHC Machine”. JINST 3 S08001 (2008).
- 2299 [58] CERN Photographic Service.“Radio-frequency quadrupole, RFQ-1”, March
2300 1983, CERN-AC-8303511. Retrieved from <https://cds.cern.ch/record/615852>.
- 2301 [59] CERN Photographic Service “Animation of CERN’s accelerator net-
2302 work”, 14 October 2013. DOI: 10.17181/cds.1610170 Retrieved from
2303 <https://videos.cern.ch/record/1610170>
- 2304 [60] C.Sutton. “Particle accelerator”.Encyclopedia Britannica. July 17, 2013. Re-
2305 trieval from <https://www.britannica.com/technology/particle-accelerator>.
- 2306 [61] L.Guiraud. “Installation of LHC cavity in vacuum tank.”. July 27 2000. CERN-
2307 AC-0007016. Retrieved from <https://cds.cern.ch/record/41567>.

- 2308 [62] J.L. Caron, “Magnetic field induced by the LHC dipole’s superconducting coils”.
2309 March 1998. AC Collection. Legacy of AC. Pictures from 1992 to 2002. LHC-
2310 PHO-1998-325. Retrieved from <https://cds.cern.ch/record/841511>
- 2311 [63] AC Team. “Diagram of an LHC dipole magnet”. June 1999. CERN-DI-9906025
2312 retrieved from <https://cds.cern.ch/record/40524>.
- 2313 [64] CMS Collaboration “Public CMS Luminosity Information”.
2314 <https://twiki.cern.ch/twiki/bin/view/CMSPublic/LumiPublicResults#2016>
2315 _proton_proton_13_TeV_collis, last accessed 24.01.2018
- 2316 [65] J.L. Caron. “LHC Layout” AC Collection. Legacy of AC. Pictures
2317 from 1992 to 2002. September 1997, LHC-PHO-1997-060. Retrieved from
2318 <https://cds.cern.ch/record/841573>.
- 2319 [66] J.A. Coarasa. “The CMS Online Cluster: Setup, Operation and Maintenance
2320 of an Evolving Cluster”. ISGC 2012, 26 February - 2 March 2012, Academia
2321 Sinica, Taipei, Taiwan.
- 2322 [67] CMS Collaboration. “The CMS experiment at the CERN LHC” JINST 3 S08004
2323 (2008).
- 2324 [68] CMS Collaboration. “CMS detector drawings 2012” CMS-PHO-GEN-2012-002.
2325 Retrieved from <http://cds.cern.ch/record/1433717>.
- 2326 [69] R. Breedon. “View through the CMS detector during the cooldown of the
2327 solenoid on February 2006. CMS Collection”, February 2006, CMS-PHO-
2328 OREACH-2005-004, Retrieved from <https://cds.cern.ch/record/930094>.
- 2329 [70] A. Dominguez et. al. “CMS Technical Design Report for the Pixel Detector
2330 Upgrade”, CERN-LHCC-2012-016. CMS-TDR-11.

- 2331 [71] CMS Collaboration. “Description and performance of track and primary-vertex
2332 reconstruction with the CMS tracker,” Journal of Instrumentation, vol. 9, no.
2333 10, p. P10009,(2014).
- 2334 [72] CMS Collaboration and M. Brice. “Images of the CMS Tracker Inner
2335 Barrel”, November 2008, CMS-PHO-TRACKER-2008-002. Retrieved from
2336 <https://cds.cern.ch/record/1431467>.
- 2337 [73] M. Weber. “The CMS tracker”. 6th international conference on hyperons, charm
2338 and beauty hadrons Chicago, June 28-July 3 2004.
- 2339 [74] CMS Collaboration. “Projected Performance of an Upgraded CMS Detector at
2340 the LHC and HL-LHC: Contribution to the Snowmass Process”. Jul 26, 2013.
2341 arXiv:1307.7135
- 2342 [75] L. Veillet. “End assembly of HB with EB rails and rotation in-
2343 side SX ”,January 2002. CMS-PHO-HCAL-2002-002. Retrieved from
2344 <https://cds.cern.ch/record/42594>.
- 2345 [76] J. Puerta-Pelayo.“First DT+RPC chambers installation round in the
2346 UX5 cavern.”. January 2007, CMS-PHO-OREACH-2007-001. Retrieved from
2347 <https://cds.cern.ch/record/1019185>
- 2348 [77] X. Cid Vidal and R. Cid Manzano. “CMS Global Muon Trigger” web
2349 site: Taking a closer look at LHC. Retrieved from https://www.lhc-closer.es/taking_a_closer_look_at_lhc/0.lhc_trigger
- 2351 [78] WLCG Project Office, “Documents & Reference - Tiers - Structure,” (2014).
2352 <http://wlcg.web.cern.ch/documents-reference> , last accessed on 30.01.2018.

- 2353 [79] CMS Collaboration. “CMSSW Application Framework”,
 2354 <https://twiki.cern.ch/twiki/bin/view/CMSPublic/WorkBookCMSSWFramework>,
 2355 last accesses 06.02.2018
- 2356 [80] A. Buckleya, J. Butterworthb, S. Giesekec, et. al. “General-purpose event gen-
 2357 erators for LHC physics”. arXiv:1101.2599v1 [hep-ph] 13 Jan 2011
- 2358 [81] A. Quadt. “Top Quark Physics at Hadron Colliders”. Advances in the Physics
 2359 of Particles and Nuclei. Springer-Verlag Berlin Heidelberg. DOI: 10.1007/978-
 2360 3-540-71060-8 (2007)
- 2361 [82] DurhamHep Data Project, “The Durham HepData Project - PDF Plotter.”
 2362 <http://hepdata.cedar.ac.uk/pdf/pdf3.html> , last accessed on 02.02.2018.
- 2363 [83] F. Maltoni, G. Ridolfi, and M. Ubiali, “b-initiated processes at the LHC: a
 2364 reappraisal,” Journal of High Energy Physics, vol. 07, p. 022, (2012).
- 2365 [84] B. Andersson, G. Gustafson, G.Ingelman and T. Sjostrand, “Parton fragmen-
 2366 tation and string dynamics”, Physics Reports, Vol. 97, No. 2-3, pp. 31-145,
 2367 1983.
- 2368 [85] CMS Collaboration, “Event generator tunes obtained from underlying event
 2369 and multiparton scattering measurements;” European Physical Journal C, vol.
 2370 76, no. 3, p. 155, (2016).
- 2371 [86] J. Alwall et. al., “The automated computation of tree-level and next-to-leading
 2372 order differential cross sections, and their matching to parton shower simula-
 2373 tions,” Journal of High Energy Physics, vol. 07, p. 079, (2014).

- 2374 [87] S. Frixione, P. Nason, and C. Oleari, “Matching NLO QCD computations with
 2375 Parton Shower simulations: the POWHEG method,” Journal of High Energy
 2376 Physics, vol. 11, p. 070, (2007).
- 2377 [88] S. Agostinelli et al., “GEANT4: A Simulation toolkit,” Nuclear Instruments
 2378 and Methods in Physics, vol. A506, pp. 250–303, (2003).
- 2379 [89] J.Allison et.al.,“Recent developments in Geant4”, Nuclear Instruments and
 2380 Methods in Physics Research A 835 (2016) 186-225.
- 2381 [90] CMS Collaboration “Full Simulation Offline Guide”, <https://twiki.cern.ch/twiki/bin/view/CMSPublic/SWGuideSimulation>, last accessed 04.02.2018
- 2383 [91] A. Giammanco. “The Fast Simulation of the CMS Experiment” J. Phys.: Conf.
 2384 Ser. 513 022012 (2014)
- 2385 [92] A.M. Sirunyan et. al. “Particle-flow reconstruction and global event description
 2386 with the CMS detector”, JINST 12 P10003 (2017) <https://doi.org/10.1088/1748-0221/12/10/P10003>.
- 2388 [93] The CMS Collaboration. “ Description and performance of track and pri-
 2389 mary vertex reconstruction with the CMS tracker”. JINST 9 P10009 (2014).
 2390 doi:10.1088/1748-0221/9/10/P10009
- 2391 [94] J. Incandela. “Status of the CMS SM Higgs Search” July 4, 2012. Pdf slides.
 2392 Retrieved from https://indico.cern.ch/event/197461/contributions/1478917/attachments/290954/406673/CMS_4July2012_Final.pdf
- 2394 [95] P. Billoir and S. Qian, “Simultaneous pattern recognition and track fitting by
 2395 the Kalman filtering method”, Nucl. Instrum. Meth. A 294 219. (1990).

- 2396 [96] W. Adam, R. Fruhwirth, A. Strandlie and T. Todorov, “Reconstruction of
 2397 electrons with the Gaussian sum filter in the CMS tracker at LHC”, eConf
 2398 C 0303241 (2003) TULT009 [physics/0306087].
- 2399 [97] K. Rose, “Deterministic Annealing for Clustering, Compression, Classification,
 2400 Regression and related Optimisation Problems”, Proc. IEEE 86 (1998) 2210.
- 2401 [98] R. Fruhwirth, W. Waltenberger and P. Vanlaer, “ Adaptive Vertex Fitting”,
 2402 CMS Note 2007-008 (2007).
- 2403 [99] CMS collaboration, “Performance of CMS muon reconstruction in pp collision
 2404 events at $\sqrt{s} = 7$ TeV ”, JINST 7 P10002 2012, [arXiv:1206.4071].
- 2405 [100] M. Cacciari, G. P. Salam, and G. Soyez, “The anti- k_t jet clustering algorithm,”
 2406 Journal of High Energy Physics, vol. 04, p. 063, (2008).
- 2407 [101] B. Dorney. “Anatomy of a Jet in CMS”. Quantum Diaries. June
 2408 1st, 2011. Retrieved from <https://www.quantumdiaries.org/2011/06/01/anatomy-of-a-jet-in-cms/>
- 2410 [102] The CMS Collaboration.“Event Displays from the high-energy collisions at 7
 2411 TeV”, May 2010, CMS-PHO-EVENTS-2010-007, Retrieved from <https://cds.cern.ch/record/1429614>.
- 2413 [103] The CMS collaboration. “Determination of jet energy calibration and transverse
 2414 momentum resolution in CMS”. JINST 6 P11002 (2011). <http://dx.doi.org/10.1088/1748-0221/6/11/P11002>
- 2416 [104] The CMS Collaboration, “Introduction to Jet Energy Corrections at
 2417 CMS.”. <https://twiki.cern.ch/twiki/bin/view/CMS/IntroToJEC>, last ac-
 2418 cessed 10.02.2018.

- 2419 [105] CMS Collaboration Collaboration. “Identification of b quark jets at the CMS
2420 Experiment in the LHC Run 2”. Tech. rep. CMS-PAS-BTV-15-001. Geneva:
2421 CERN, (2016). <https://cds.cern.ch/record/2138504>.
- 2422 [106] CMS Collaboration Collaboration. “Performance of missing energy reconstruc-
2423 tion in 13 TeV pp collision data using the CMS detector”. Tech. rep. CMS-PAS-
2424 JME16-004. Geneva: CERN, 2016. <https://cds.cern.ch/record/2205284>.
- 2425 [107] K. Skovpen. “Event displays highlighting the main properties of heavy flavour
2426 jets in the CMS Experiment”, Aug 2017, CMS-PHO-EVENTS-2017-006. Re-
2427 trieved from <https://cds.cern.ch/record/2280025>.
- 2428 [108] G. Cowan. “Topics in statistical data analysis for high-energy physics”.
2429 arXiv:1012.3589v1
- 2430 [109] L. Lista. “Statistical Methods for Data Analysis in Particle Physics”, 2nd
2431 ed. Springer International Publishing. (2017) <https://dx.doi.org/10.1007/978-3-319-62840-0>
- 2433 [110] Y. Coadou. “Boosted decision trees”, ESIPAP, Archamps, 9 February 2016.
2434 Lecture.
- 2435 [111] J. Neyman and E. S. Pearson, “On the problem of the most efficient tests
2436 of statistical hypotheses”. Philosophical Transactions of the Royal Society of
2437 London. Series A, Containing Papers of a Mathematical or Physical Character.
2438 Vol. 231 (1933), pp. 289-337